Development and Characterization of Ultrasensitive Carbon Nanotube Paper-Based Capacitive Sensors for Human-Machine Interfaces and Machine Learning-Enhanced Eye Tracking

Tianyi Li

A dissertation

submitted in partial fulfillment of the

requirements for the degree of

Doctor of Philosophy

University of Washington

2024

Reading Committee:

Jae-Hyun Chung, Chair

Robijanto Soetedjo

Lucas R. Meza

Program Authorized to Offer Degree:

Mechanical Engineering

University of Washington

Abstract

Development and Characterization of Ultrasensitive Carbon Nanotube Paper-Based Capacitive Sensors for Human-Machine Interfaces and Machine Learning-Enhanced Eye Tracking

Tianyi Li

Chair of the Supervisory Committee:

Jae-Hyun Chung

Department of Mechanical Engineering

Capacitive sensors are playing an important role in human-machine interfaces (HMI) for their simplicity, speed, and robustness. However, in wearable applications, traditional metal capacitive sensors' proximity sensitivity is limited by their small size. In this dissertation, I present my research on studying the proximity sensitivity of a capacitive sensor made of carbon-nanotube-paper-composite (CPC) and its application in HMI and wearable eye-trackers.

CPC capacitive sensors had conductive cellulose fibers whose high aspect ratio structures increased the electric field strength and total surface area, leading to a higher capacitive sensitivity. The effect of cellulose fiber geometries on sensor sensitivity was studied with finite element

analysis. The proximity and pressure sensitivity of CPC capacitive sensors were characterized and benchmarked against identically sized silver sensors. The CPC sensor provides a highly-sensitive, multi-modal sensing solution for wearable devices and other HMI applications.

A non-human primate capacitive eye-tracker used four CPC capacitive sensors that sensed the displacement changes at the scleral-corneal junction during eye movements. The capacitive eye-tracker was benchmarked against the gold standard scleral search coil on two rhesus monkeys, showing a high signal correlation. Various data processing methods and machine learning techniques were studied to optimize signal quality, achieving gaze detection accuracy comparable to top-end commercial solutions while having superior portability. This lightweight, non-invasive capacitive eye tracker offered potential as an alternative to the traditional coil and camera-based systems in oculomotor research and vision science.

CPC capacitive sensors were further developed into a cylindrical format in human eye trackers. This sensor format allowed easier integration, minimum vision obstruction, and better safety. This cylindrical format also exhibited a superior capacitive response compared to identically sized copper sensors. Sensor placements were optimized through eye area 3D scanning, allowing the capacitive eye-tracker to achieve a high accuracy over a wide gaze angle range. The capacitive eye-tracker was also explored for fatigue monitoring using blink rate and eye closure duration biomarkers, showing a low deviation from manual counting and computer vision algorithms. The compact wearable capacitive eye-tracker allowed continuous gaze and fatigue tracking throughout the day, enabling unique applications for fatigue monitoring, cognitive research, and medical diagnostics.

In summary, the dissertation covered the design, fabrication, characterization, and eye-tracking applications of CPC capacitive sensors. The high proximity sensitivity at a small size could be ideal for wearable sensing applications.

Table of Contents

List of Figures

List of Tables

Acknowledgements

First, I would like to express my sincere gratitude to my faculty advisor Professor Jae-Hyun Chung for his trust, mentorship and continuing support throughout my PhD study. I would also like to thank my colleagues and alumni of the nano-manufacturing lab Changwoo Lee, Vigneshwar Sakthivelpathi, Zhongjie Qian, Yu-Jen Cheng, Zachary Taylor, and Scott Soelberg for their support and assistance throughout my research.

Besides, I would like to thank the rest of my committee: Dr. Robijanto Soetedjo, Professor Lucas R. Meza, Professor M. P. Anant, and Professor Youngjun Choe, for their insightful comments and encouragement.

I acknowledge the support from NSF, NIH, IP group and Somalytics.

Finally, I would like to thank my parents for their support for my Ph.D. studies and beyond.

Chapter 1. Review of the Capacitive Sensors for Wearables

1.1 Definition of Capacitance and Factors Affecting it

1.1.1 Uniform Field and Fringe Field Capacitance

Capacitance refers to a body's capacity to store an electrical charge, defined as the number of charges stored per unit of applied electrical potential. Consequentially, objects with high capacitances store more charges under the same electrical potential compared with their lower counterparts. The equation governing capacitance is:

$$C = \frac{Q}{V} \tag{1.1}$$

Here Q is the electrical charge, V is the electrical potential, and C is the capacitance. All these three parameters may have non-uniform distribution in surface or space, requiring integration.

A capacitive sensor generates an electrical field to detect environmental changes, the electrical field can be further categorized into uniform and fringe fields. The uniform field, as implied by its name, is uniform between two plate electrodes in a parallel plate configuration. This field is always parallel to plate normal (θ = 0°) and can be treated as equal at any point within both parallel plates. In an actual capacitor, dielectric materials with a dielectric constant ε_r are often used. Inside the dielectric material, the effects of polarization and free electrons can be generalized as the electrical displacement field **D**, defined as $D \equiv \varepsilon_r \varepsilon_0 E$ (see Figure 1a). By

substituting E with D for Q calculation in the dielectric material, the following relation can be established

$$C_u = \frac{Q_{free}}{V} = \frac{A|D|}{d|E|} = \frac{\varepsilon_r \varepsilon_0 A}{d} \tag{1.2}$$

Where ε_r denotes dielectric constant, ε_0 is vacuum permittivity, A is the plate area, and d is the separation between plates.

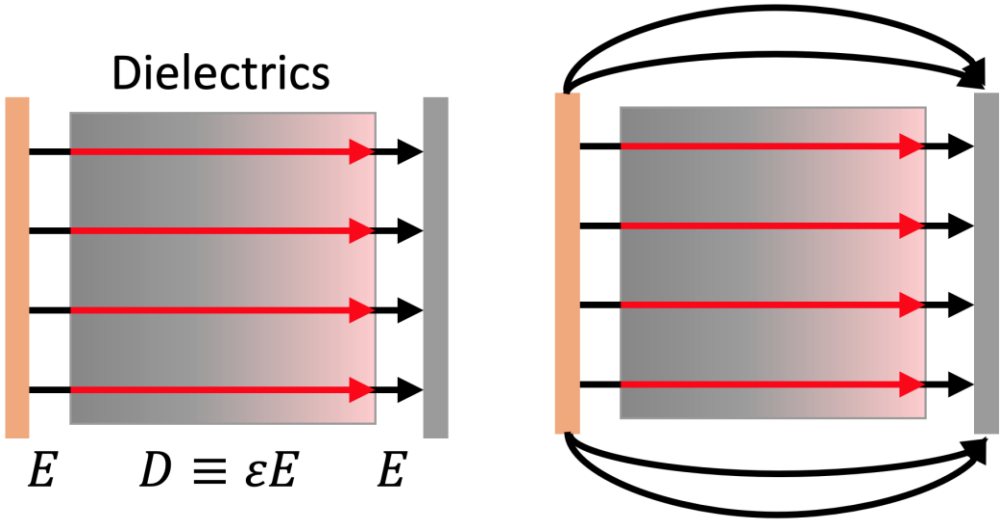

Figure 1. (a) Electrical field E and the electrical displacement field D in a parallel plate capacitor. (b) Fringing field from a parallel plate capacitor (edge effect).

This equation is commonly referred to when determining the capacitance of a parallel plate capacitor. From this equation, three ways to increase capacitance in a parallel plate capacitor are evident, which are 1) increasing the facing area, 2) choosing dielectrics with high

dielectric constant, and 3) bringing electrical plates closer. This equation, however, holds only true for the uniform field part of a parallel plate capacitor. When √A / d is high, the capacitance mostly comes from the uniform field. When the ratio √A / d becomes smaller, the edge effect kicks in. In this case, the electrical field fringes or budges outwards (see Figure 1b).

Numerous works have been published on getting a closed-form solution for the fringed electrical field. Examples includes Kirchhoff's early study [1] which found

$$C(d) = 4\pi\varepsilon_0[\frac{1}{4d} + \frac{1}{4\pi}(\ln\frac{16\pi}{d} - 1)] + O(d) \tag{1.3}$$

There are others attempt to solve the Love Integral Equation [2, 3], as.

$$f(x,d) - \frac{d}{\pi}\int_{-1}^{1} dy \frac{f(y,d)}{d^2 + (y-x)^2} = 1 \tag{1.4}$$

Nevertheless, the above equations are all based on circular condenser disks, assuming that the plate thickness is infinitely small so that the electrical flux on the side wall is 0. Getting a closed-form solution for a square-plate parallel plate capacitor is much harder as the square is less symmetric than a disk. An approximation model presented in [4-7] has a general form of.

$$C_f \approx \frac{k_1 d C_u}{\pi R}\ln\left(\frac{k_2\pi R}{d}\right); R = \sqrt{\frac{A}{\pi}} \tag{1.5}$$

Where C_u is the uniform field capacitance, as shown in Equation 1.2, and k1 and k2 can be fitted over a certain $\sqrt{A} / d$ range with results from numerical simulation, which requires the laborious task of solving Poisson's equation.

In my finite element analysis (FEA), a parallel plate capacitor was modeled as two facing 1mm-by-1mm square plates, which all had 0.1mm thickness. More details on boundary condition, mesh, and solver configuration are described in Section 2.4. The distance between the facing plane was either 0.01, 0.1, 1, or 10 mm. Using the 100kHz frequency domain electrostatic solver, the following relationship was found between fringing capacitance and uniform field capacitance (Table 1).

Table 1. Uniform field capacitance from equation (C_u), from surface integration (C^*_u), and total capacitance (C).

d (mm)	**$\sqrt{A} / d$**	**C_u by Equation 1.2 (pF)**	**C^*_u from facing plane Surface integration (pF)**	**C_u by Equation 1.2/ C^*_u from integration**	**C by simulation (pF)**	**C^*_u/ C by numerical analysis**
0.01	100	0.885	0.887	0.998	0.987	0.897
0.1	10	0.0885	0.0889	0.996	0.130	0.684
1	1	0.00885	0.0129	0.664	0.0348	0.371
10	0.1	0.000885	0.00771	0.115	0.0244	0.315

In Table 1, C_u was calculated from either Equation 1.2 or by surface integration of electrical flux normal to the facing plate then applying Equation 1.1. The capacitance from the second method was denoted C^*_u as a large part of this capacitance can be from edge effect at small $\sqrt{A} / d$, which

was not a uniform field capacitance. C was the overall capacitance accounting for all the electrode surfaces.

According to the simulation results in Table 1, when $\sqrt{A} / d$ was large (i.e., 100), uniform field C_u constituted 99.8% of all facing plane capacitance (C^*_u). However, when $\sqrt{A} / d$ was small (0.1), such ratio dropped to 11.5%. The $\sqrt{A} / d$ ratio of 10 is likely a cut-off where further lowering $\sqrt{A} / d$ could induce a significant edge effect. Similarly, the ratio between facing plane capacitance and all plane capacitance was also the highest at 0.897 when $\sqrt{A} / d$ was 100. This value dropped and saturated around 0.315. Considering these two ratios, the uniform field was not dominant when $\sqrt{A} / d > 1$.

1.1.2 Capacitor and Capacitive Sensors

Capacitors play an essential role in nearly all electrical circuits due to their capability of storing energy. Capacitors delay or attenuate sudden electrical potential changes, which trait is crucial for stabilizing circuitry under varying loads, filtering out high-frequency signals, and storing digital information, as seen in the dynamic random-access memory (DRAM). Along with resistors, the RC circuit is also capable of generating clocks at its resonance frequency.

A capacitor's function and performance are heavily influenced by its capacitance value. Therefore, it's essential to engineer capacitors such that their capacitance value remains stable over their working range; otherwise, the circuitry's functionality deviates from the design.

An ideal capacitor has no inductance, resistance, or leakage, and remains unaffected by environments such as temperature, moisture, pressure, or dielectric breakdown. An actual capacitor, while not ideal, resists the environmental changes relatively well. For example, X7R capacitors

work between -55 to 125 degrees Celsius with a capacitance change less than ±15% [8]. Besides, capacitors are usually fully enclosed to mitigate the effect of dirt, moisture, or mechanical vibrations.

Capacitive sensors, on the other hand, are designed intentionally as faulty capacitors such that their capacitance values change a lot under some environment changes. Sensors are engineered to transduce environmental changes into either geometry change or dielectric material change, which subsequently affect the capacitance.

Capacitive sensors may work on uniform field and/or fringing field, which again, is determined by the parallel plate's $\sqrt{A} / d$ ratio. Two notable examples of capacitive sensors relying on uniform field capacitance are microelectromechanical system (MEMS)-based accelerometers and capacitive liquid level sensors (see Figure 2). In a comb drive accelerometer, the fixed electrode and the movable electrode are laid out alternatively. The movable electrode is suspended on a micro-spring which elongates or compresses under force. The change of spacing between the movable and the fixed electrode causes a capacitance change, which can be measured and correlated to force and acceleration. The liquid level sensor leverages the fact that some liquids, such as water, have a higher dielectric constant than the air. Equation (1.2) accurately determines the submerged area A, and the liquid level can be calculated. In both cases, a large facing area and small spacing between electrodes guarantee a high $\sqrt{A} / d$ ratio, which is crucial for uniform field sensing. Due to the "uniformness" of the uniform field, the change of either geometry or dielectric constant can be accurately measured. However, the working area is limited to the space enclosed by electrodes, where the uniform electric field prevails.

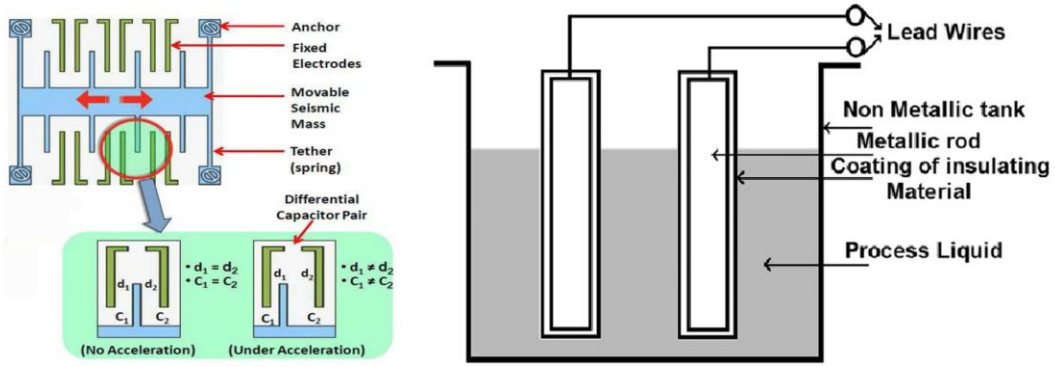

Figure 2. Schematic of a capacitive comb drive (used on a MEMS accelerometer) [9]. and a capacitive liquid level sensor [10].

A fringing field capacitive sensor, on the other hand, can sense a much larger area as its electrical field extends beyond the space enclosed by electrodes. Nevertheless, due to lacking a closed-form solution that determines the relationship between the potentially complex geometry change and capacitive response, empirical data fittings and numerical simulations are usually required to find the physical properties of the capacitive changes. Examples of capacitive sensors utilizing fringing electrical fields are various coplanar capacitive sensors. Coplanar capacitance sensors, as the name suggests, have electrodes put in the same plane. Attempting to use the parallel plate capacitor equation reveals a small facing area (in this case, sensor thickness) and a large separation, indicating a large fringing capacitance.

Coplanar capacitance sensors are favorable for several reasons. First, the electrodes for coplanar sensors are on the same layer, allowing easy and high-throughput manufacturing through the modern printed circuit board (PCB) process. On the other hand, parallel plate capacitance sensors require plate construction and assembly, or require a microfabrication process such as Deep

Reactive Ion Etching (DRIE) to create a large √A / d ratio. Besides, with no top plate blocking access, a coplanar capacitance sensor can sense the proximity of objects at a distance much larger than the size of the sensor itself and work irrespective of surface geometry. Both target object compatibility and process throughput are very important in spatial mapping applications such as touchscreen sensors matrix (see drawing at Figure 3) and gesture recognition, where thousands of electrodes are needed to sense the hand, fingers, or other objects of different shapes and distances.

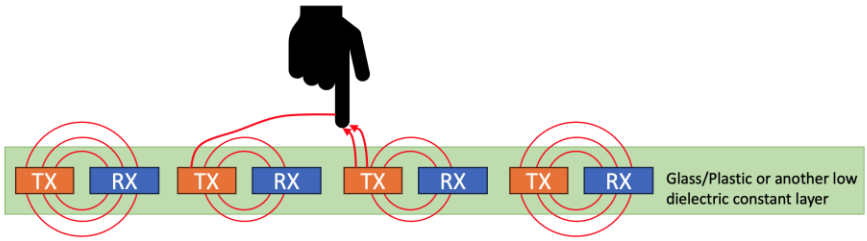

Figure 3. Drawing of a capacitive touchscreen panel.

1.1.3 Self-capacitance sensor and mutual capacitance sensor

There are two kinds of capacitive sensors based on which reference the capacitance is measured against. In self-capacitance, the capacitance is defined with respect to ground potential. Therefore, a self-capacitive sensor only requires an electrode that is not grounded and measures the capacitance between this electrode and the ground. Mutual capacitance, on the other hand, requires at least two electrodes and measures the capacitance between them. The schematic of both modes of capacitive sensing can be seen in Figure 4.

In the self-capacitance part of the diagram, the capacitance changed by sensed objects is shown as C_s. C_p is the parasitic capacitance, which involves every other charge interaction from the environment. When an object (grounded or high dielectric constant) moves closer to the self-capacitive sensor, an additional capacitive pathway forms between the sensor and the target, resulting in an increase in capacitance. In the mutual-capacitance configuration, parasitic capacitance pathways to ground C_{p1} and C_{p2} still exist but are cancellable by alternating switching electrodes on and off (see

Table 2). C_{mut}, the mutual capacitance, reduces when sensing objects are introduced as part of the electrical flux now passes through the sensing object to the ground (similar to the case of self-capacitance). But from a mutual capacitance point-of-view, this additional ground pathway reduces the capacitance between two electrodes.

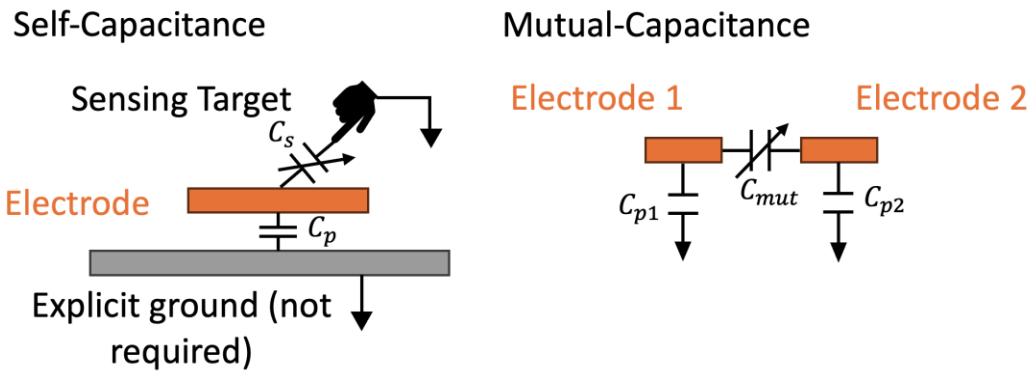

Figure 4. Schematic of self-capacitance and mutual capacitance.

Table 2. Mutual capacitance calculated as $C_{mut} = (C_1 + C_3 – C_2)/2$.

Step	Voltage Electrode 1	Voltage Electrode 2	Measured Capacitance
1	High	Ground	$C_1 = C_{p1} + C_{mut}$
2	High	High	$C_2 = C_{p1} + C_{p2}$
3	Ground	High	$C_3 = C_{p2} + C_{mut}$

For a self-capacitance sensor, the proximity sensing performance depends heavily on the ratio between C_s (sensor capacitance) and C_p (parasitic capacitance). A higher C_p increases the total sensor capacitance, making it harder to charge or discharge, which results in slower and higher power consumption. Moreover, C_p is usually variable, and a large C_p can mask tiny C_s change.

In contrast, a mutual-capacitance sensor can cancel out ground parasitic capacitances C_{p1} and C_{p2} through alternative electrode excitation. However, for all steps in

Table 2, the C_{p1} and C_{p2} are still included in measurements C_1 to C_3. A high C_{p1} and C_{p2} in a mutual-capacitance sensor system can overshadow the change of C_{mut}. A higher C_{mut} also requires a smaller electrode spacing between mutual-capacitance electrodes, limiting the range of proximity capacitive sensing.

Nevertheless, the ability of mutual-capacitance sensors to reject ground parasitic capacitance while capturing only the capacitances between electrodes is advantageous in electrode grids. In such grids, a few electrodes can form hundreds of intersections, where each of them are a limited-range mutual-capacitance sensor. Such a grid is often used in shorter-range spatial mapping applications like the touchscreen controller.

1.1.4 Single-ended and Differential Measurements

Single-ended and differential measurements are the techniques adopted by various capacitive sensors. For capacitive measurement, single-ended measurement involves a single sensor (which may have multiple electrodes and can be either self- or mutual-capacitance) with reference to a single ground. Conversely, the differential measurement captures the difference between two sensors' references to the common ground. A single-ended configuration is usually easier to implement and provides an absolute capacitance value with reference to the ground. Differential configuration requires more sensors that are referenced to the same ground and measures the difference between these sensors. Despite the complexity, the differential measurement has its own advantage. The differential measurements allow common-mode-rejection (CMR), which mitigates common noise as noise cancels each other. Moreover, the differential measurement allows better linearity of the capacitive sensor.

Consider the comb drive accelerometer in Figure 2 as an example. Without acceleration, the movable mass rests at the center so that the distances to both static plates are d_0, and capacitance to both static plates $C_1 = C_2$ (see Figure 5a). Under small acceleration to the left, the movable mass moves a small distance x to the left, which now causes an imbalance of C_1 and C_2 (see Figure 5b), where:

$$C_1 = \frac{\varepsilon A}{d_0 - x}; C_2 = \frac{\varepsilon A}{d_0 + x} \tag{1.6}$$

Calculating the Maclaurin Series from Equation 1.6, as:

$$C_1 \approx \frac{\varepsilon A}{d_0} + \frac{\varepsilon A x}{d_0^2} + \frac{\varepsilon A x^2}{d_0^3} + O(x^3);\ C_2 \approx \frac{\varepsilon A}{d_0} - \frac{\varepsilon A x}{d_0^2} + \frac{\varepsilon A x^2}{d_0^3} + O(x^3); \tag{1.7}$$

Per the definition of the differential measurement, the differential capacitance C can be defined as:

$$C = C_1 - C_2 \approx \frac{2\varepsilon A x}{d_0^2} + O(x^3) \tag{1.8}$$

Which, when compared with single-ended measurements of either C_1 or C_2, has better linearity and twice the amplitude.

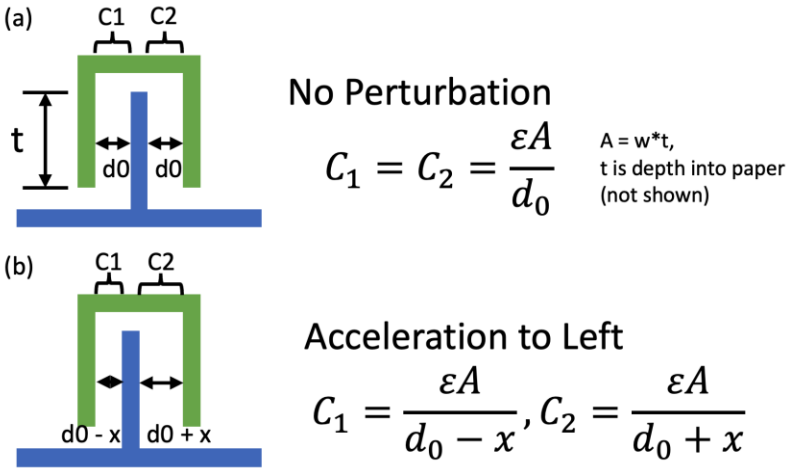

Figure 5. (a) A comb drive accelerometer at the neutral position. (b) A comb drive accelerometer under acceleration to the left side.

1.2 Capacitive Sensors for Wearable Applications

A wearable device is a general term for electronic devices worn on a user's body or attached to clothing. Common wearable devices include headphones, fitness trackers, and smartwatches. Other wearable devices include AR/VR eyeglasses, health monitoring devices, and e-textiles. These devices often integrate multiple sensors. For example, photoplethysmography (PPG) sensors use a diode and photodetector to measure heartbeats by tracking the change in blood volumes [11]. Accelerometers are commonly used for tracking human motions including workout performance [12], sleep quality [13], heart rate and respiratory rate [14], and blood pressure [15]. More advanced medical biosensors can detect early signs of illness and disease by analyzing subtle chemical changes from sweat, interstitial fluid, or skin secretions.

Various research results on applying capacitive sensors on wearable devices have been demonstrated. Compared with other types of sensors, capacitive sensors are very suitable for wearable applications as the human body has a large dielectric constant, and human skin acts like

a large ground plane. Besides, various human biofunctions depend on bioelectricity. Unlike biopotential sensors or resistive sensors, capacitive sensors do not require stable skin contact, which is hard to guarantee because of human movements, vibration, sweat and dirt, and variation of body shape and hair.

Many wearable capacitive sensors are designed for user inputs. Capacitive touchscreen sensors and capacitive microphones [16] are two of the most commercially popular examples. Many researchers also explored capacitive sensors for tactile and pressure inputs. For example, Kim et al. created a passive-powered, inkjet-printed, paper-substrate sensor tag that was calibration-free and showed "rugged" performance in sensing object proximity as well as contact. They found it to have great potential in wearable and Human Machine Interface (HMI) uses [17]. Guo et al. created an electronic skin (e-skin) application that's based on flexible electrodes and carbon black (CB)/silicone rubber (SR) dielectric material. They found the device to be of good wearing comfort, good stability, and tactile perception capabilities [18]. Zhang et al. created a wearable hydrogel-based capacitive strain sensor that was highly resistant to stretching, had good durability, and retained its performance after cutting and self-healing test. They found it useful for human motion monitoring [19].

Capacitive sensors in wearables extend to environmental and physiological monitoring. Kanaparthi created a paper-based capacitive humidity sensor that was based on a pencil draw-over-stencil interdigitated electrode array. He found that the quick absorption and desorption of water molecules during exhales could be used to monitor respiratory rate [20]. Song et al. created a capacitive friction force sensor by using Silver/PDMS mixtures to create tall, interdigitated electrodes. Large electrodes showed larger deformation/ buckling when friction was applied on top. It was speculated that this sensor could be used in e-skin, human monitoring, and intelligent

robots [21]. Bijender and Kumar created pressure sensors using porous PDMS structures and demonstrated blood pressure sensing [22].

In subsequent chapters, I will delve into my research on a novel microstructure-enhanced capacitive sensor, exploring its applications in HMI and wearable eye-tracking applications.

Chapter 2. Ultrasensitive Capacitive Sensor and the Human-Machine Interface

Acknowledgment of Previous Publication

This chapter was also published as T. Li, V. Sakthivelpathi, Z. Qian, S.-J. Kahng, S. G. Ahn, A. B. Dichiara, K. Manohar, J. H. Chung, *Ultrasensitive Capacitive Sensor Composed of Nanostructured Electrodes for Human–Machine Interface*. Adv. Mater. Technol. 2022, 7, 2101704

2.1 OBJECTIVE

This chapter introduces the Carbon-Nanotube-Paper-Composite (CPC) material and its application as a capacitive sensor. CPC materials contain numerous conductive cellulose fibers with high surface-area-to-volume ratio and aspect ratio. This unique geometry increases the sensor's total surface area and electric field strength, enhancing its capacitive sensitivity.

In this chapter, I will first discuss the fabrication of the CPC material and sensors. Then I will evaluate the CPC capacitive sensor's performance through finite element analysis (FEA) and benchmarking against reference silver sensors. Finally, I will demonstrate some applications in Human-Machine-Interface.

2.2 INTRODUCTION

Human-machine interfaces (HMIs) have rapidly evolved due to advancements in artificial intelligence and Industry 5.0. Sensors play a crucial role in HMI implementation by detecting voice, force, body motion, and gestures to enhance efficiency in industrial- [23, 24] and healthcare [25-27] sectors. Among these, motion and gesture sensing receive lots of attention as they provide key human behavior inputs for efficient communication, process control, and safety assurance. Common motion-sensing technologies include cameras, radar, electromagnetics, infrared, and capacitance sensing [28-30]. Among these, capacitance sensing stands out for its ability to detect both proximity and contacts at a lower cost and power consumption than camera-based or radar-based technologies.

Traditional capacitive sensors, however, lack flexibility and sensitivity for HMI applications such as wearables. Recent researchers have found nanostructures or nanomaterials integration into electrode designs can lead to improved flexibility [31]. Li et al. created a flexible capacitive sensor by printing copper traces to form crossing junctions [32]. Murai's group used silver-plated-fiber electrodes and compressible silicone dielectric to create a motion-sensing leg band whose electrical conductivity was still guaranteed under high tensile strain and bending [33]. Qin's group created a flexible touch sensor by printing the silver nano-ink onto a PET film [34]. Frutiger et al. enclosed ionized liquid into the silicone to create a flexible capacitive strain sensor [35]. Tsuji and Kohama's self-capacitance sensors can detect humans at 120 mm but at a size of 100 mm by 70 mm [36]. Moheimani et al. created Thermoplastic Polyurethane – Carbon nanotube (TPU – CNT) film sensors that can measure up to 120 mm at a size of 60 by 20 mm [37]. Despite their mechanical performance, wearability, and durability, these new forms of capacitive sensors do not particularly stand out for their sensing performance.

In this chapter, I present a capacitive sensor composed of nanostructured paper electrodes. The carbon nanotube-embedded cellulose fiber construction provides high sensitivity from a large surface area and high aspect ratio, reduces parasitic noise and maintains flexibility. The sensing mechanism is studied through numerical and experimental studies demonstrating that the proposed capacitive sensor is better than similar silver sensors in proximity and pressure sensing. A smart pad with several functionalities will also be showcased.

2.3 Carbon-Nanotube Composite Based Capacitive Sensor

2.3.1 The Carbon-Nanotube-Paper-Composite Electrode

The CPC material were made in a similar way as previous art [38, 39]. In short, cellulosic pulp suspension pre-adsorbed with cationic polyacrylamide (CPAM, Percol 3035; BASF, RP, DE) was mixed with 10 wt.% MWCNTs (Cheap Tubes Inc., VT, U.S.A.) dispersed in aqueous sodium dodecyl sulfate (SDS) (Sigma Aldrich, MO, U.S.A.). The mixture was subsequently filtered, pressed, and dried to form electrically conductive carbon nanotube paper composites (CPC). MWCNT in CPC forms an electrically connected Random Fiber Networks (RFN), where MWCNTs intersect each other to create random electrically connected paths that increases the conductivity of a normally non-conductive paper material.

The creation of electrically connected Random Fiber Network (RFN) depends heavily on the Van der Waals force (VDW) and the electrostatic force (ES). VDW forces are always attractive. However, VDW is proportional to surface area and inversely proportional to intermolecular distance to the 6^{th} order [40, 41], which makes VDW forces prominent at smaller distances (especially at a distance between 0.1 and 10 nm). ES is proportional to body charge, which is

directly correlated to volume but only proportional to the distance to the 2nd order. As a result, repulsive ES is much more dominant when molecule and intermolecular distances are large. CNTs are chosen because of its small diameter, where the single-walled carbon nanotube (SWCNT) has a diameter of 1 nm and MWCNT about 3-20 nm, at the same time, their length can easily go over 1000 nm [42-44]. As the diameter decreases, the spacing between neighboring CNTs reduces, and the surface area to volume ratio increases (see Equation 2.1).

$$\frac{A}{V} = \frac{\pi dL}{\frac{\pi d^2 L}{4}} = \frac{4}{d} \tag{2.1}$$

As a result, MWCNTs experience larger attractive VDW forces compared with repulsive ES force. Besides, their length allows multiple connected pathways to form even with a lower MWCNT density. Therefore, MWCNTs are frequently employed to make paper electrically conductive.

Silver paste (MG Chemicals, USA) was applied and cured to both ends of CPC strips with various widths (i.e., 1, 3, 5, and 10 mm). Deionized water was printed three times over the planned fracture site using a 0.8 mm-diameter capillary pen. After that, tension was slowly applied to both ends of CPC, causing CPC cellulose fibers to delaminate and fracture. The water-enhanced fracture process creates numerous conductive cellulose fibers extending out of the fracture site. The whole manufacturing process, as well as sensors being made, can be seen at Figure 6a.

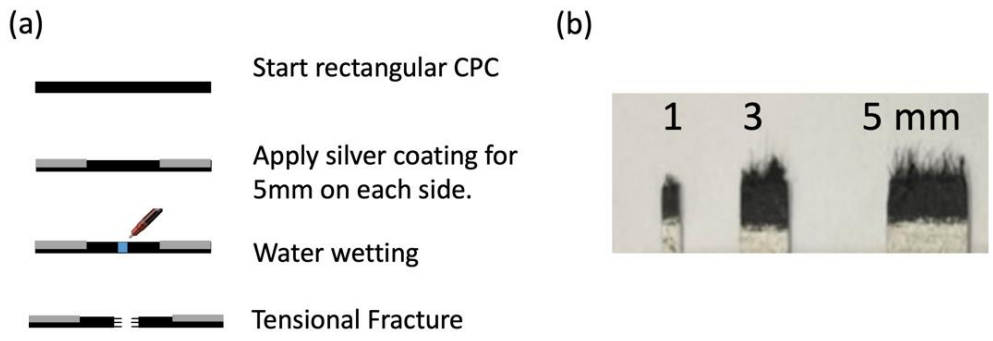

Figure 6. (a) The water fracture process (b) Fibrous CPC sensor of varies width being made.

2.3.2 Properties of CPC Fibrous Electrode

Conductive cellulose fibers were inspected by optical microscopy and scanning electron microscopy (SEM) to determine geometric parameter including the linear density, defined as number of individual fibers per mm CPC width, average length, and average thickness, and aspect ratio (see Figure 7).

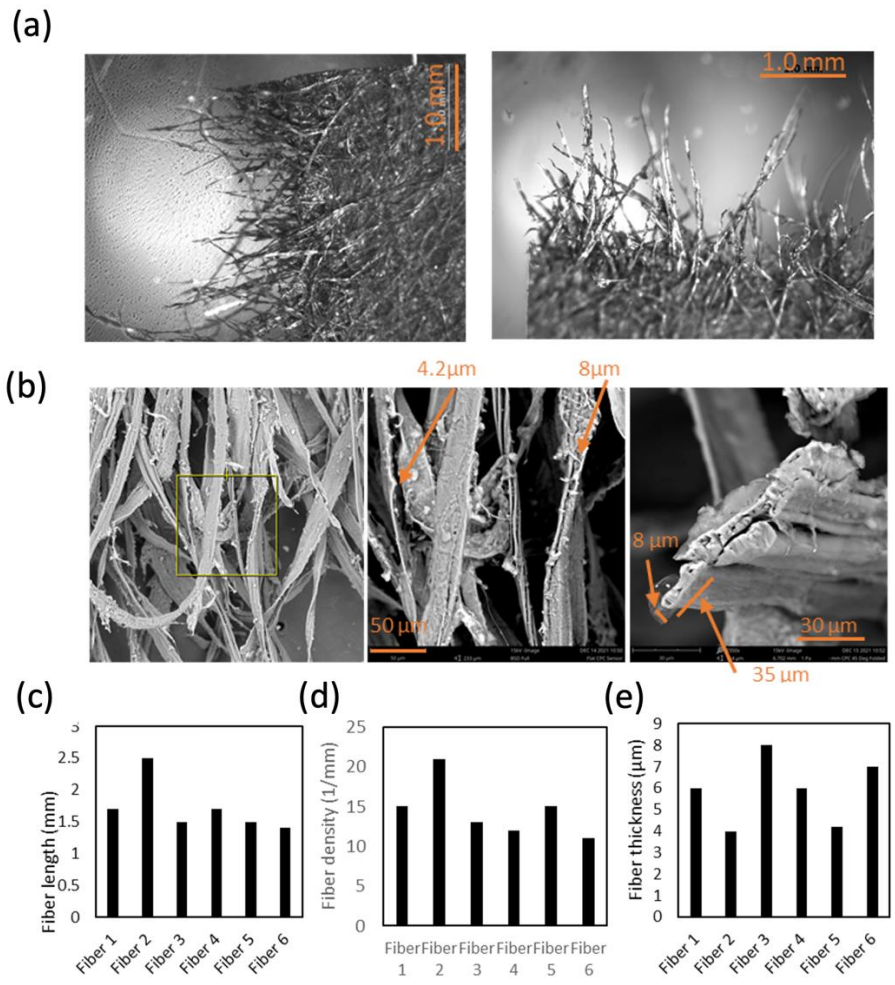

Figure 7. (a) Optical microscopy showing the fracture site of the sensor. (b) SEM images showing the thickness and structures of individual cellulose fiber. (c) Averaged fiber length among 6 fibers measured. (d) Averaged fiber linear density, defined as the number of fibers per mm CPC. (e) Thickness of the fiber.

Additionally, three fibers were separated with a tweezer and fixed onto a 100 µm-thick polyethylene terephthalate (PET) using the same conductive silver epoxy applied at the fiber end. Their resistance value was measured with a multimeter and converted to conductivity using the

averaged fiber size measurements (see Figure 8). All measurements have been summarized in Table 3.

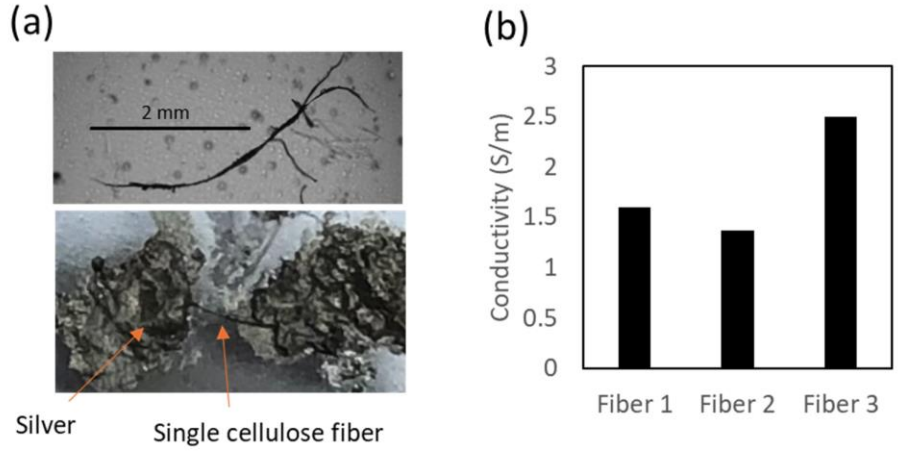

Figure 8. (a) Single cellulose fiber fixed by conductive silver epoxy. The measurement is through the silver epoxy on both ends. (b) The calculated conductivity for 3 single fibers.

Table 3. Characterization of fibers created with water fracture process.

Metrics	**Value**
Average Fiber Linear Density	14.5 ± 3.6 mm^{-1}
Averaged Fiber Length	1.71 ± 0.4 mm
Averaged Fiber Thickness	5.9 ± 1.6 μm
Aspect Ratio	200 to 490
Averaged Conductivity	1.8 ± 0.6 S/m

Beyond fibers, the bulk CPC itself will also deform under this tensile fracture. CPC exhibits auxetic behavior, which is defined as negative Poisson's ratio, in the out-of-plane directions when under the stress [45]. Auxetic behavior can be achieved in engineered structures, such as chiral structures, re-entrant structures, or rotating rigid squares [46-48], as well as some materials, such as paper and non-woven fabrics [49, 50], due to its internal structures. CPC, as a paper-based material, shows auxetic behavior when fractured [51]. The buckling fibers can cause a negative Poisson's ratio as much as over -200 [52].

During fracture, the fibers skid and self-align. This phenomenon can also be visualized in Figure 7a, where the cellulose fibers in fractured site were much aligned when compared to the unfractured part. As a result, compared with the RFN in the unfractured part, the RFN in the fractured part has a much larger thickness, much more parallel alignment, but lower conductivity due to the breaking of conductive pathways. Prior research had demonstrated this effect (as seen in Figure 9).

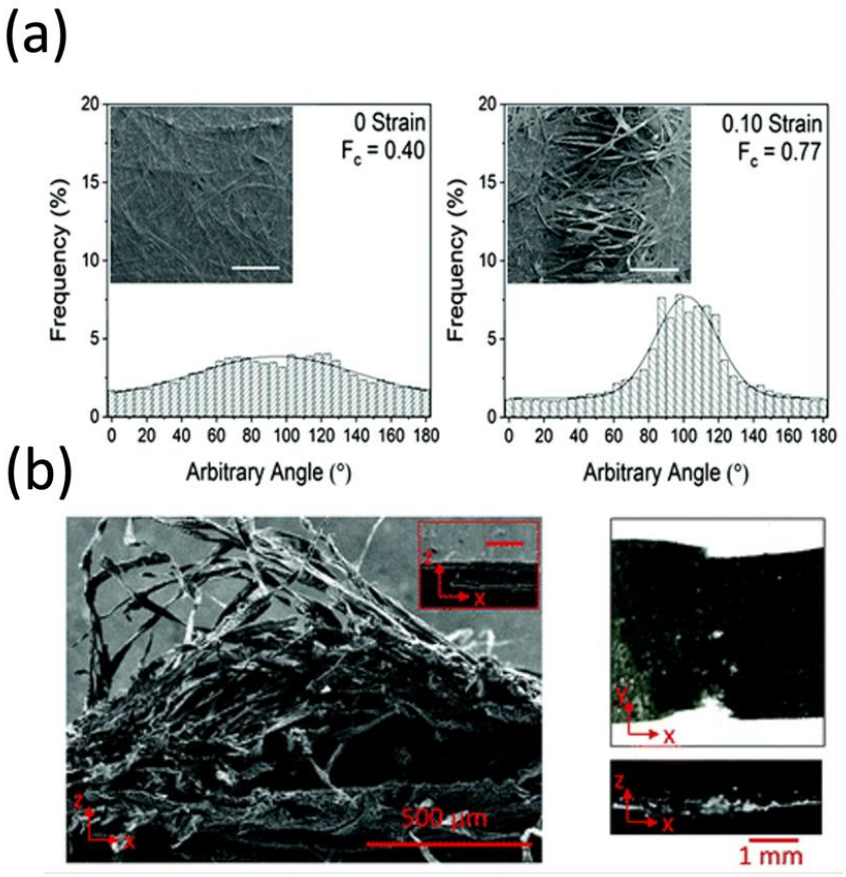

Figure 9. (a) SEM images and fiber orientation of 2.5 CNT wt%-CPC at strain of 0, and 0.10. (Scale bar: 500 µm) (b) Left: SEM image of fractured CPC with 10 CNT wt% at strain of 0.10. Inset: SEM image of pristine CPC. [38]

2.3.3 Electrode configuration of a CPC Capacitive Sensor

Capacitive sensors of different configurations were fabricated using CPC electrodes and silver electrodes. A silver electrode was fabricated by coating silver ink over a 100 µm-thick PET film. To highlight the geometry difference, I define the CPC electrode as Fibrous electrode (F), and silver-based electrode as Rectangular (R). Five configurations were made:

- Paired Fibrous (PF): Two Fibrous electrodes.
- Paired Rectangular (PR): Two Rectangular electrodes.
- Single Fibrous (SF): Single Fibrous electrode.
- Single Rectangular (SR): Single Rectangular electrode.
- Paired Hybrid (PH): One Fibrous and one Rectangular electrode.

2.4 SENSOR NUMERICAL STUDIES --- HAND PROXIMITY SENSING

Numerical simulation using the COMSOL Multiphysics were conducted to evaluate the proximity sensing performance of the above electrode configurations. Usually, sensor's sensitivity is defined as the $\Delta C/C_0$, where $\Delta C = (C_1-C_0)$. C_1 and C_0 are capacitance values with or without sensing objects. In my research, I defined the parameter as $\Delta C = (C_1-C_0)$, instead of $\Delta C/ C_0$. This decision can be justified as C_0 was small (C_0 below 0.5 pF due to the small form factor). As a result, factoring the ΔC as sensing capacitance/ circuitry capacitance with such a small baseline creates high percentage error. Besides, the capacitive-to-digital-converters (CDCs) I used were Analog Devices AD7747 and Texas Instrument FDC1004, both of which offer high resolution as low as $0.5*10^{-15}$ F (i.e., 0.5 fF).

The electrode design was analyzed based on three-dimensional modeling. The fibrous electrodes were modeled as four separated cantilevers. Each cantilever has a length of 1mm and a cross-section of 10μm-by-10μm. The rectangular electrode was modeled as a monolithic 1mm-by-40μm-by-10μm cantilever. Both electrodes were oriented with their central axis colinear, and their spacing was 1mm (spacing only applicable to PF, PH, and PR). The air boundary was modeled as a 25mm width cube, and the target object was represented as a sphere whose radius was 5mm

and suspended 5mm (measured from the bottom) above the sensor. The details of modelling can be seen at Figure 10.

A potential concern was representing numerous irregular fibrous electrodes for four equally distributed cantilevers. While modeling every fiber was impossible, simulation results showed that sensor capacitance quickly saturated after a linear density of 8. Microscopy result showed that the sensor has a linear density averaging 14.5 fibers per mm width, indicating the current model is likely to perform sufficiently well in modeling the actual sensor.

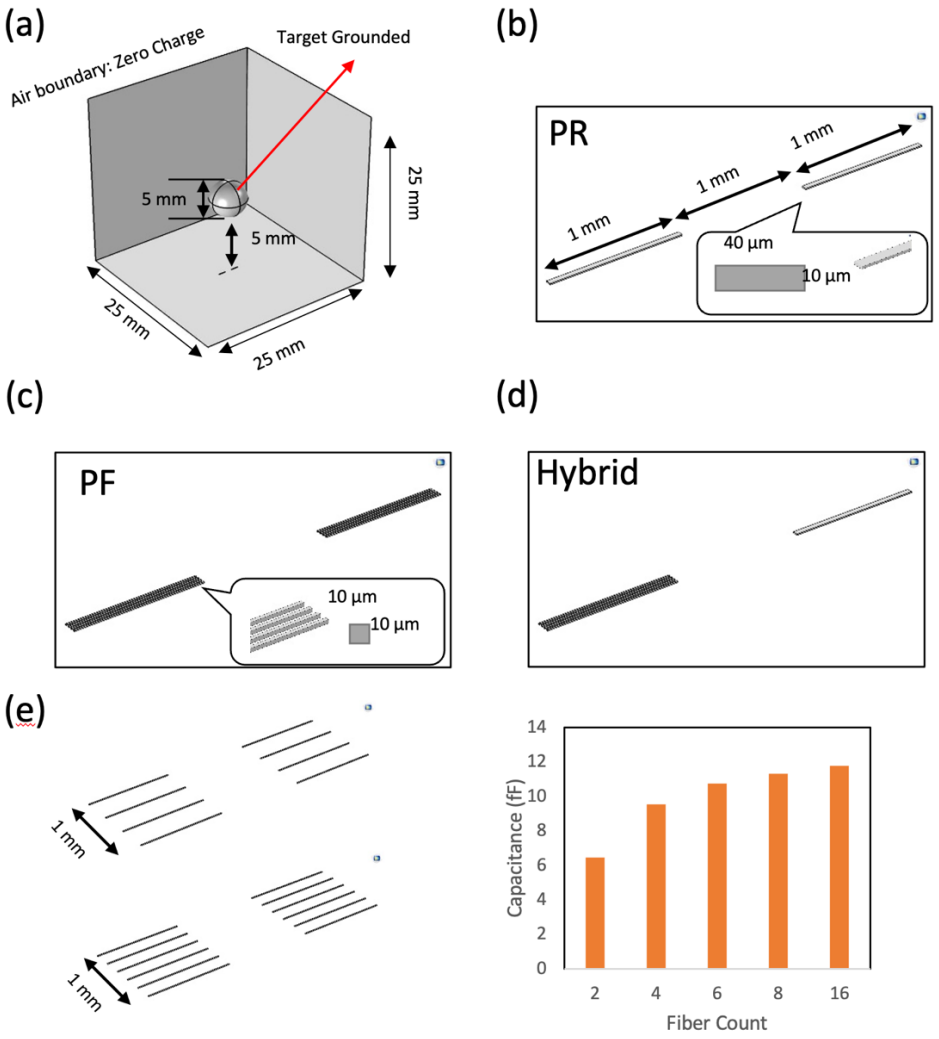

Figure 10. (a) Isometric view of the model (with front surfaces hidden). (b) Paired Rectangular configuration. (c) Paired Fibrous configuration. (d) Paired Hybrid configuration. (e) Increasing the linear density in the simulation. (f) The capacitance changes quickly saturated after a linear density of 8.

The electrostatics solver provided by COMSOL's AC/DC module was configured to a 100 kHz frequency response mode. The sensing electrode used a 5V fixed voltage terminal constraint such that the internal variation was all ignored. For PH, PF, and PR, the other electrode was

assigned as ground terminal. The target was also defined as ground. The air boundary was defined as zero-charge, which, per COMSOL documentation [53]. In other words, the electrical displacement field (D) will not pass, thus no flux.

$$n \cdot \vec{D} = 0 \tag{2.2}$$

The dielectric constant of the target was defined as 80, and the air's dielectric constant was 1.

The mesh was manually configured such that it had a minimum cell size equals to the minimum feature size in the model (10 μm), but a higher growth rate (1.5). This configuration ensured all features can be modeled while the mesh was not over-refined. The self-capacitance value from the sensor can be calculated from the impedance of sensor as:

$$Z = \frac{1}{Y} = R + \frac{1}{j\omega C} \tag{2.3}$$

Where Z is the impedance of the sensor, Y is the admittance, R is resistance, ω is the frequency (in rad/s), and C is the capacitance. As a result, the capacitance can be found from the imaginary part of the terminal admittance Y_{11}, as:

$$C = \frac{imag(Y_{11})}{2\pi * (100kHz)} \tag{2.4}$$

The capacitance was modeled as a lumped parameter for the whole electrode. Besides, the streamline of the electrical field as well as color-coded electrical field norm was also reported.

The electric field distributions of the different paired electrode configurations were modeled both without (Figure 11a) and with (Figure 11b) the presence of the sphere. The left and right electrodes in the PH configuration consisted of fibrous and rectangular-shaped electrodes, respectively. When the target is not present, due to the zero-charge boundary condition of the air boundary, all flux exiting the sensor electrode must enter the ground electrode, causing a parasitic capacitance to exist between them. CPC sensors have a larger surface area, which led to C_0 rise in the sequence PR, PH, PF.

After the introduction of the grounded sphere, the electrical flux between the sensor and sphere accounts for 88% to 98% of the total outward flux. In this state, the capacitance value C_1 is relatively independent of the parasitic capacitance to the grounded electrode. Results show that the fibrous electrode has the higher C_1 when the spherical target is present (see Figure 11c). Nevertheless, the CPC based sensor also increases the baseline capacitance C_0. Therefore, among all paired sensors, PH showed the largest ΔC. ΔC could be further improved by removing the ground electrode in the paired configuration, which effectively turned the paired sensors into single sensors either SF or SR. This modification, however, caused electrical flux to have nowhere to go (as the air boundary does not take flux) and therefore couldn't have a capacitance value. I considered C_0 equaled to 0 fF assuming infinite distance ground. With a stable C0, single electrode configurations demonstrated higher ΔC. Owing to its larger surface area, SF exhibited the largest ΔC (Figure 11d). Experiments on these sensors will be reported in the next section.

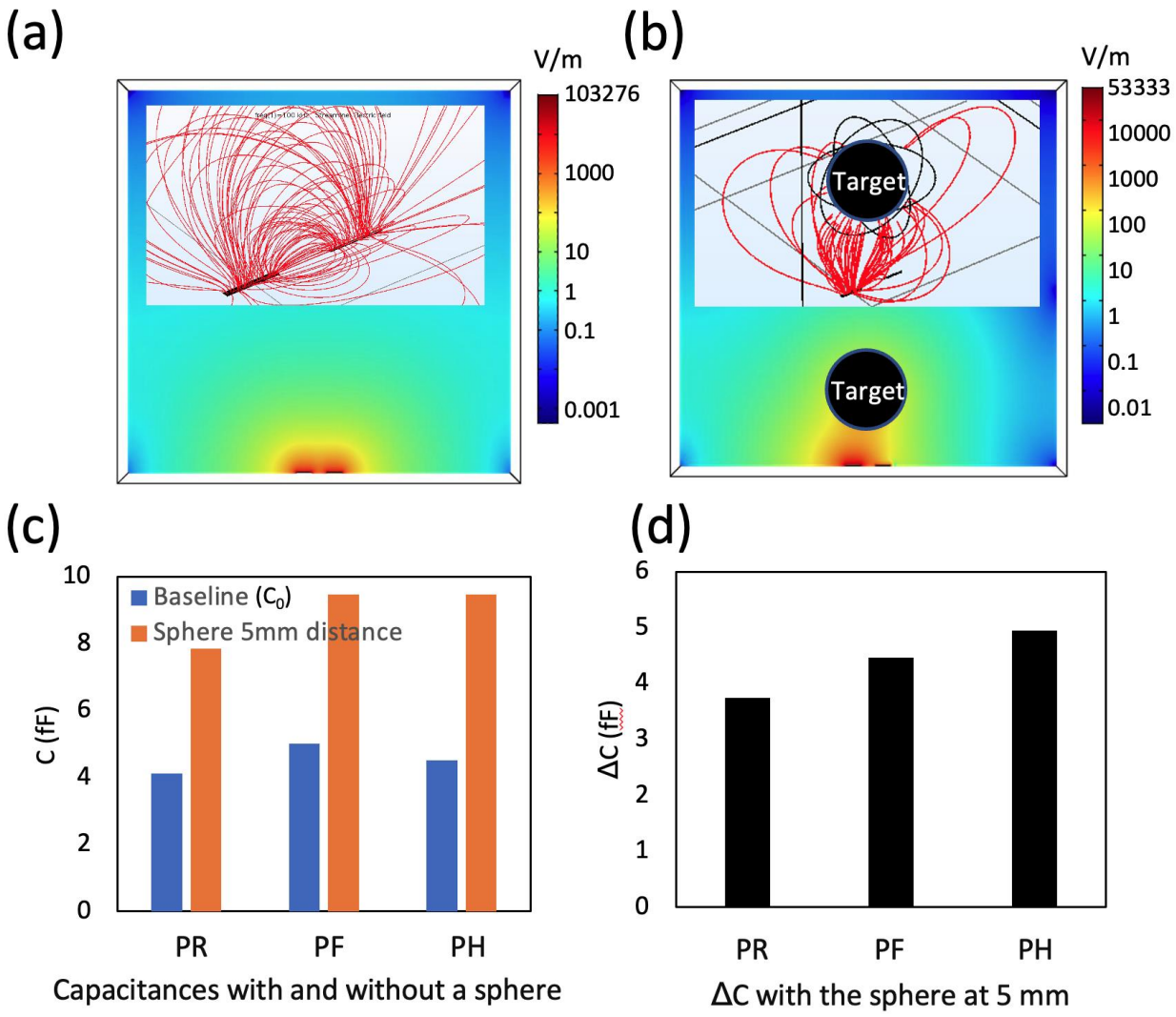

Figure 11. (a)(b) Electrical field norm and streamline without/ with a grounded sphere. (c) Baseline capacitance and capacitance with sphere target. (d) Change of capacitance caused by introduction of the sphere target.

2.5 Sensor Characterization --- Hand Proximity Sensing

CPC fibrous sensors of 1-, 3-, 5-, and 10-mm width were fabricated. Silver rectangular electrodes of 1-, and 10-mm width were also built for reference. Sensors were connected to a CDC

chip (FDC 1004, Texas Instruments) which measured the capacitance of the sensor and reported the value through a microcontroller (Arduino Nano).

To test the proximity response of the sensor, I connected the sensors to rigid wires made from 1mm wide silver-coated PET film, and maintained uniformity in sensor size, wiring, and location throughout the experiment. The proximity experiment spanned distances between 40 to 300 mm from the hand to the sensor, a range best fitted for expected applications (see Figure 12a).

PR, PF and PH sensors were first tested and their ΔC values were compared (Figure 12b). As hand approached from 300 mm to 40 mm, the reference PR sensor showed a mean capacitance increase of 42.8 ± 8.5 fF. The PF sensor exhibited a larger 78 ± 6.2 fF increase owing to the fibrous electrode's greater surface area. For the PH sensor, its response depends on polarity. When the fibrous electrode was the excitation, the responses is similar to PF at 78.6 ± 8.1 fF, the other way around the response was 109 ± 11.1 fF. Results can be seen in Table 4. However, silver-driven PH is not shown in Figure 12 as the coupling between a silver positive and CPC ground was unstable and very affected by environment. Within each test, the setup had a peak-to-peak noise around 4 fF. Using this value, the PH sensor has a maximum 150 mm range.

Echoing simulation results, Single Rectangular (SR) and Single Fibrous (SF) sensors had higher ΔC than the PR, PF, and PH sensors. In the experiment, excitation was connected to the electrode. The 1 mm width SR reference showed a 130 fF ΔC, already exceeding the most sensitive 109 fF PH value. The 1 mm SF sensor exhibited 171 fF, with wider widths leading to higher ΔC. The 10 mm SF sensor doubled paired sensor responses with 246 fF, enabling differences noticeable at 300 mm (see Figure 12c, Table 4). Thus, the most sensitive 10 mm SF sensor was used in later experiments.

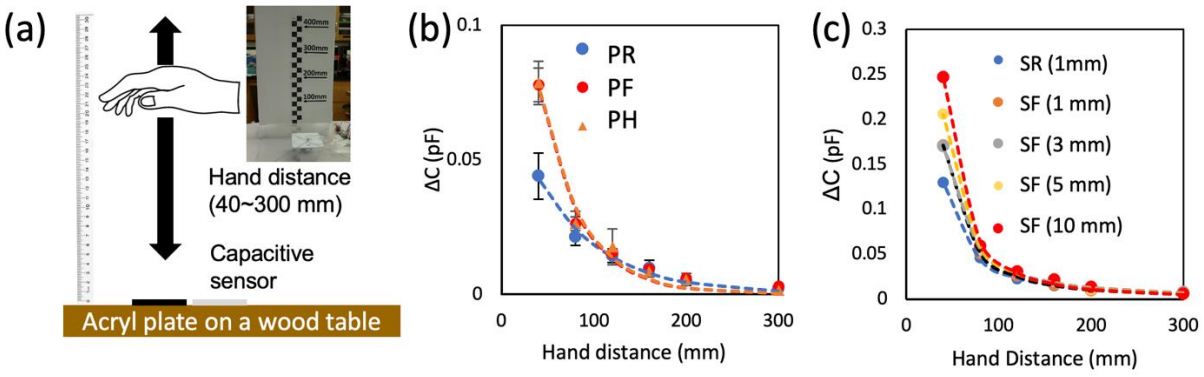

Figure 12. (a) Setup for hand proximity detection at the distance of 40~300 mm. (b) ΔC of hand proximity for 40~300 mm using PR, PF, and PH sensors. (c) ΔC of hand proximity for 40~300 mm using SR of 1mm width and SF sensors of 1, 3, 5, and 10 mm-widths. The most sensitive SF (10 mm) has an empirical relationship $\Delta C\ (pF) = 313.8 * x^{-1.929}$ (x in mm).

Table 4. Sensor type, material compositions, and the capacitance change from 300 mm hand-sensor distance to 40 mm.

Type	**Electrode Configuration**	**Capacitance change (fF)**
PR	Both Silver	42.8 ± 8.5
PF	Both CPC	78 ± 6.2
PH	One Silver, One CPC	109 ± 11.1 (Silver Excitation) 78.6 ± 8.1 fF (CPC Excitation)
SR	One Silver	130
SF	One CPC	171

2.6 SENSOR CHARACTERIZATION --- PRESSURE SENSING

2.6.1 Transitional Finger Proximity - Contact Sensing on Single Sensor

For the finger force testing, we positioned 10 mm-wide SF and SR sensors on an acrylic plate with a load cell installed below (Figure 13a).

To assess sensor variability, 6 SF and 6 SR sensors (10 mm-width, N=6) were fabricated. The baseline parasitic capacitance, considering only the circuitry, was around 2.67 pF. The averaged parasitic capacitance was 2.89 ± 0.016 pF for 6 SR sensors, and 2.95 ± 0.013 for 6 SF sensors. This discrepancy highlights that C_0 of CPC-based SF sensor is larger than silver-based SR sensor (Figure 13b).

The capacitance parameter ΔC was defined as ($C_1 - C_0$) where C_0 was the value without finger, C_1 where applied force equals to 1.5N. Under a finger force of 1.5 N, the SF sensor's ΔC peaked at 8.26 pF, contrasting with the SR sensor's 5.36 pF (Figure 13c). Importantly, the SF sensor showed a continuous capacitance increase with rising finger force. When the fibers were pressurized by a finger, more conductive pathways formed inside the random fiber network (RFN), increasing the overall conductivity and capacitance, which is unique to the CPC fibrous sensor.

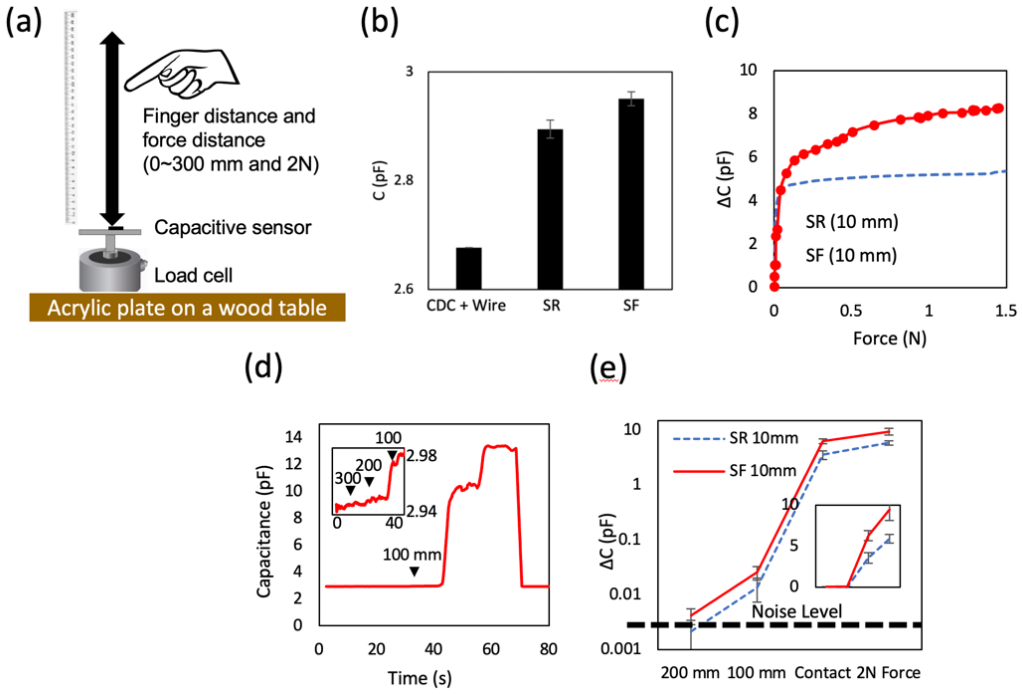

Figure 13 (a) Setup for the transitional proximity and contact sensing. (b) Capacitance of circuitry, SR (10 mm), and SF (10 mm) sensors (N=6). (c) Finger force and capacitance relationship for 10 mm-wide SR and SF sensors. After 0.04N, $\frac{\Delta C}{\Delta F} = 1.566\, pF/N$ for 10 mm SF and $\frac{\Delta C}{\Delta F} = 0.3429\, pF/N$ for 10 mm SR. (d) Time-dependent ΔC at the distance of 300~0 mm followed by the finger force of 0~2 N. (SF-10 mm width). (e) Comparison of ΔC at the distance of 200~0 mm followed by the finger force of 0~2 N (SF and SR with 10 mm width, N=6).

In the transitional proximity–force sensing, the capacitance change was continuously measured at distances of 300, 200, 100, and 0 mm, followed by the finger contact at 2 N-force with a total of 6 replicates (Figure 13d). As the index finger approached from 300 to 0 mm and pressed a sensor with a force of 2 N, ΔC increased exponentially (Figure 13e). The inset showed the exploded view of the capacitance at the 300~100 mm distance range.

2.7 SENSOR APPLICATIONS

2.7.1 Water Level Measurement

The capacitive response of an SF sensor showed the potential to measure an object based on the pressure. SF capacitive sensors with widths of 1, 3, 5, and 10 mm were tested on water level sensing. A 100 μm-thick PET film covered the sensor to prevent accidental water damage (Figure 14a). Both glass and metal cups were placed above the sensor and subsequentially filled 30 mL of water at 10 mL increment.

In Figure 14b (top panel), the capacitance change showed spikes with each water addition. These spikes were caused by the hand and container proximity during pouring. The reading was taken after pouring finished. For the glass cup, first 10 mL caused a ΔC of 140 fF. Subsequent water pouring contributed around 10 fF for each additional 10 mL. The larger ΔC from the initial 10mL water likely came from water filling the container bottom, which was polarized, forming an electrical double layer. Subsequent water addition experienced a decrease of response due to the polarization of the first layer of water, which greatly attenuated the capacitive response.

In contrast to a glass cup, a much more polarizable metal cup increases the C_0 by 1.593 pF (bottom image of Figure 14b). For a 1 mm-wide SF electrode, the addition of the 10 mL water showed ΔC of -3 ~ 0 fF. The negative change of ΔC was shown because of the limited capacitance of an SF electrode due to the limited surface area.

Figure 14c shows ΔC for 10, 20, and 30mL water in a glass cup for a 1 mm-wide SR sensor (shown as 0 in Figure 14c due to being a SR rather than a SF sensor) and 1, 3, 5, and 10 mm wide SF sensors. ΔC increased with the width of sensor.

Figure 14d shows ΔC for 10, 20, and 30 grams of water in a metal cup for a 1 mm-wide SR sensor (shown as 0) and 1, 3, 5, 10 mm-wide SF sensors. ΔC of a 1-mm wide SR sensor showed a negative value (-18 fF) due to the limited surface area and charge leakage. As the width increased from 1 to 10 mm, ΔC increased to 18 fF for a 10 mm- wide SF sensor.

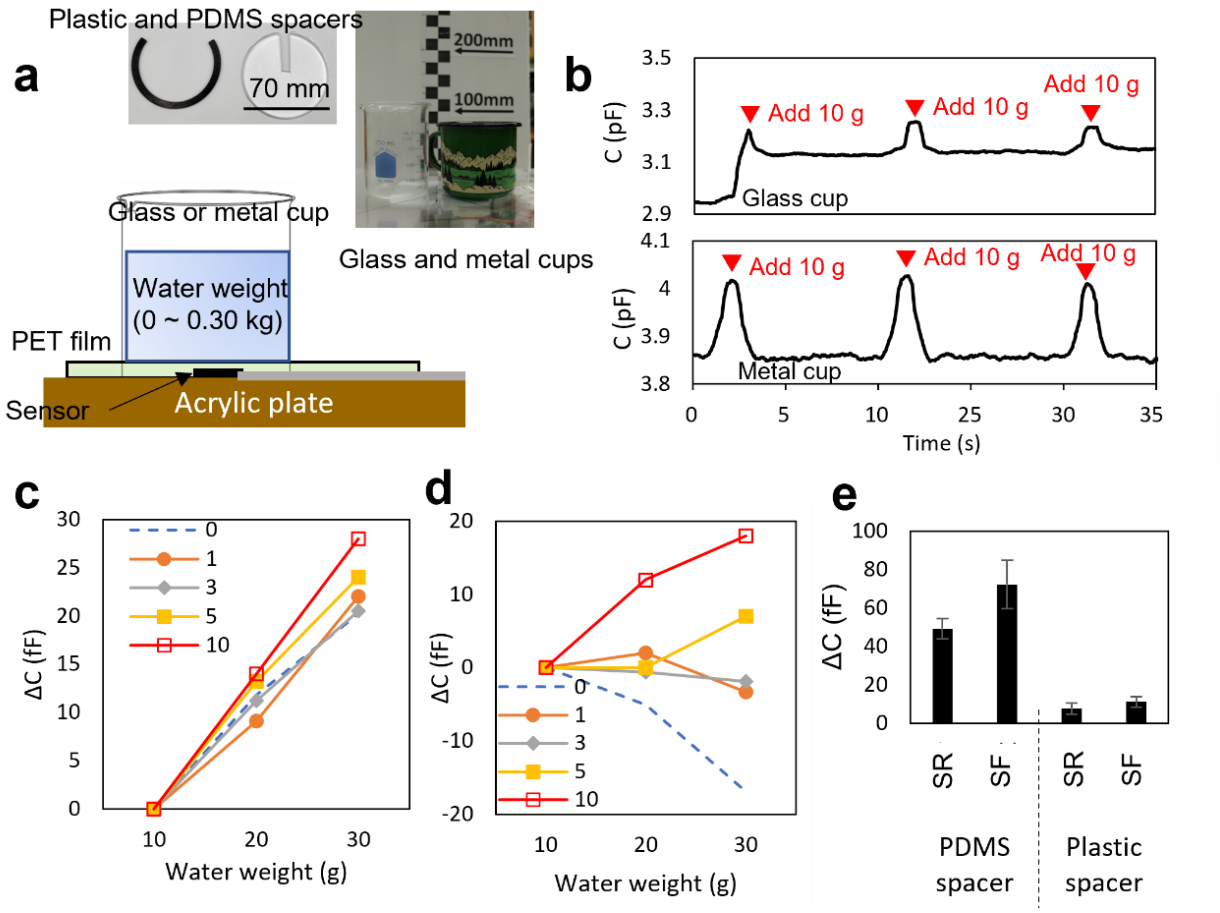

Figure 14. (a) Setup for water volume measurement in glass and metal cups. The weights of glass and metal cups are 103 and 154 g, respectively. (b) Time-dependent C for glass and metal cups (SF 1 mm-width). The initial capacitance was measured with glass or metal cups on the sensor. (c) ΔC of 10 mL-water supply in a glass cup. SR (1mm width, shown as 0) and SF (1-, 3-, 5-, and 10-mm widths) sensors are used. (d) ΔC of 10 mL-water supply in a metal cup. SR (1mm width) and SF (1-, 3-, 5-, and 10-mm widths) sensors are used. (e) Comparison of ΔC with PDMS and plastic spacers. (10 mm wide-SF and SR sensors, N=6)

It was unusual that small water additions could be measured through a metal cup. I hypothesized that the ΔC increase could be attributed to the increase of either pressure or charge.

To perform a controlled test, the 2mm-thick polydimethylsiloxane (PDMS) pad or 2mm-thick hard plastic ring was placed between the cup and sensor (Figure 14a). PDMS was preferred for a pressure test because of its similarity to human finger and its compliance, which made pressure distribution even across the sensor surface. The compliant PDMS spacer should compress under load, increasing capacitance through both pressure and a smaller sensor-cup gap. In contrast, the rigid plastic ring did not deform much under small pressure, allowed isolated charge detection.

In the experiment, 10 mm-wide SF and SR electrodes were located under the center of either PDMS or plastic spacers. An initial water of 20 mL was added to a metal cup to form the initial water layer. After the capacitive measurement was stable, 250 mL more water was supplied.

For the PDMS padded test, a full 270 mL of additional water caused an ΔC of 47 fF and 75 fF for SR and SF sensors, respectively (N=6, Figure 14e). In comparison, for the plastic ring test, the ΔC of SR and SF sensors were only 3 and 8 fF. This difference indicated pressure was the dominating mechanism for this sensitivity, with increasing charge accounted for 10 % of ΔC. To confirm this, we stacked a 290-gram porcelain container (which has a low dielectric constant) on top of the empty metal cup and observed a ΔC of 65 fF on a 10 mm-wide SF sensor. In contrast, the 270 mL of water causes around 75 fF of capacitance change.

Compared to SR sensors, SF sensors demonstrated stronger capability in sensing liquids under both pressure and charge mechanisms. Some of the enhancement was due to larger water polarization from the stronger electrical field generated by the conductive cellulose fiber structures. More importantly, the random fiber network (RFN) of the CPC sensor were pressed together to form new electrical pathways, which increased the conductivity and capacitance even at a small compression.

2.7.2 Capacitive Smart Plate

I created a sensing platform, dubbed “Smart Plate”, by utilizing four sensors and the same CDC-microcontroller combination (FDC1004, Arduino Nano) (Figure 15a). The plate performed spatial mapping and water measurements at 18 Hz.

The smart pad comprised four 10mm wide SF sensors. The detectable range of the hand was 300 mm. Changing SF sensors to similar sized PH sensors decreased detection range to below 30 mm. This can be caused by a larger parasitic capacitance.

Nevertheless, a catch of the SF sensor is that it’s more affected by surroundings. When situated near the ground or highly polarizable materials, the hand proximity detection range drops noticeable. Attaching the plate to a door, concrete floor, a metal desk, and a bio-cabinet reduced the hand detection range to 150, 90, 50, and 50 mm, respectively (Figure 15b). Still, 50 mm was considered remarkable for SF proximity sensor when fully enclosed by metal shelves.

To aid the detection of hand location, I performed a COMSOL to study how capacitance on each sensor changes when as a hand moved over them. In the simulation, the whole pad was segmented into a 16 x16 grid centered at (0, 0, 0) with a cell size of (12.5 mm by 12.5 mm) (see Figure 15c). Sensors were modelled as rectangles in quadrant center. In proximity sensing, the hand was modelled as a flat cylinder moving from 1 to 4 mm above the pad. For spatial mapping, the cylinder moved horizontally and vertically across all grid points. A Gaussian function was used to approximate a continuous mapping between hand locations and ΔC.

$$f(x) = a \cdot \exp\left(-\left(\frac{(x-b)^2}{2c^2} + \frac{(y-d)^2}{2e^2}\right)\right) \quad (2.4)$$

where *a* was the measurement value from the sensor, *b* and *d* were the location of sensors in the map, and c and e were the coefficients to be estimated.

ΔC from simulation is shown in Figure 15e as blue dots. The contour map was plotted using the fitted Gaussian equation and showed good agreements with numerical results. Figure 15d showed the real-time mapping using the fitted Gaussian function described. When a person pressed his right foot (with a leather shoe) on top. When the foot with a shoe was placed on a board, the pressurized area was changed red. Sequential footsteps showed distinct ΔC for each foot, and capacitance returned to baseline when both feet left, with the rear foot responding faster. The around 400 fF ΔC came from the low dielectric constant shoe rubber.

Finally, Figure 15e showed ΔC for glass and metal cups during an addition of 300 mL water at a 100 mL increment. Contour peak highlighted the cup location and ΔC. Since pressure sensing is desired, a 1 mm thick PDMS plate was place between cups and the sensor to help with uniform pressure distribution. The ΔC over time graph showed the effect of both cup and added water. Average ΔC values were 341, 415, and 442 fF for 100, 200, and 300 mL of added water in a glass cup. Such values became 670, 688, and 709 fF for a metal cup. The average ΔC value for a metal cup for 100 mL was 19.5 fF. When 100 mL of water was converted to a pressure in a 70 mm-diameter metal cup, the pressure applied to a sensor was 254 Pa. Considering the amplitude of noise level (± 5 fF), the pressure detection limit was determined to 64 Pa.

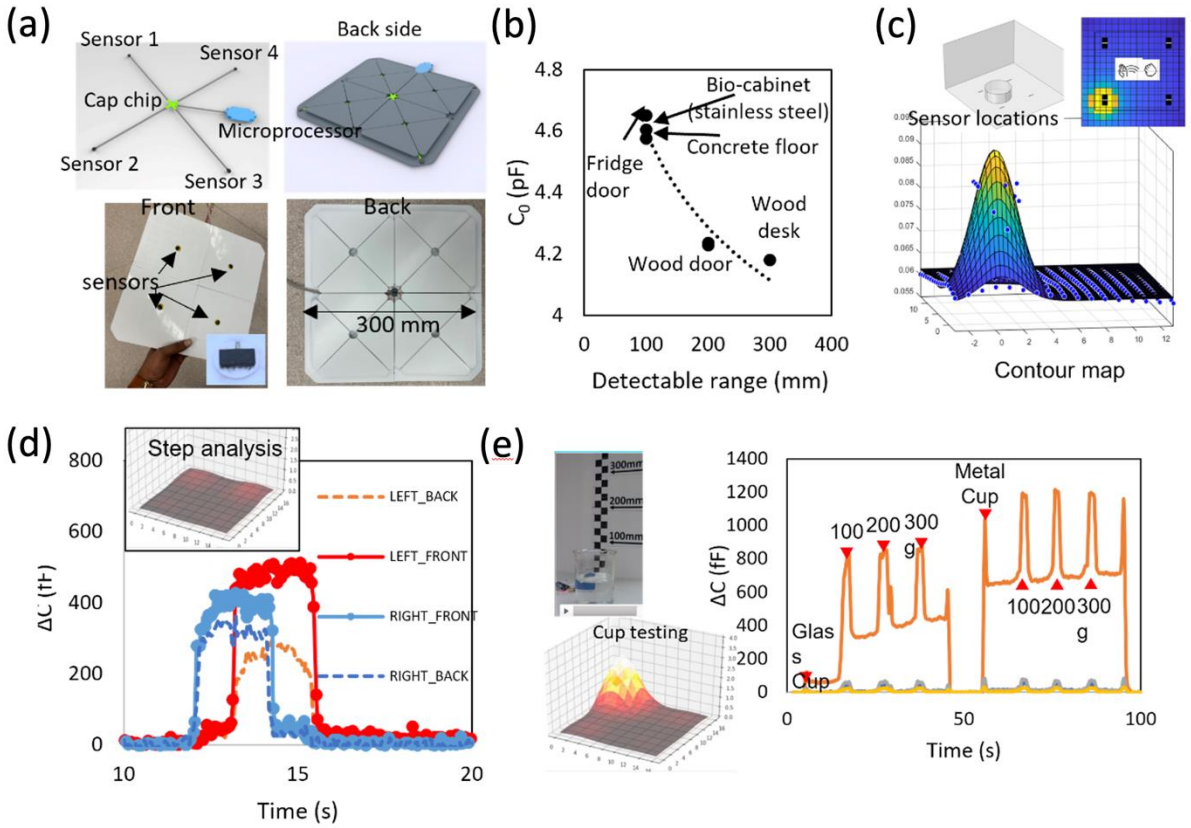

Figure 15. (a) 3D-design and photos of a smart pad. Four sensors are radially arranged on a 3D-printed plate. 10 mm-wide SF sensors are used. (b) Relationship between C0 and a detectable range of a human hand. (c) Numerical model of a smart pad integrated with four sensors. The contour map shows ΔC based on the location of an object. (d) Step test for a smart pad. Stepping of right and left feet followed by leaving both feet. Contour map showing only with a right foot. (e) Water supply to glass and metal cups (100 mL increment)

Gesture recognition was attempted with the help of my research collaborator, Dr. Zhongjie Qian. We trained a Long Short-Term Memory (LSTM) model using the *Sktime* ML package, with

a sampling window of 3s. Four types of gestures: left-right swiping, hand grabbing, writing letter A and B were performed above the pad for 30 times each. Figure 16a-b showed distinct capacitance changes for each type of gesture input.

Figure 16c showed the real-time gesture recognition for the left-right, right-left, writing 'A', and writing 'B' gesture. Examples of capacitive input which were classified as "Gesture left" and "Gesture Right" were shown in Figure 16d.

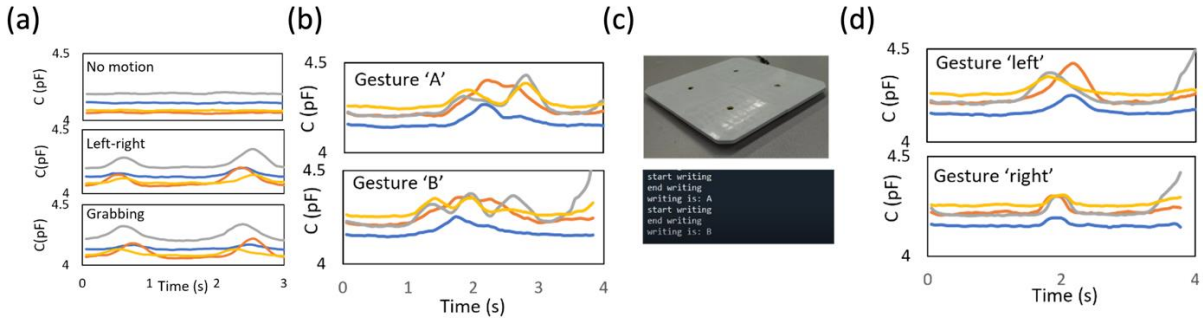

Figure 16. (a) Capacitance C during without motion, left-right swiping, and grabbing of a hand on a pad. (b) Capacitance C during writing letter A, B. (c) Recognition result of letter "A", and "B" in testing runs. (d) Capacitance inputs for actions classified as left swipe and right swipe.

2.8 CONCLUSION

In conclusion, this chapter presented an ultrasensitive capacitive sensor made of nanostructured fibrous CPC electrodes. The unique fibrous properties of CPC allowed the formation of numerous high-aspect-ratio conductive fibers, which, when combined with it auxetic behavior, created a capacitive sensor of superior proximity and pressure sensitivity.

Finite element analysis provided insights on how various sensor electrode configurations interact with the hand during proximity sensing. The result showed capacitive sensitivity could be increased by decreasing the baseline capacitance using a smaller electrode, or by increasing the with-target capacitance using a fibrous electrode. Among 5 sensor configurations, the 10 mm wide single fibrous sensor got a remarkable 300 mm hand proximity detection range, which is one of the largest. Tests also showed that, in spite of the shape irregularities, the initial capacitance value had variation of less than 0.4%.

Besides hand proximity, the ultrasensitive CPC sensor also showed its performance in water measurement, indicating capabilities in sensing charge variations and pressure changes as low as 64 Pa. The combination of high pressure and proximity sensitivity and small, flexible packaging allows CPC capacitive sensor to shine in HMI applications such as hand proximity measurement. A smart pad composed of four capacitive sensors was constructed to recognize human behavior using a machine learning algorithm in real time. The ultrasensitive capacitive sensor facilitates the delicate detection of human behavior, environmental change, manufacturing processes, and safety control. its high sensitivity opens further possibilities in eye tracking, which I will demonstrate in the next two chapters.

Chapter 3. Capacitive Eye-Tracker for Primate Gaze Tracking

3.1 OBJECTIVES

In the previous chapter, I introduced a CPC-based capacitive sensor that had enhanced sensitivity compared to its physical size. Characterization results showed that the CPC sensors work best with used in single sensor format (SF) and have the largest advantage over a metal sensor at shorter distances (<= 40 mm). Demonstrated applications included hand proximity – pressure sensing, and water level sensing.

This chapter introduced an innovative usage of the CPC capacitive sensor for gaze measurement in two male rhesus macaques (Macaca mulatta). The main focus of this chapter was designing and testing capacitive eye trackers and benchmarking against the "Gold Standard" scleral search coil in gaze tracking, introducing data processing and statistical analysis methods that will be revisited in later human eye tracking tasks, and exploring machine learning methods for gaze estimation.

Overall, this chapter served as an introduction to the capacitive eye eye-tracking, as well as a preview of the later, more complex human eye-tracker for wearable eye tracking and mental fatigue tracking applications.

3.2 INTRODUCTION

Research in the oculomotor system explores the link between eye movement and brain activity [54-56]. Technology advancements have enabled precise measurement of eye movements, aiding studies on the neural basis of eye control and learning [57-60]. These studies provide insights into cognitive functions like decision-making [61] and attention [62]. Moreover, abnormal eye movements are associated with a range of neurological disorders, including Creutzfeldt-Jakob disease [63], autism [64], Parkinson's disease [65, 66], and Huntington's disease [67], underscoring the importance of accurate eye movement measurement for both understanding the oculomotor system and diagnosing related neurological conditions.

Eye tracking technology can be categorized into four main types: electro-oculography (EOG), photo- or video-oculography (VOG), combined pupil and corneal reflection (PCR, Purkinje images) [68], and the scleral search coil method. EOG measures the difference in corneo-retinal standing potentials by attaching electrodes to the skin near the eyes [69]. To measure horizontal eye movements, for instance, electrodes are placed on the skin at the left and right temples. As the eye rotates, the potential difference between the two electrodes changes proportionally with the rotation angle. Although EOG is a cost-effective and straightforward method, it necessitates skin contact that can lead to discomfort. Besides, its signals may be susceptible to mixing with other biopotentials, like muscle potentials.

VOG systems measure eye positions by capturing the iris's relative location using cameras, avoiding direct skin contact. However, its accuracy is significantly influenced by ambient lighting. Low light conditions can diminish image contrast, affecting iris detection. Conversely, excessive brightness, non-uniform, or fluctuating lighting conditions can introduce noise to the images, reducing the detection accuracy.

In contrast to VOG, PCR systems project light patterns into the eye and measure the locations of reflections from the cornea and lens surfaces [70]. The use of controlled lighting enables PCR systems to operate in dark environments and withstand ambient lighting changes, allowing high eye-tracking accuracy. However, bulky PCR systems tend to consume more power. The need for focused optics near the eye limits head movement and dynamic ranges.

The scleral search coil method utilizes electromagnetic induction to detect eyeball movements. In this system, a coil of a few turns of thin insulated wire is surgically implanted on the surface of the eyeball under the conjunctiva. The two wire ends are twisted together, passed subcutaneously, and soldered to a connector at the top of the skull. When the coil rotates in the electromagnetic field, a voltage proportional to the angle of the eye's rotation is produced. Therefore, this system allows for eye movement measurement with the eyelid closed, e.g., a blink [71]. The scleral search coil's high accuracy (<0.1°) [72] and bandwidth [73], low latency, and superior rejection of environment interference make it the gold standard for eye tracking in oculomotor research [74-76]. This system's real-time capabilities enable complex closed-loop optogenetic manipulation of neural activity precisely during a saccade [77-79]. The scleral search coil is bulky, power-demanding, invasive, and no longer commercially available.

Capacitive transducers play a significant role in human-device interactions. Among these, the proximity capacitive sensor stands out, finding wide use across human activities [80, 81]. It is applied for gesture sensing [82] and human-presence monitoring in automotive fields. This same principle can track eyeball movement using proximity sensing, leveraging the eye's asymmetry near the scleral-corneal junction [83]. Eye rotation alters the sensor-eye distance, changing the fringing electric field and, thus, the capacitance.

This study presents a novel approach using a carbon nanotube-paper composite (CPC) for a capacitive eye tracker, facilitating the development of a non-invasive eye movement monitoring technique for non-human primates. The technique operates on the principle of proximity capacitive sensors, detecting femtofarad (fF) capacitance changes during horizontal and vertical eye rotations. The performance of the CPC capacitive eye tracker is evaluated on different eye movements against the reference scleral search coil system. Various data processing techniques and machine learning models are explored to enhance the accuracy of gaze tracking. The outcomes demonstrate the capacitive eye tracker's potential for research and medical applications, paving the way for non-invasive, accurate eye tracking.

3.3 Materials and Methods

3.3.1 Compliance & Research Approval

All experiments were performed in accordance with the Guide for the Care and Use of Laboratory Animals and exceeded the minimum requirements recommended by the Institute of Laboratory Animal Resources and the Association for Assessment and Accreditation of Laboratory Animal Care International. All the procedures were evaluated and approved by the local Animal Care and Use Committee of the University of Washington.

3.3.2 Fabrication of fibrous electrodes

The capacitive sensor, made from carbon nanotube-paper composites (CPC) following methods outlined in [38, 39], had an average thickness of 88.4 ± 3.1 μm. The sensor fabrication

process (Figure 17a) involved patterning silver polymer (MG Chemicals, 8330S-21G, USA) strips at both ends of a rectangular CPC piece, then using a 0.1 mm capillary pen to print a water line at the center of the material. This line weakened the CPC fibers, allowing a tension-induced fracture to split the material. This wet-stretching process resulted in a 5x10 mm^2 fibrous electrode. The sensor was laminated with a 50 μm-thick self-adhesive polyethylene terephthalate (PET) film. A wire lead was secured at the non-fracture end with silver epoxy (Figure 17b, top picture). The scanning electron microscope (SEM) image revealed conductive cellulose fibers at the cracking site (Figure 17b, bottom image).

In the last Chapter I found that compared to metallic sensors of identical dimensions, CPC sensors demonstrated enhanced sensitivity and dynamic range of capacitive detection. This improvement was attributed to the CPC sensors increased electric field and larger surface area due to their fibrous construction. Scanning electron- and optical microscopy showed that the fibers had a linear density of approximately 14.5 ± 3.6 mm^{-1}, lengths averaging 1.71 ± 0.4 mm, and thicknesses around 5.9 ± 1.6 μm. Despite the variable fiber dimensions, the large number of fibers balanced these differences, resulting in a minimal baseline capacitance variance of 0.4%.

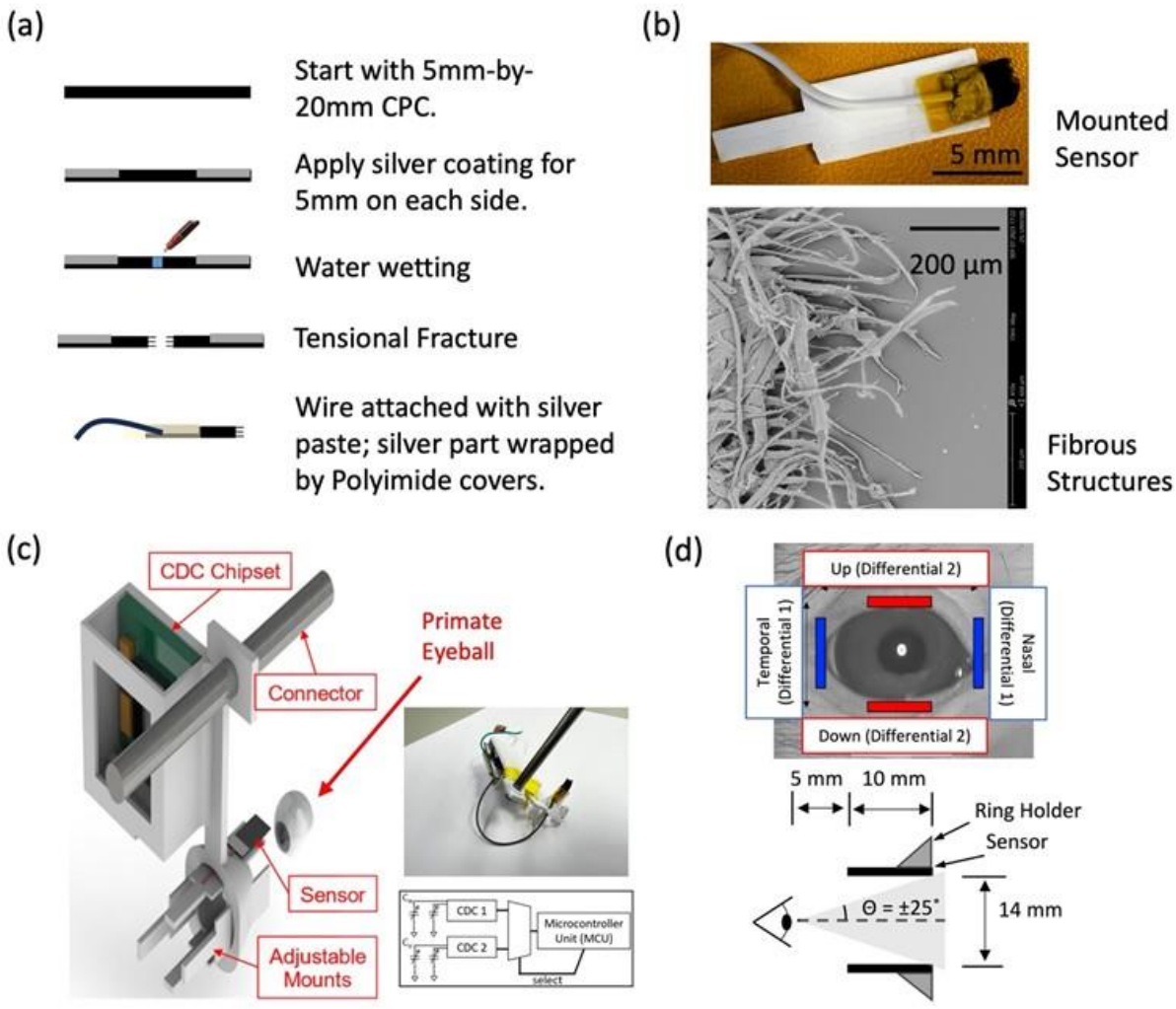

Figure 17. a) Steps of CPC sensor fabrication process. b) Mounted finished CPC capacitive sensor (top) and microstructures of the sensor at the tip (bottom). c) Design (left), circuit configuration (bottom right), and a photograph of the primate eye tracker fixture (top right). d) Top: Positions of differential capacitive sensors for detecting vertical and horizontal movement around the animal's right eyeball. Bottom: Animal field of view diagram estimated from the geometry of the ring holder.

3.3.3 Sensor Fixtures and electronics

The primate eye tracker fixture was custom-made using the specific cranial and facial dimensions of the primates in this study (Figure 17c). It featured a metal rod at the top, secured into a tube mount on the animal's head. Below the rod, a ring-shaped sensor holder was precisely aligned in front of the animal's right eye. Four adjustable rectangular sensor mounts were connected to the holder to secure CPC sensors. These sensor mounts were adjusted to position CPC sensors' front edges approximately 5 mm from the primate's eye. The sensors were placed such that horizontal and vertical pairs were equidistant from the center of the primate's right eye, and the animal had an unobstructed field of view of approximately ±25˚ (Figure 17d).

The capacitive sensors detected and processed eye movements by onboard capacitance-to-digital converters (CDCs). Active shielding and minimal cable length between the sensors and CDCs were implemented to reduce noise and parasitic capacitance. A single circuit board in the compartment adjacent to the rod contained two AD7747 CDCs (Analog Devices, MA, USA). Each CDC was configured for differential capacitance measurement: CDC 1 for a pair of sensors measuring horizontal movements and CDC 2 for a pair measuring vertical movements.

The AD7747, operating on the switch-capacitor principle, initially applied an excitation voltage (V_{ext}) to the sensor, accumulating charges proportional to the sensor capacitance (Q_{sensor}). After achieving charge stability, the sensor disconnected from the voltage source and connected to an internal reference capacitor (C_{ref}) with a known capacitance. This switching caused a charge transfer from the sensor to the reference capacitor, developing a voltage (V_{ref}) across C_{ref}. The sensor's capacitance was inferred from V_{ref}, as the transferred charge (Q_{sensor}) followed this equation: $Q_{sensor} = C_{ref}V_{ref}$.

The circuit board also included an nRF52840 microcontroller (Nordic Semiconductor, Trondheim, Norway), handling CDC data via I^2C interface. It processed the data and relayed capacitance values to a laptop. The CDC was capable of a maximum sampling rate of 45 Hz. To avoid signal interference with the same excitation frequencies of two CDCs, however, the CDCs operated in an alternating sampling mode, effectively reducing the overall sampling rate to 21 Hz. Figure 17c provides an electrical block diagram illustrating the microcontroller's selecting method for alternating between the two CDCs. The whole system consumed less than 10 mW during operation.

3.3.4 Scleral search coil

We used two male rhesus macaques (*Macaca mulatta*) in this study, a common sample size for study involving scleral search coil [84-87]. The technique to implant the scleral search coil has been previously reported [88]. Briefly, a preformed 3-turn scleral eye coil (18-19 mm diameter), made of fluorinated ethylene propylene insulated stranded stainless-steel wire (0.0012” diameter, Alan Baird Industries), was placed surgically on the left eye of the animals under the conjunctiva. The eye coil was secured by tying it to the lateral and medial rectus muscle insertions using an absorbable suture. The two wire ends were twisted together and then passed through a small hole drilled on the sphenoid bone, routed subcutaneously to the top of the skull, and soldered to a connector implanted on the frontal bone, secured with dental acrylic and titanium screws. In addition, we also implanted dental-acrylic head stabilization lugs.

Following the surgery, the animals were trained for smooth pursuit and saccade tracking with a red laser dot used as the gaze target. The laser was rear-projected onto the ground-glass side

of a tangent screen via mirrors attached to galvanometers. The animals were rewarded with a dollop of fortified applesauce every second, provided they accurately tracked the target and maintained their gaze within a 1.5° window surrounding the target.

The animal sat in a neurophysiological booth with its head fixed, and its eye coil was placed in the center of two orthogonal AC magnetic fields with frequencies of 114 and 73 kHz for the horizontal and vertical fields, respectively. The amplified eye coil signal was then fed to a phase detector (CNC Engineering, Seattle, USA) that generated voltages proportional to the horizontal and vertical gaze angles. The recorded analog signals of horizontal and vertical eye and target positions were digitized at 1 kHz and visualized through a custom program showing target locations, eye positions, and velocities.

In this study, we opted to compare the capacitive eye tracker with the scleral search coil, known for its resolution of better than 0.1° [74]. While Chung's lab owns a pupil and corneal reflection (PCR) eye tracker (Tobii Pro Nano, Stockholm, Sweden) designed for human use, it was deemed unsuitable for this study. First, few PCR trackers are compatible with non-human primates such as rhesus macaques due to their smaller eyes and faster movements. The Tobii Pro Nano is not one of the capable models. Second, the layout of the small neurophysiological booth where we conducted experiments posed additional challenges in properly positioning the PCR tracker. Therefore, we chose the scleral search coil as the ground truth gaze signal.

3.3.5 Experimental Setup

Two macaques (animals #1 and #2, abbreviated to A1 and A2 in later texts) were used in this experiment. The animal was secured in an acrylic chair with bars to stabilize its head [89, 90].

We then placed and secured the capacitive eye tracker (Figure 17c) in front of the right eye. Their eye movement was simultaneously recorded using both the custom capacitive eye tracker (right eye) and the reference scleral search coil system (left eye). During each experiment, the animal was placed in a fully darkened booth, facing a tangent screen 62 cm from its eyes (Figure 18a). The animal had been trained to track a moving red laser dot target (~0.25° diameter). They were presented with either sinusoidal movements or discrete steps of the target. The movement of the red laser dot was controlled by a computer using Power 1401 (Cambridge Electronic Design, Cambridge, UK), which also collected the outputs from the scleral search coil system. Outputs from our custom capacitive eye tracker were collected by another computer. The data from the coil and capacitive eye tracker were synchronized during post-processing.

The experiments produced three distinct data sets (data sets 1 – 3, later abbreviated as DS1 – DS3), with DS1 being the most recent and detailed. Animal A1 contributed to DS1 and DS2, while DS3 originated from A2. These data sets were collected over a span of 3 years, with the eye tracker being installed and removed for each testing session.

DS1 contained five kinds of different eye movements: (1) horizontal smooth pursuit, (2) horizontal saccade tracking, (3) horizontal fixation, (4) vertical smooth pursuit, and (5) vertical saccades tracking. Smooth pursuit, saccades, and fixations were common eye movements with different characteristics (Figure 18b). Smooth pursuit involves tracking an object smoothly and continuously, while a saccade is a response to the sudden appearance of a target in a new location. Fixation tasks, on the other hand, require the animal to keep its gaze on a stationary target. In DS1 experiments, the range of eye movement was limited to ±5° amplitude, except for the fixation test where the range was ±15°. The starting position of the laser spot was configured to have an offset of up to 5° from the center of the visual field. Positive angle denoted rightward or upward gaze

positions (see Figure 17d). During horizontal and vertical smooth pursuits, the red laser spot followed a sinusoidal trajectory with a default period of 10 seconds (T = 10 s). Additional smooth pursuit tests were also conducted at shorter periods of 5 [vertical smooth (T = 5 s)] and 2 seconds [horizontal smooth (T = 2 s)] to determine the operational limit of the eye tracker. During saccade tracking, the target stepped every 2 seconds, starting at the center (0°), moving to +5° (right), returning to the center, then to -5° (left), and back to the center. The horizontal fixation was similar to saccade, where the target stepped 5˚ every 10 seconds to right, back to center, and repeat on the left side.

DS2 (from animal A1) and DS3 (from animal A2) involved the animals performing both saccades and smooth pursuit movements within a ±10° amplitude range. However, the smooth pursuit tasks varied across three distinct periods (see Table 6). Horizontal fixation and vertical saccade tests were not conducted in these sets. DS1, being the most comprehensive, was selected for sensor characterization and analysis. DS2 and DS3 were utilized in the machine learning section due to their differing characteristics.

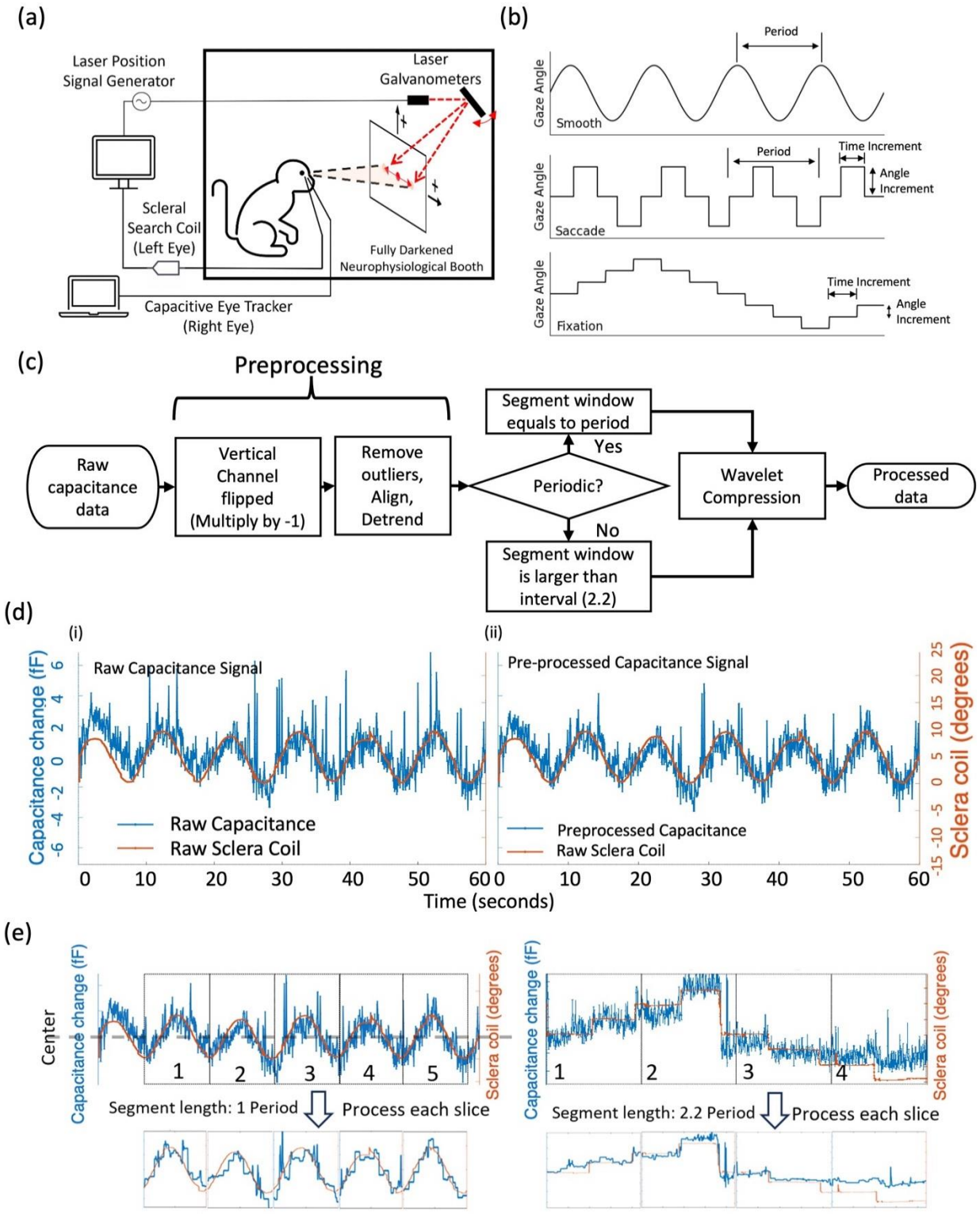

Figure 18. Experimental and data processing procedure. a) Experimental setup showing a control computer manipulating a galvanometer mirror reflector to move a laser dot on a screen to guide

the animal's gaze. The same computer also recorded the outputs of the scleral search coil (left eye) while another one simultaneously recorded the outputs of the custom capacitive eye tracker (right eye). b) Tasks of three different modalities and their control parameters. The illustration compresses the fixation durations to fit the entire sequence; however, the actual time increment in fixation is much longer than the inter-saccadic intervals. c) Flowchart showing the data processing pipeline. d.i) Raw capacitance data overlaps with scleral coil data. d. ii) Result of signal preprocessing that involves outlier removal, signal alignment, and linear detrend. e) Result of data processing flow shown 2c. The upper left panel shows the raw capacitance signal of smooth pursuit, and the lower left panel shows the processed capacitance signal. The upper right panel shows the raw horizontal fixation test, and the lower right shows the processed capacitance signal. In both 2d and 2e, the capacitance values are in blue alongside the scleral search coil gaze position in red.

Table 5. Test cases in DS1 for animal A1

Test case (DS1)	**Angles (Positive right/up)**	**Angle (Increment)**	**Period (seconds)**	**Segment duration (seconds)**
Horizontal Fixation	[-15,15]	5˚ every 10 seconds	Non-periodic	22
Horizontal Smooth (T = 10 s)	[0, 10]	Continuous	10	10
Horizontal Saccade	[0, 10]	5˚ every 2 seconds	8	8
Vertical Smooth (T = 10 s)	[0, 10]	Continuous	10	10
Vertical Saccade	[-5, 5]	5 every 2 seconds	8	8
Horizontal Smooth (T = 2 s)	[0, 10]	Continuous	2	2
Vertical Smooth (T = 5 s)	[-5, 5]	Continuous	5	5

Table 6. Experiments from DS2 and DS3, and the corresponding animals.

Test Name (Data sets 2 and 3)	**Angles**	**Angle (Increment)**	**Period (seconds)**	**Segment duration (seconds)**	**Animal**
Horizontal Smooth (DS2)	[-10, 10]	Continuous	10 seconds	10 seconds	A1
Vertical Smooth (DS2)	[-10,10]	Continuous	10 seconds	10 seconds	A1
Horizontal Smooth (DS3)	[-10, 10]	Continuous	3.3 seconds	3.3 seconds	A2
Horizontal Saccade (DS3)	[-10,10]	5˚ every 1.75 seconds	7 seconds	7 seconds	A2

3.3.6 Data Processing

The raw data, comprising time-series recordings of capacitance changes, frequently contained anomalies unrelated to eye movements, such as accidental sensor contact with facial hair or eyelashes, muscle twitching, or eye closures. To prepare the data for analysis and minimize artifacts, we developed a data processing flow (Figure 18c). The process involved several preprocessing steps, including the outlier removal, alignment, and detrending. It was followed by segmentation and wavelet compression to refine the signal for subsequent analysis.

Every data entry contained three values: a timestamp, the capacitance value by the horizontal sensor, and that by the vertical sensor. Notably, the vertical sensor's capacitance decreased when the animal looked upwards. To align this with the standard sign convention used in scleral search coil systems, we inverted the values by multiplying them by -1.

After that, we applied the Hampel filter to detect outliers. This filter identified outliers if the absolute difference between a value and the median of its surrounding values exceeded k times the median absolute deviation (MAD) within a moving window. The representation of the Hampel filter and MAD calculation is given by:

$$Outlier\ if\ |x_i - \tilde{x}| > k * \text{MAD} \tag{3.1}$$

$$\text{MAD} = median(|x_i - \tilde{x}|) \tag{3.2}$$

where in this test, after experimenting with parameters, we chose a threshold of k = 3 and a window size of 10 samples to balance artifact detection and signal feature retention. Window size could be shorter for testing with shorter period for preserving more details. Detected outliers were replaced by the preceding non-outlier value.

Following outlier correction, we aligned readings from the capacitive eye tracker and the scleral search coil to correct any timing discrepancies arising from separate control systems. Alignment was achieved by identifying and matching common patterns in both signals, such as a series of gaze jitters. Following alignments, we performed linear detrending to mitigate any temporal signal drift. Linear detrending involved fitting a linear trendline, expressed as $y = kt + b$, to the capacitance value y over time t. The detrending process then removed this linear trend, resulting in detrended value denoted as $y' = y - (kt + b)$. The results of all preprocessing steps are shown in Figure 18d.

In tests other than fixation, where the repeated patterns of eye movements occurred, the detrended signals were segmented according to their period without overlap or padding. Each

segment represented a complete gaze movement from start to finish, allowing for detailed examination at a finer timescale and statistical analysis on individual repeat. For periodic signals, data were segmented according to their periods (see Figure 18e) with no overlapping or padding between segments. Despite being non-periodic, fixation data were also segmented to include at least two gaze angles per segment. The fixation-signal segment length was arbitrarily set at 2.2 times the step interval.

Discrete wavelet transformation with a *Biorthogonal 1.5* mother wavelet [91] was applied to the data segments. We chose this method after exploring different signal processing methods such as moving-median filtering, bandpass filtering, and discrete wavelet transformation with *Daubechies 4* wavelet [92]. The results of these methods were compared in the result section. Up to level 4 of wavelet compression of these segments was then carried out using the MATLAB's *wdencmp* function using default parameters calculated from *ddencmp* function. For data with shorter periods, the level was lowered to preserve more details.

3.3.7 Statistical analysis and machine learning

For each case study, a continuous recording of 60 seconds was reassembled from processed segments (illustrated in Figure 18e, bottom panels). Smooth pursuit and saccade tracking tests typically lasted about 120 seconds, while fixation tests were about 90 seconds in duration. The 60-second recording duration was identified as the optimal continuous recording duration, being the longest span during which both animals consistently and accurately tracked the visual stimuli. Sensitivity, expressed in femtofarads per degree (fF/°), was calculated using bi-square-weighted least-squares linear fitting on all tests. Unlike standard linear regression, this method minimized

the impact of any remaining outliers. For linear correlation, we calculated the Pearson correlation coefficient (PCC), defined as:

$$r = \frac{\sum(x_i - \bar{x})(y_i - \bar{y})}{\sqrt{\sum(x_i - \bar{x})^2 \sum(y_i - \bar{y})^2}} \tag{3.3}$$

In this equation, r is the PCC value; y_i and $\bar{y}$ are the observed capacitance and mean capacitance of the segment; x_i and $\bar{x}$ are the individual gaze angle and mean gaze angle of the segment measured by the scleral search coil. The difference in sampling rate between our capacitive eye tracker and the referential scleral search coil system resulted in timing mismatches within each segment. To align these two measurements for PCC calculation, we down-sampled the scleral search coil measurement by applying table-lookup interpolation. This method involved identifying the two scleral search coil measurements that were temporally nearest to each capacitive eye tracker measurement. Linear interpolation was then performed between these two measurements to estimate a coil value corresponding to the time of the capacitive measurement. We evaluated the maximum, average, and standard deviation of PCC across all segments.

Using MATLAB's machine learning toolbox, I developed models to predict gaze angles from capacitance values. We assessed their absolute errors as the angle difference between the predicted and actual gaze obtained from a scleral search coil. The tested models included linear regression, decision tree, Gaussian kernel support-vector regression, and artificial neural networks. For reproducibility, we fixed the random number generator (RNG) seed to 10. All models were trained on shuffled data without timestamps, with an 80/20 split between training and testing sets.

To mitigate overfitting, we employed 5-fold cross-validation for all training processes. The test loss was evaluated with the median absolute error (MAE) metric, given as

$$\text{MAE} = median(|y_i - \hat{y}_i|) \tag{3.4}$$

where y_i is the gaze angle value from the scleral search coil and $\hat{y}_i$ is the predicted value. We evaluated the robustness of the models by testing them on both animals.

Given the low dimensionality of the eye tracking data, with only two values representing capacitance changes in horizontal and vertical directions, all models could be trained quickly. This enabled us to train multiple models on the same data and compare their MAEs. Their hyperparameters are shown Table 7.

Table 7. Hyperparameters of all four models.

Regression Model	Hyperparameters
Tree	Minimum leaf size: 4 surrogate split: none.
Linear	Linear
Support Vector Regression	Kernel: Gaussian kernel scaling: 0.25 half width of Ɛ-insensitive band: Interquartile range of response (gaze angle) divided by 13.49
Neural Network	1 input node, 1 output node, $\lambda = 0$ 2 fully connected layer with 25 nodes each, ReLU activation function, 1000 epochs.

3.4 RESULTS

3.4.1 Comparison of Data Processing

After we obtained preprocessed signals (Figure 19a) from the raw capacitance signals, we compared four signal processing techniques to identify the one that most effectively reduced noise in the capacitance signal while still preserving rapid events. We evaluated the moving median filter (Figure 19b) and the low-pass filter (Figure 19c). Both filters produced signals that were smoother

and matched better to measurements of the scleral search coil system. Although these filters improved the signal, we noted their distortion of brief and transient events, such as saccades. This effect was evident in Figure 19b, where the moving median filter introduced a delay in saccadic movement, creating a noticeable slope. In contrast, the wavelet-based method allowed for a better representation of sharp edges with better time-domain resolution. Between the Biorthogonal 1.5 mother wavelet (Figure 19d) and Daubechies 4 mother wavelet (Figure 19e), we chose the Biorthogonal 1.5 mother wavelet to filter the signal. The Biorthogonal 1.5 mother wavelet, having a staircase shape and five vanishing moments in its reconstruction function, was ideal for representing complex, multi-frequency features in smooth pursuit and saccade tracking. Consequently, we processed all data using wavelet compression with the Biorthogonal 1.5 mother wavelet for subsequent analysis.

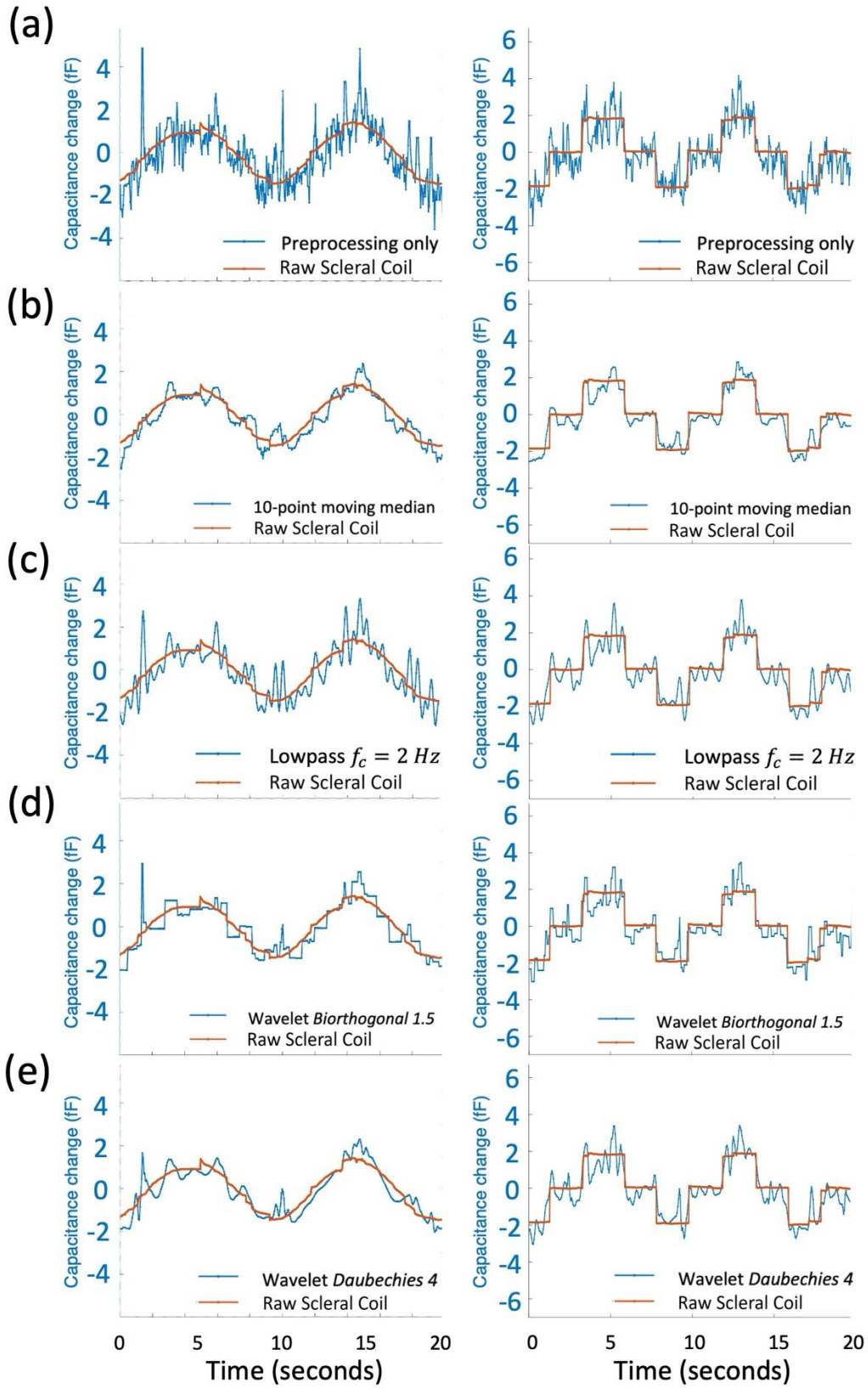
(a)
(b)
(c)
(d)
(e)
Capacitance change (fF)
Preprocessing only
Raw Scleral Coil
10-point moving median
Raw Scleral Coil
Lowpass $f_c = 2\ Hz$
Raw Scleral Coil
Wavelet *Biorthogonal 1.5*
Raw Scleral Coil
Wavelet *Daubechies 4*
Raw Scleral Coil
Time (seconds)

Figure 19. Comparison of signal processing methods on 20-second signals from horizontal smooth pursuit (left) and horizontal saccade tracking (right). The processed capacitance signal is blue, and the referential scleral search coil signal is red. a) Preprocessed signals before signal processing shown in (b-e). b) Processed with 10-point moving median filter. c) Processed with 2 Hz cutoff lowpass filter. d) Processed with Biorthogonal 1.5 mother wavelet. e) Processed with Daubechies 4 mother wavelet.

3.4.2 Segment-based Analysis

This section aimed to evaluate the capacitive eye tracker's effectiveness in eye tracking by evaluating its Pearson correlation coefficient (PCC) relative to the reference data from the scleral search coil system. Additionally, we also determined the sensitivity of the eye tracker to changes in gaze angle (fF/°). The analysis was conducted on the data from DS1, illustrated in Figure 20, and on DS2 to DS3, shown in Figure 21.

Figure 20a shows the 2 segments of horizontal smooth at T = 10 s. Using bi-square-weighted linear regression, we found the sensitivity was about 0.32 femtofarad-per-degree (fF/˚). Across all segments, the maximum PCC values were 0.94, with an average of 0.88 ± 0.05 (mean ± 1SD). When the gaze velocity increased by five-fold [horizontal smooth (T = 2 s), shown in Figure 20b], the sensitivity dropped from 0.32 to about 0.18 fF/˚. The maximum PCC slightly decreased to 0.92, while the average significantly dropped to 0.56 ± 0.24, suggesting highly variable performance during fast pursuits. Vertical smooth pursuits, shown in Figure 20c-d, maintained a consistent sensitivity of 0.17 fF/˚ and maximum PCC of 0.9 at both T = 10 s and T =

5 s. However, the pursuit over a shorter period (T = 5 s) exhibited a higher standard deviation of 0.16, compared to 0.07 for the T = 10 s pursuit.

Figure 20e-h show the results for saccade tracking and fixation. Horizontal saccade (Figure 20e) had a sensitivity of 0.36 fF/˚ with maximum and average PCC of 0.95 and 0.88 ± 0.04, respectively. Vertical saccade showed a sensitivity of 0.18 fF/˚ with maximum and average PCC values of 0.88 and 0.79±0.12, respectively. Horizontal fixation was categorized into rightward (Figure 20g) and leftward (Figure 20h) gaze. As seen in the Figure 20h, the capacitance measurement saturated at gaze angle exceeding 5˚ to the left. Excluding the saturated sections, the sensitivity was about 0.35 fF/˚ with PCC maximum value of 0.92, and an average of 0.86 ± 0.06. Sensitivity and PCC of horizontal fixation closely matched those of horizontal saccade.

The fixation stability of the sensor without eye movement was analyzed by measuring the median absolute deviation (MAD) from median capacitance at 5°, 10°, and 15° gaze angles. For the non-saturated range, the MAD were 0.34 fF, 0.36 fF, and 0.43 fF for fixations at 5°,10°, and 15° angles, respectively. With sensitivity about 0.35 fF/°, the median angular error reached 1.23°. However, considering spontaneous animal eye movements even when the laser target spot was stationary, this error might be overestimated. Real stability will be further discussed through gaze prediction accuracy in the machine learning section.

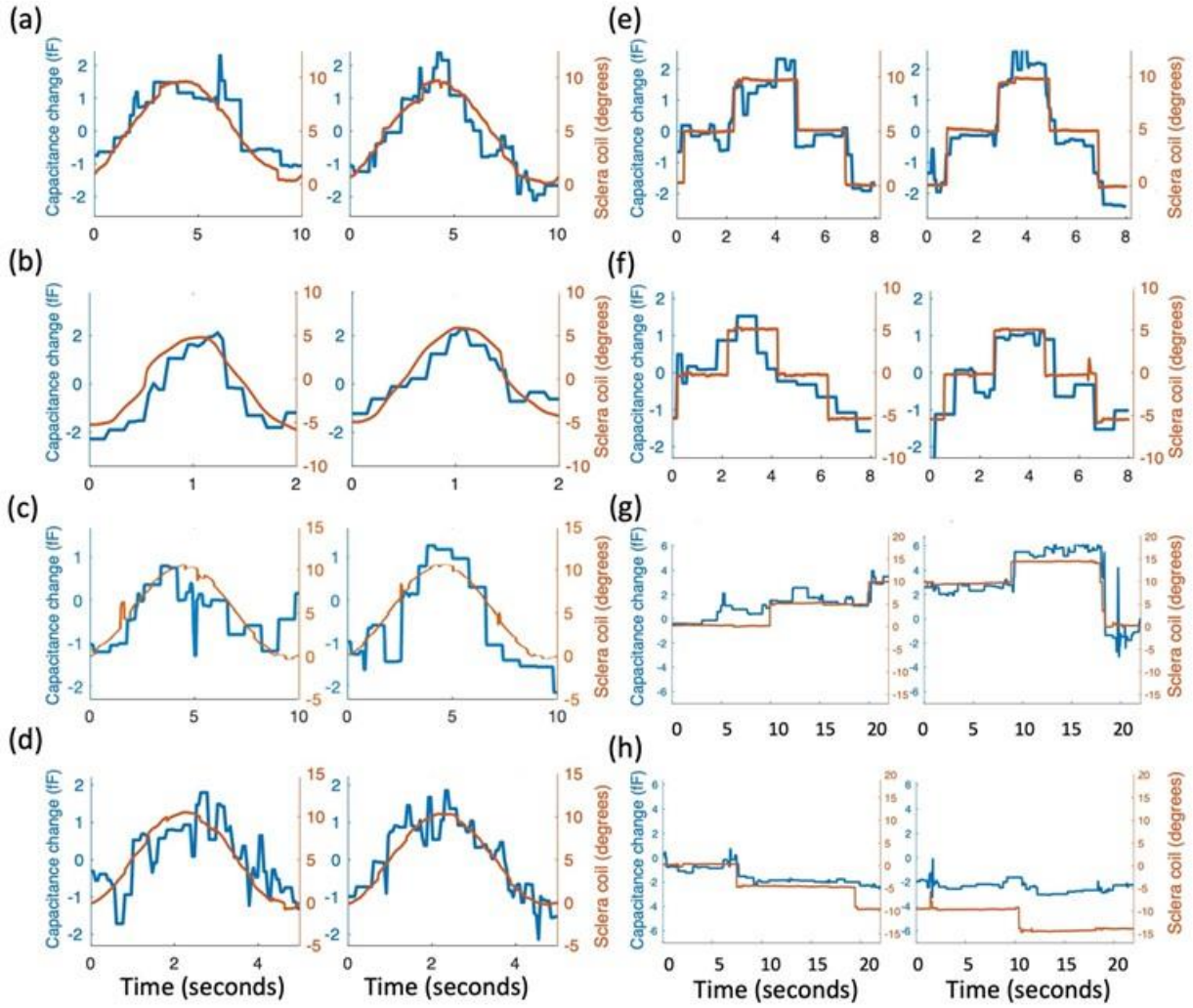

Figure 20. Data set 1 only (DS1): Processed capacitance change versus true gaze angle from referential scleral search coil. For all panels, the processed capacitance is shown in blue with a unit of femtofarads (fF). Scleral search coil gaze angle is shown in red of degrees (˚). The horizontal axis represents time in seconds. a) horizontal smooth at a period T = 10 s. b) horizontal smooth 1 (T = 2 s). c) vertical smooth (T = 10 s). d) vertical smooth (T = 5 s). e) horizontal saccade 1 (T = 8 s). f) vertical saccade (T = 8 s). g) Horizontal fixation (segment when gazing to right); h) Horizontal fixation (segment when gazing to left).

Further analysis was conducted on DS2 and DS3, which had different experimental setups compared to DS1 (see Table 6)

The smooth pursuit test in DS2 covered twice the angle for the same period as that in DS1, effectively doubling the peak gaze velocity. The horizontal smooth in DS2 (Figure 21a) showed a sensitivity around 0.13 fF/°, with a peak and average PCC of 0.92, and 0.83±0.05, respectively. The vertical smooth (Figure 21b) had a higher sensitivity of 0.41 fF/°, achieving a maximum PCC of 0.91 and an average PCC of 0.80±0.08. In the vertical smooth pursuit test, it's notable that animal A1 struggled with tracking the visual stimulus effectively. This issue manifested in noisier capacitance signals and a staircase pattern in the scleral search coil signals. When compared to DS1, it was evident that different installation and calibration between sessions could contribute to difference in sensitivity. Despite the difference in installation and calibration, the results maintained a good agreement with the reference scleral search coil reading, indicating robustness.

DS3, collected from animal A2, had twice the smooth pursuit amplitude of DS1 with an even shorter period, resulting in a much higher gaze peak velocity. The horizontal smooth pursuit from this dataset had a peak gaze velocity 6 times of the horizontal smooth of DS1 at T = 10 s. As shown in Figure 21c, this horizontal smooth pursuit had a 0.18 fF/° sensitivity, with a maximum and average PCC value of 0.92 and 0.75±0.4, respectively. Horizontal saccade, shown in Figure 21d, exhibited a sensitivity of 0.19 fF/°, with the maximum and mean PCC values or 0.92 and 0.70±0.31. When compared with the slower horizontal smooth pursuit of DS1 (T = 10 s), the faster horizontal smooth pursuit of DS3 had a worse agreement with the scleral coil signal but performed comparably to the faster horizontal smooth of DS1 (T = 2 s). This suggested that accuracy of the current capacitive eye tracker was reduced at high gaze velocities, likely due to the limitations imposed by the hardware’s low sampling rate.

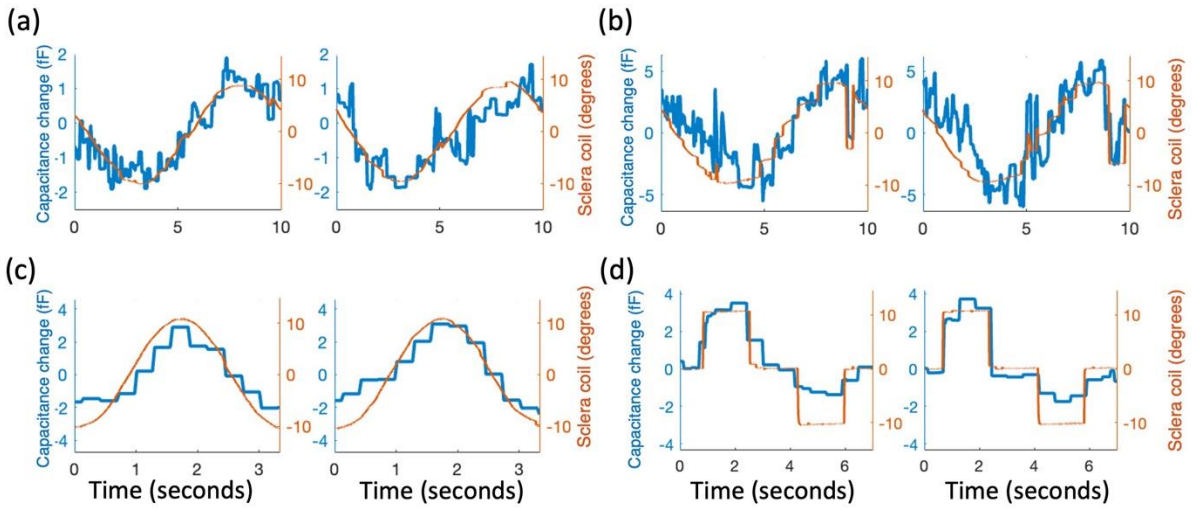

Figure 21. Comparison of capacitance changes to various smooth pursuit behaviors in DS2 and DS3. (a) Horizontal smooth pursuit at T = 10 s from DS2. (b) Vertical smooth pursuit at T = 10 s from DS2. (c) Horizontal smooth pursuit at T = 3.3 s from DS3. (d) Horizontal saccade at T = 7 s from DS3. Capacitance- and scleral eye coil signals are in blue and red, respectively.

3.4.3 Machine learning and Gaze Prediction

Machine learning algorithms were utilized to predict gaze angles. Given the novelty of a capacitive eye tracker and its signals, we did not have an existing method to compare it to other than the scleral search coil, which served as a control. Instead, we explored multiple machine-learning models to assess accuracy and the required computing resource. The Median Absolute Error (MAE) for various machine learning models applied were summarized in Table 8. Linear regression exhibited higher MAE across all tests, suggesting bad performance, likely due to its inability to handle the capacitive sensing non-linearity. In contrast, support-vector regression and neural networks showed better gaze predictions. Among them, the support-vector regression was

better in smooth pursuit, while the neural network was more effective in saccade tracking and fixation. The regression tree model outperformed all others, achieving a low MAE of 0.04° for horizontal fixation and 0.30° for horizontal smooth pursuit (T = 10 s). Note the MAE can be very low (less than 0.1˚) during saccades and fixations where gaze remained stationary most of the time. This low MAE highlighted the sensor's superior stability during stationary gaze.

Table 8. MAE of angle predictions using the capacitance data from dataset DS1 ~ DS3.

Test (DS1 unless noted)	**Averaged MAE of test sets**			
	regression tree	linear regression	support-vector regression	neural network
Horizontal Smooth (T = 10 s)	0.30	1.09	0.68	0.76
Horizontal Saccade	0.05	1.02	0.34	0.21
Horizontal Fixation	0.04	1.36	0.56	0.49
Horizontal Smooth (T = 2 s)	1.09	2.47	1.47	1.83
Vertical Smooth (T = 10 s)	0.49	1.72	0.94	1.22
Vertical Saccade	0.07	1.59	0.39	1.10
Vertical Smooth (T = 5 s)	0.95	2.20	1.41	1.65
Horizontal Smooth (DS2)	0.65	1.43	1.05	1.41
Vertical Smooth (DS2)	1.02	2.85	1.87	2.43
Horizontal Smooth (DS3)	1.08	2.07	1.86	1.72
Horizontal Saccade (DS3)	0.05	1.35	0.60	0.28

Considering the goal of developing a low power, portable eye-tracking device, it's important to consider the potential memory and power requirement. Both linear regression and regression tree can be quick to train, while the Gaussian kernel support-vector regression and the

neural network demands time and memory, which may be impractical. The regression tree could be the ideal choice from its quick training and its high accuracy.

Figure 22a shows a time series plot of the horizontal smooth pursuit in DS1 comparing the predicted gaze positions from the capacitive eye tracker (blue) to the actual positions measured by a scleral search coil method (red). The predicted gaze angle followed the reference gaze accurately for 60 seconds. Figure 22b shows the increase in capacitance with gaze angles. It exhibited gradual saturation at larger angles.

The accuracy of the machine learning models might be influenced by the amount and diversity of the training data. Factors such as subject variations, conditions, and sensor setup and placement differences could impact training data quality. The availability of three distinct data sets, collected at different times and from different animals, provided a unique opportunity to assess the models' robustness. Figure 22c overlays the horizontal smooth pursuit results from all three data sets, with data sets 2 and 3 adjusted for consistent gaze range across all sets. Despite session variations, such as different animals, sensor fittings, gaze ranges, and gaze periods, the overall trends and sensitivities appeared similar.

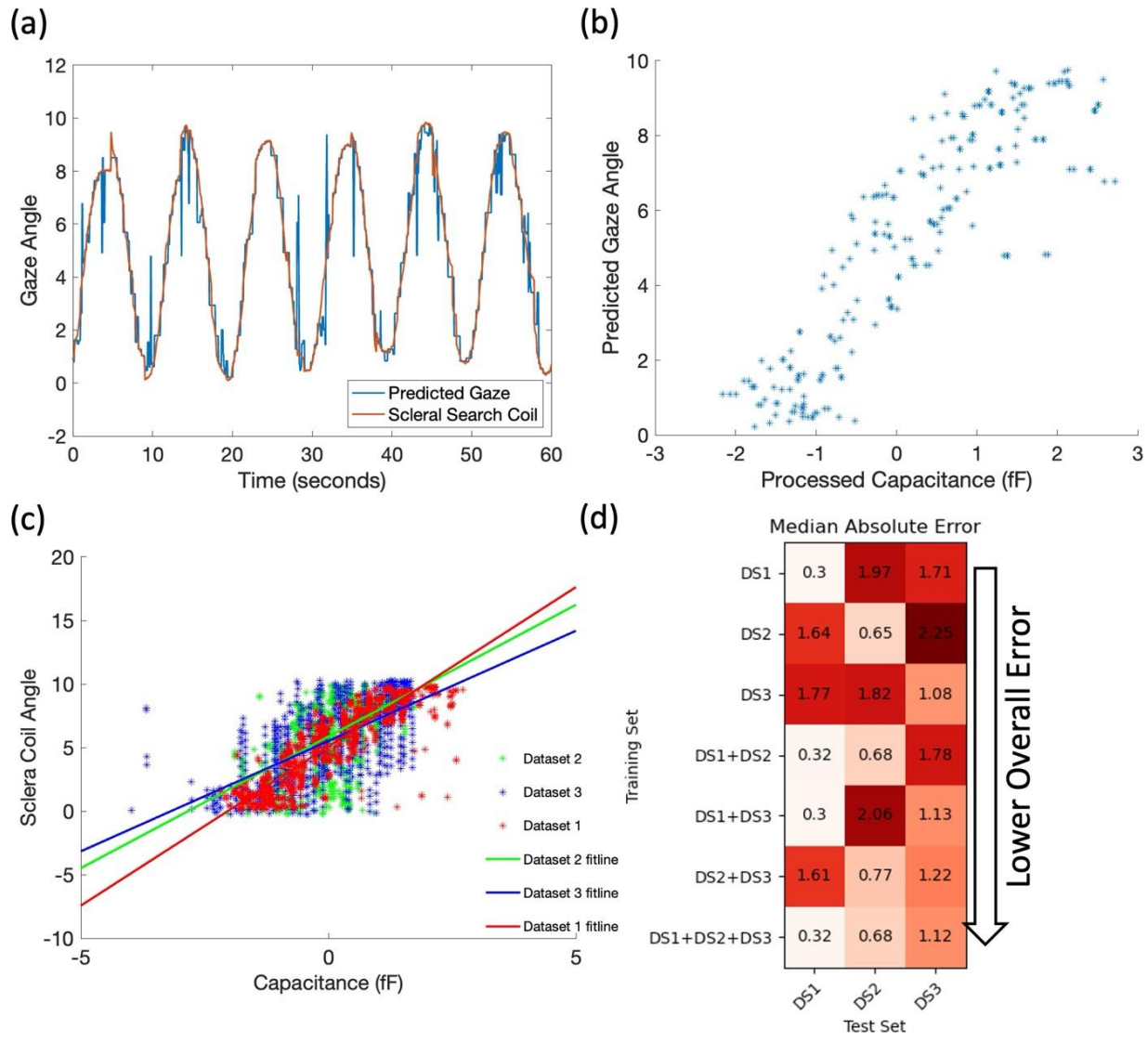

Figure 22. a) Time series of horizontal smooth pursuit at T = 10 s from Dataset 1 (DS1), showing gaze predictions from our custom capacitive eye tracker against actual gaze measurements from a scleral search coil. b) Processed capacitance data and corresponding gaze angle predictions generated by the machine learning model based on the data presented in (a). c) Overlay of three horizontal smooth pursuit tests. Red: Horizontal smooth pursuit at period T = 10 from DS1, animal A1; green: Horizontal smooth pursuit from DS2, animal A1; blue, Horizontal smooth pursuit from DS3, animal A2. d) The median absolute error (MAE) of gaze prediction for horizontal smooth

pursuits, when using regression tree models and trained with various combinations of input datasets, reflecting the model's performance across different training scenarios.

Figure 22d illustrated the MAE when using a regression tree model trained on various dataset combinations to predict test data from either DS1, DS2 or DS3. This capacitive eye tracker, while achieving high gaze accuracy with impressive proximity sensitivity, was also hindered by this sensitivity due to its vulnerability to variations in facial geometry and sensor positioning. As a result, a machine learning model trained exclusively on one session performed well within that session. As expected, its accuracy decreased on other sessions. A model trained on DS1 achieved a low MAE of 0.3° for gaze predictions within the same dataset. However, when applied to predict gaze positions from capacitance values in DS3, the MAE significantly increased to 1.71°. To achieve the best accuracy, recalibration before every use was recommended.

Training a robust model with combined data from multiple sessions could yield consistently good performance across all test sets. As demonstrated in Figure 22d, a model trained with data from DS1, DS2, and DS3 achieved MAE of 0.32° for DS1, 0.68° for DS2, and 1.12° for DS3 in gaze prediction. Although the MAE values of this model were slightly higher than the best results obtained from individual session training (0.3˚, 0.65˚, and 1.08˚), it demonstrated consistent performance across all three datasets without a significant drop in accuracy.

3.5 DISCUSSION

The experimental results demonstrated that the capacitive eye tracker holds the potential to be an accurate, non-contact device for monitoring horizontal and vertical eye movements in non-human primates. The device utilized flexible carbon nanotube-paper composite (CPC)

capacitive sensors to detect small capacitance changes resulting from the movement of the bulging cornea during eye rotation. The small displacement of the sensor-eye distance during rotation resulted in capacitance changes of only a few femtofarad (fF). Enhanced capacitive sensitivity was achieved through the high-aspect-ratio fibrous structures, which increased both the electric field and the surface area [38, 93].

Two factors may improve the current setup. First, selecting a capacitance measurement chip with high accuracy is crucial, but there is a trade-off between the sampling rate, capacitance resolution, and the speed of eye movements. The prototype's CDC limits its sampling rate to 21 Hz, resulting in a higher MAE for tasks involving rapid eye movements. For instance, the MAE for the faster horizontal smooth in DS1 was 1.09˚, which was significantly higher than 0.30˚ for the slower horizontal smooth in DS1. Upgrading to faster CDCs can enhance eye displacement detection accuracy and provide more detailed profiles of eye movement onset, duration, and velocity.

Second, the geometry of the CPC sensor plays a significant role. Since the capacitance change is directly proportional to the sensor's area and inversely proportional to the distance, better capacitive sensitivity and gaze prediction accuracy can be achieved with larger sensors or by positioning sensors closer to the animal's eye. Larger sensors may increase the capacitive field, but they reduce specificity to eye displacement and potentially restrict the animal's field of vision. Future developments may explore fabricating CPC sensors in three-dimensional shapes to increase surface area while maintaining compact dimensions. Such miniaturized sensors, placed closer to the animal's eye, can enhance sensitivity, and refine angular gaze resolution.

Machine learning algorithms were utilized to predict gaze angles from capacitance reading. Due to the low data dimensionality, linear regression, regression tree, and SVR models could be

trained within 1 second, while a neural network could be trained within 10 seconds without a dedicated GPU. These models achieved high accuracy with minimal computational cost. Nevertheless, their performance was constrained by the relatively small training dataset. Calibration for a single session could achieve an MAE as low as 0.30˚ in gaze angle prediction. However, using the model on data from another animal without recalibrating resulted in an MAE exceeding 1.5˚. This limitation could be addressed by session-specific calibration or by enriching the training dataset with data from additional sessions, enhancing the model's adaptability and precision on unfamiliar test data.

In its current form, the device offers a highly customized and wearable platform for non-human primate eye tracking applications. The machine learning-based gaze angle prediction achieved an error as low as 0.30˚ MAE at optimal conditions and 0.80˚ average MAE across all smooth pursuits of all velocities across two animals and three data sets. However, the accuracy fell short compared to high-end desk-mounted commercial trackers like the Tobii Spectrum Pro, which demonstrated accuracy between 0.3 ~ 0.43˚ at a higher sampling rate. Nevertheless, with low power consumption and portability, the wearable capacitive eye tracker stands out for its uniqueness of long-term usage in less restrained settings. This advantage could enable unique animal or human applications, such as our previous work in human eye tracking [94] and wearable neurological screening.

3.6 Conclusion

In conclusion, our study introduced an innovative, non-invasive wearable eye tracking system for measuring both horizontal and vertical eye movements. This system employed CPC

capacitive sensors with fibrous structures to significantly improve capacitive sensitivity. This enhanced sensitivity allowed the measurement of sub-femtofarad level capacitance changes from eye movement. Machine learning was utilized to predict gaze angles from the capacitance value. The prototype eye tracker demonstrated the capability to measure gaze angles with a median absolute error as low as 0.30˚, averaging at 0.80˚. Benchmarking on rhesus monkeys' eye movements revealed a strong linear correlation with the scleral search coil system, achieving correlation coefficients up to 0.97 for horizontal movements and 0.91 for vertical movements. With further refinement, our eye tracker can be a viable alternative to scleral search coil and camera-based systems for researchers, standing out for its lightweight, wearable, and non-contact advantages.

Chapter 4. Capacitive Eye-Tracker for Human Gaze Tracking and Fatigue Monitoring

4.1 OBJECTIVE

The previous three chapters covered a review of capacitance concepts and capacitive sensing, the development and characterization of a highly sensitive, carbon-nanotube paper-based composite (CPC) capacitive sensor, and a sensor application of non-invasive gaze tracking for non-human primates. The previous chapters were all based on flat CPC sensors, which posed challenges for human uses. In this chapter, I introduce a new CPC cylindrical capacitive sensor that has even better capacitive sensitivity than previous CPC sensors while addressing these challenges. Topics covered include comparing cylindrical and flat sensor formats, manufacturing of the new CPC cylindrical sensors, benchmarking CPC cylindrical sensors with identically sized copper cylindrical sensors, 3D face scanning for optimal eye-tracking sensor placement, human gaze tracking, fatigue biomarker characterization, and fatigue-tracking human subject tests.

4.2 INTRODUCTION

Fatigue can cause severe consequences [95]. Fatigue monitoring is crucial for daily life as fatigue leads to as much as 1.62 times accidents rates increase [96-98], reduction of productivity and cognitive functions [99, 100], and contribute to a larger likelihood of physical and mental illness such as diabetes, cardiovascular diseases, and suicide attempts [101-103]. Many methods were introduced for fatigue monitoring, ranging from self-reporting Karolinska Sleepiness Scale

(KSS) [104, 105], reaction-based performance-based Psychomotor Vigilance Test (PVT), to biomarker-based methods such as electroencephalography (EEG) or cortisol [106, 107].

Self-reporting methods like KSS require participants to rate their fatigue on a numerical scale, whereas for KSS, the range varies from 1 representing extremely alert, to 10 representing extremely sleepy [104]. While these methods are easy to conduct, they require temporary interruptions in work and can be subjective. On the other side, in the PVT test, participants are required to react to random visual events, typically presented on a screen, and their reaction times are measured. An increase in reaction time can indicate reduced alertness and increased fatigue. PVT results are quantitively and easy to conduct, besides, its visual event's randomness reduces the memory effect. Nevertheless, PVT can be challenging in real-life monitoring due to the need for uninterrupted test segments, which can last somewhere between 3 to 10 minutes [108]. The EEG is generated by inhibitory and excitatory postsynaptic potentials of cortical nerve cells and can be a valid biomarker for detecting fatigue. EEG is used to monitor brain wave patterns that correlate with different states of alertness and fatigue. Specific EEG markers, such as the presence and increases of theta wave and alpha wave activity, are associated with higher levels of fatigue [109, 110]. While EEG has shown trends with brain arousal, sleepiness, and fatigue, the result varies between studies and individuals. Nevertheless, sampling EEG could be difficult and not feasible outside of the lab environment, besides, EEG signals can be affected by many issues other than fatigue such as eye closures [111], cognitive and memory tasks [112, 113], and emotions [114]. Salivary cortisol levels can drop in people suffering fatigue, nevertheless, biochemistry measurements are not convenient and not suitable for long-term monitoring [115, 116].

Eye-tracking can be an ideal way for fatigue level measurement due to its non-contact nature and being fast and unobtrusiveness compared with EEG or biochemical markers based

methods. Eye-tracking-based fatigue monitoring utilizes biomarkers such as percentage of eyelid closure over the pupil over time (PERCLOS), blink frequencies, and gaze directions to estimate alertness or fatigue level and have seen commercial applications in driver alertness monitoring systems in automobiles [117-119]. Research has shown that an increase in fatigue level can lead to an increase in PERCLOS [117] and blinking frequency [120].

In this chapter, I presented my novel human wearable eye tracker using an even better CPC sensor design. I determined sensor placement through 3D profiling of human eye regions. An online-processing capable eye tracker prototype was developed and benchmarked against the commercial Tobii eye tracker and the accuracy and performance were studied. Detection of blinks and PERCLOS has been verified with the camera. Short-term noise induced fatigue tests have been attempted.

4.3 Cylindrical CPC Capacitive Sensors

4.3.1 Advantages of Cylindrical Sensors

In Chapter 2, I introduced a highly sensitive flat CPC capacitive sensor with superior sensitivity at close ranges. In Chapter 3, I used this sensor to create a non-human primate eye tracker that predicted gaze at high accuracy. However, when adapting the CPC sensor for a human eye-tracker, I have to address a few challenges.

First, despite the high sensitivity, CPC sensors still need to be placed close to the eye for better accuracy. The flat CPC sensor in Chapter 3 had a width of 5 mm and relied on the slide structures shown in Figure 17d to move. On a human-eye tracker, slide structures cannot be integrated due to safety concerns and adverse effects on the vision field. Besides, due to a lack of

shielding, flat CPC sensors' high proximity sensitivity could pick up displacements from the forehead or eyebrow, causing interference with gaze signals.

To address the above positioning and interference issues, a stick-like long electrode was designed to be installed close to the eye and had its sensitivity concentrated at the tip closest to the eyes. Such a design goal can be achieved by affixing a flat sensor at the end of a stick or wrapping CPC materials around a stick to create a cylindrical roll and shielding. The first option could be difficult to implement because of the difficulty of creating tiny, fractured CPC structures and maintaining stable electrical connections. Additionally, the tiny, affixed sensor could be easily damaged during adjustment or use. Using a copper electrode could be more desirable in the affixed sensor setting. Nevertheless, copper electrodes do not have enough sensitivity to capture tiny eye movements, and the rigidness and sharpness of copper foil could pose safety concerns. Rolling CPC electrodes, on the other hand, have the soft fractured cellulose fiber end exposed, which is highly sensitive and safe.

4.3.2 Cylindrical CPC Sensor Fabrication

The capacitive sensor was fabricated with the same CPC material as shown in Chapter 2 [39]. The whole process can be visualized in Figure 23a. The process began with the application of conductive Ag-510 silver ink (Kayaku Advanced Materials, MA, USA) to one end of a long CPC strip to form conductive pads. Around halfway along the strip, a controlled fracture was induced by drawing a water line with a 0.1-mm capillary pen across the shorter edge of the CPC. This pre-weakening allowed for a precise break, leaving a 12 mm segment from the conductive pads intact.

Following this, the long CPC strip was sectioned into several 15 mm-by-12 mm pieces (see Figure 23a). To reduce parasitic capacitance and electromagnetic interference, 1.3 mm thin coaxial shielded cables were used for the sensor connection. Preparation steps involved stripping 5 mm of the cable jacket and setting aside the exposed shielding mesh for later use. To increase electrical contact area and robustness to rolling deformation, I soldered a 2 mm-by-1 mm copper foil to each cable's inner conductor and connected it to the CPC's silver pattern using conductive silver epoxy (MG Chemicals, 8330S-21G, USA) (see Figure 23a, upper right).

The sensor was then rolled around a 1.6 mm diameter soft polyurethane core, starting from the end opposite to the cable connection to maximize bending curvature, thus reducing the likelihood of loose connection. A polyimide self-adhesive tape wrapped over the rolled CPC structure, securing the geometry and providing insulation. A second copper foil was subsequently wrapped over the polyimide tape, exposing a 2 mm section at the top of the sensor. The copper foil was then connected to the shielding mesh I previously set aside to extend the sensor's electromagnetic shielding. The completed sensor had a diameter of approximately 3.5 mm. The length can be over 12 mm for a larger active shielding coverage. The image of the sensor can be seen in Figure 23b.

The SEM image of the sensor can be seen in Figure 23c. The left image shows the fiber networks while the right image shows an individual fiber with width about 40 um. The EDS spectrum of the sample showed a high weight concentration of carbon and oxygen, which is consistent with earlier research attempting to characterize cellulose fibers [121].

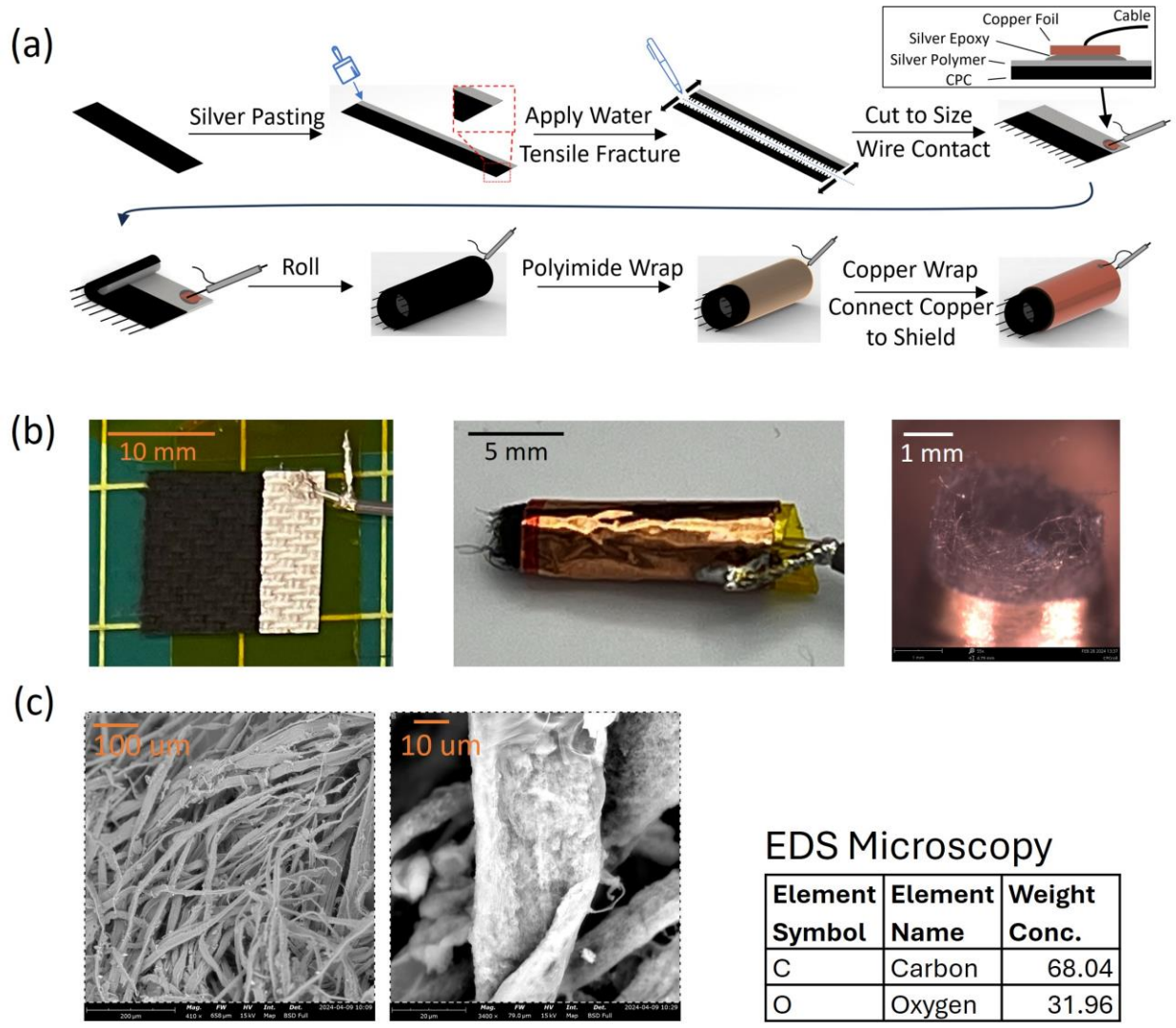

Figure 23. CPC Cylindrical sensors fabrications and images. (a) Steps to make a CPC cylindrical sensor from raw CPC material. Upper right: The sectional view of the wire contact. (b) Left: Unwrapped CPC sensor showing the cable connection and silver pad. Central: The CPC cylindrical sensor side view. Right: Optical microscopy of the CPC cylindrical sensor showing the cross-section of the fractured fibrous end. (c) SEM images of the CPC sensor showing the fibrous network (left), zoomed-in view of individual fiber (middle), and atomic weight concentration through energy dispersive X-ray spectroscopy (EDS) (right).

4.3.3 Cylindrical Sensor Characterization

CPC cylindrical sensors were benchmarked against similarly constructed and identical-sized copper sensors. I made three CPC cylindrical sensors as well as 3 reference copper foil sensors. Both sensors were mounted on a custom-designed carriage on a modified 3D printer (originally made by CReality, Shenzhen, China). The carriage consisted of two parts: a top section with a single circuit board with two AD7747 capacitance-to-digital converters (CDCs) (Analog Devices, MA, USA), which were the same CDC as the non-human primate eye-tracker, and an nRF52840 microcontroller (Nordic Semiconductor, Trondheim, Norway) and a bottom section containing a L-shaped bridge for holding sensors. Figure 24a illustrates the sensor characterization setup.

In the upper section, the microcontroller communicated with both CDCs through independent I^2C interfaces, converting and relaying the measurement data to a connected laptop. Measurement data were continuously read by the laptop but only saved during predefined sampling windows. The carriage's bottom features an L-shaped bridge with slots slightly larger than the sensor diameter, holding the sensors through a friction fit achieved by wrapping them with cut-open silicone tubes (Figure 24a lower-right). The sensor tips were placed about 1 mm from the target.

Three characterization tests were performed on the CPC and copper sensors: baseline capacitance and noise level, capacitive proximity sensing distance, and response to different-sized hemisphere targets.

In the baseline measurements, all six cylindrical sensors (three CPC, three copper) were sequentially connected to a single AD7747 CDC. Three CPC sensors showed an average baseline

capacitance and standard deviation of 229.6 ± 0.41 fF, while the copper reference sensors averaged 184.1 ± 0.47 fF (Figure 24c). Adjusted for the CDC's 122.5 fF baseline, the CPC sensors had an average baseline capacitance of 107.1 ± 0.41 fF compared with copper's 61.6 ± 0.47 fF. The CPC sensor showed a 73.9% higher baseline capacitive while keeping the noise level 13.8% lower.

For the proximity sensing distance test (Figure 24d), CPC and copper sensors were tested in pairs by lowering them from 120 mm to 1 mm above the printer's aluminum print bed in 0.1 mm increments. At each increment, the 3D printer stopped for at least 350 ms to gather around 7 readings and kept the average value. Slots containing two sensors were separated by 12 mm in the x direction. To ensure positional consistency, tests were done in two passes with a 12 mm x direction shift. For the full 120 mm to 1 mm range, the reference copper sensor showed an average capacitance increase of 0.032 pF, while CPC averaged 0.066 pF, a value 106% higher. Using three times the noise level determined in the last baseline test as the detection threshold, the CPC sensors had a proximity sensing distance of 85 mm, compared to 45 mm for the copper sensors, representing an 89 % increase.

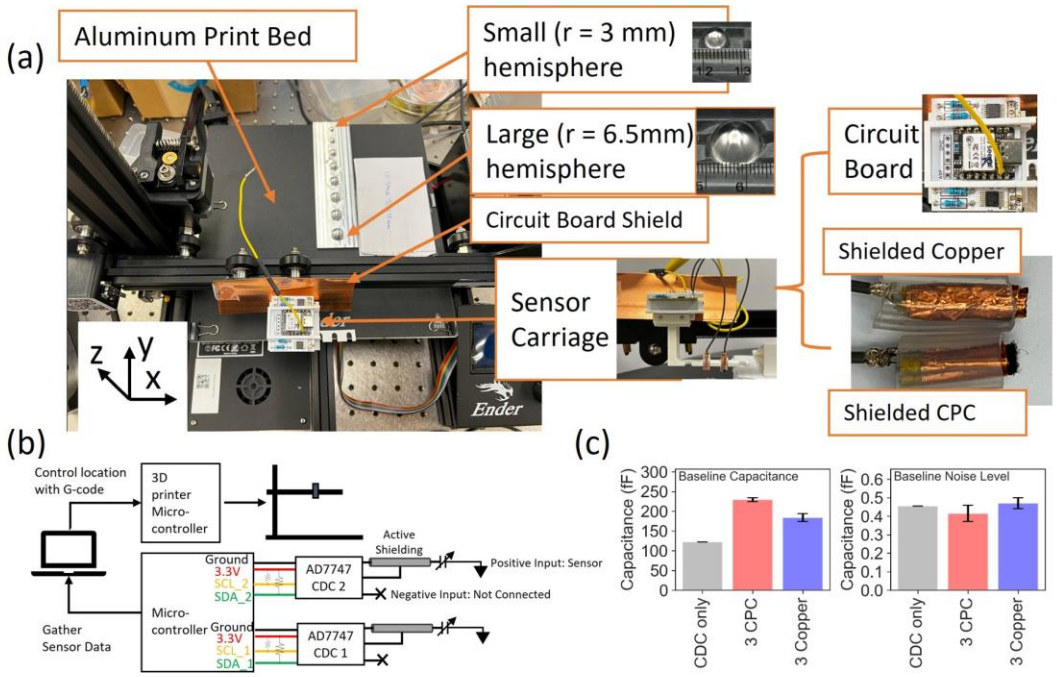
(a)
Aluminum Print Bed
Small (r = 3 mm) hemisphere
Large (r = 6.5mm) hemisphere
Circuit Board Shield
Sensor Carriage
Circuit Board
Shielded Copper
Shielded CPC
z
y
x
Ender
(b)
Control location with G-code
3D printer Micro-controller
Active Shielding
Positive Input: Sensor
Negative Input: Not Connected
Ground
3.3V
SCL_2
SDA_2
AD7747 CDC 2
Micro-controller
Gather Sensor Data
Ground
3.3V
SCL_1
SDA_1
AD7747 CDC 1
(c)
Baseline Capacitance
Capacitance (fF)
CDC only
3 CPC
3 Copper
Baseline Noise Level
Capacitance (fF)
CDC only
3 CPC
3 Copper
(d)
Sensors
120 mm to 1 mm.
0.1 mm
increment
Proximity Capacitive Response
Copper ±1σ
CPC ±1σ
Capacitance (pF)
Sensor Displacement (mm)
Proximity Capacitive Response
Copper ±1σ
CPC ±1σ
(Zoomed to 5 fF)
Capacitance (pF)
Sensor Displacement (mm)
(e)
Sensor move at
0.1 mm increment
At different
Height
10 - 1 mm
Large
r = 6.5 mm
Z = 1.20 mm
Z = 3.10 mm
Z = 5.00 mm
Z = 9.80 mm
CPC
Shown
Only
Capacitance Change (pF)
x (mm)
Copper ±1σ
CPC ±1σ
at Z = 1.20
at Z = 3.10
at Z = 5.00
at Z = 9.80
Capacitance Change (pF)
x (mm)
(f)
Sensor move at
0.1 mm increment
At different
Height
10 - 1 mm
Small
r = 3 mm
Z = 1.20 mm
Z = 3.10 mm
Z = 5.00 mm
Z = 9.80 mm
CPC
Shown
Only
Capacitance Change (pF)
x (mm)
Copper ±1σ
CPC ±1σ
at Z = 1.20
at Z = 3.10
at Z = 5.00
at Z = 9.80
Capacitance Change (pF)
x (mm)

Figure 24. Characterization of the CPC cylindrical sensor. (a) Image of the sensor platform loaded on a 3D printer, which can accurately control the sensor position. (b) Electrical schematics of the characterization setup. The computer concurrently interfaced two microcontrollers, sending G-code to the 3D-printer's microcontroller to move the sensor to a designated location while getting reading from the sensor's microcontroller. Two AD7747 CDCs were installed on each circuit board on their independent i2C channel to interface CPC and copper sensor at the same time. Sensors were connected to positive input in CDCs through active shielded cables. (c) Baseline capacitance measurement of three CPC cylindrical sensors and three copper cylindrical sensors measured through a single CDC. (d) Proximity response of CPC cylindrical sensors and copper cylindrical sensors to the printer bed (aluminum plate of 240 mm-by-240 mm) when sensor descending from 120 mm to 1 mm. 3 sensors mean capacitance change and standard deviation are plotted. The rightmost chart is a zoomed view. (e) Capacitive response of both CPC and copper sensor to the large r = 6.5 mm aluminum hemisphere at different heights. The middle chart only has CPC plotted for less clutter, and the right chart has variable capacitance range to show finer details for larger height tests. (f) Capacitive response of both CPC and copper sensor to the smaller r = 3 mm aluminum hemisphere at different heights.

For different-sized hemisphere tests, sensors moved over aluminum hemisphere patterns at multiple passes at varying heights z. The small and large target had a diameter of 3 mm and 6.5 mm, respectively. These two sizes were chosen as the average cornea-to-lens distance is 3.6 mm [122] and the average radius is 5.75 mm [123], making them suitable for approximating the displacement caused by eye rotation. Sensors moved across the hemisphere centers with an initial 1 mm sensor-to-hemisphere-top distance. Multiple passes were made at different heights with

increasing increments as sensitivity decreased with heights. The average and standard deviation of both CPC and reference copper cylindrical sensor (N = 3) were plotted at heights of 1.2, 3.1, 5, and 9.8 mm.

The CPC sensor consistently outperformed reference copper sensors in the hemisphere test. The capacitance change, calculated from the maximum capacitance minus the minimum is shown in Table 9. For the large r = 6.5 mm hemisphere pattern, as seen in Figure 24e, showed about 70 fF of capacitive response when crossing the top of the hemisphere at 1.2 mm. The smaller 3 mm pattern, as seen in Figure 24f, generates a smaller response at 41 fF. On average, the CPC cylindrical sensor was twice as sensitive as the copper sensors at heights less than 5 mm in both hemisphere pattern sizes. Considering all heights, the CPC sensor is 75% more sensitive than copper in smaller hemispheres, and 99% more sensitive than copper sensors in large hemispheres, a lead consistent with the earlier proximity sensing distance characterization (106%) (Figure 24d).

Table 9. Capacitance change from scanning over hemisphere patterns at different height

Height Z (mm)	**CPC (large pattern) (fF)**	**Copper (large pattern) (fF)**	**CPC (small pattern) (fF)**	**Copper (small pattern) (fF)**
1.2	70 ± 8.3	33 ± 2.3	41 ± 4.4	22 ± 2.1
3.1	23 ± 1.4	11 ± 1.3	17 ± 2.2	10 ± 1
5.0	12 ± 1.1	6 ± 1	9 ± 1.2	5 ± 0.8
9.8	4.2 ± 1	2.4 ± 0.9	3.8 ± 0.7	2.3 ± 0.8

4.4 EYE-TRACKER DESIGN AND VERIFICATION

4.4.1 Facial Scanning and Sensor Placements

The placement of eye-tracking sensors around the eye was determined through eye displacement profiling at different gazes. To study how displacement on the eye region changes when the eye rotates, I used 3D scanning to profile the eye region at different gaze directions. As the cornea was transparent and could not be captured by a 3D scanner, the focus was on profiling the adjacent eyelid area. Instead of analyzing the entire mesh, markers made from masking tape squares with blue dots were placed at specific positions around the eye for detailed study (see Figure 25a). Markers were placed near the edge of the upper eyelid and spread across the temporal, central, and nasal sides. These markers served as measurement markers since they moved with eye movements (labeled A1 – A3, C1 - C3 in Figure 25a). Markers outside the eye region (labeled A, B, C, and O* in Figure 25a), such as those on the forehead or cheek area, were assumed to be

stationary across gaze movements and served as reference markers for aligning different 3D scans. Marker O* was not a physical tape square. Instead, it represented the interpolated middle point between A and C, serving as the center for multiple scan alignments.

Five subjects were scanned following the same protocol. Volunteers were instructed to fixate their gaze in a direction (either center, upper, lower, left, or right) for 5 seconds without blinking. During this time, another staff used a handheld EinScan H 3D scanner (Shining 3D, Hong Kong, China) to scan the participant's face. This scanner used infrared illumination instead of flash, providing less accurate scanning but safe for human eyes. One scan was created for each gaze direction per participant, and the 3D coordinates of each marker were read from the 3D mesh. To estimate the measurement accuracy, I calculated the median absolute deviation (MAD) of the L1-norm between reference markers A and marker B as it should be constant for each subject. Among all five subjects, the point A-B L1-norm MAD varied between 0.8 mm to 1.41 mm, indicating accurate scanning accuracy (see Figure 25b).

Each scan generated a 3D mesh centered on the scanner body with an axis based on the scanner's facing direction. As a result, marker coordinates from different scans must be transformed into the same global Cartesian coordinate for comparison. I defined a global coordinate system whose origin was at point O, the middle point between A and C, and x, y, and z represented protrusion, width, and elevation (Figure 25a). This affine transformation can be represented by Equation 4.1.

$$P_{global} = T * p_{local}$$

$$P_{global} = \begin{bmatrix} x_{global} \\ y_{global} \\ z_{global} \\ 1 \end{bmatrix}, T = \begin{bmatrix} r_{11} & r_{12} & r_{13} & X_0 \\ r_{21} & r_{22} & r_{23} & Y_0 \\ r_{31} & r_{32} & r_{33} & Z_0 \\ 0 & 0 & 0 & 1 \end{bmatrix}, p_{local} = \begin{bmatrix} x_{local} \\ y_{local} \\ z_{local} \\ 1 \end{bmatrix} \quad (4.1)$$

where the vector p_{local} contains the location in the scanner coordinate system, P_{global} contains the location in the global coordinate system, and the T matrix contains an affine transformation needed to convert a coordinate from the scanner coordinate system location to the global coordinate system location. For each participant, I first established the P_{global} for reference markers A, B, C, and O* by manually inspecting a scan with center gaze. Then, for each scan of the same participant, I first estimated T satisfying the transformation for all reference markers A, B, C, and O*. Once T was calculated, all measurement marker coordinates from the same scan could be transformed into the global coordinate system (see Figure 25c).

While the scanning results varied between participants, some common trends were found. For each measurement marker location, I calculated how this marker's elevation and protrusion change from the central gaze when gazing up, down, left, and right. The five participants' average and MAD (see Equation 3.2) are shown in Figure 25d. Ideally, one marker is only sensitive to one gaze direction, where complementary gazes produce opposite responses and orthogonal gazes produce small responses (for example, an ideal scenario for the vertical gaze sensor is protrusion increases with upward gaze, decreases with downward gaze, and almost no response to either left or rightward gaze).

The vertical gaze movements caused large protrusion and elevation changes in both nasal (C1, A3) and center (A2, C2) marker points (see the red and blue arrows in row 2, center markers, and row 3, nasal markers of Figure 25d). The center marker positions were better than nasal positions as vertical movement produced a larger change in elevation and protrusion, therefore a larger and more prominent proximity capacitance change. The horizontal gaze, however, was not particularly prominent in any of these marker locations. Since central and nasal markers were more sensitive to vertical movements, the two temporal side markers were chosen for horizontal measurements. Both saw an elevation and protrusion drop on opposite side movements (rightward gaze on the left-eye temporal side and leftward gaze on the right-eye temporal side, Figure 25d, row 1) while having a minimal response to same-side movements. Horizontal movements could be measured by taking the difference between them.

In summary, the left and right eye center markers were best for vertical gaze sensing due to their large magnitude but opposite responses to upward and downward gaze. Although no marker position was ideal for horizontal gaze sensing, left and right temporal markers had low sensitivity to vertical gaze and opposite sensitivity to left and right horizontal gaze, making it possible to combine sensors at these locations for horizontal measurements.

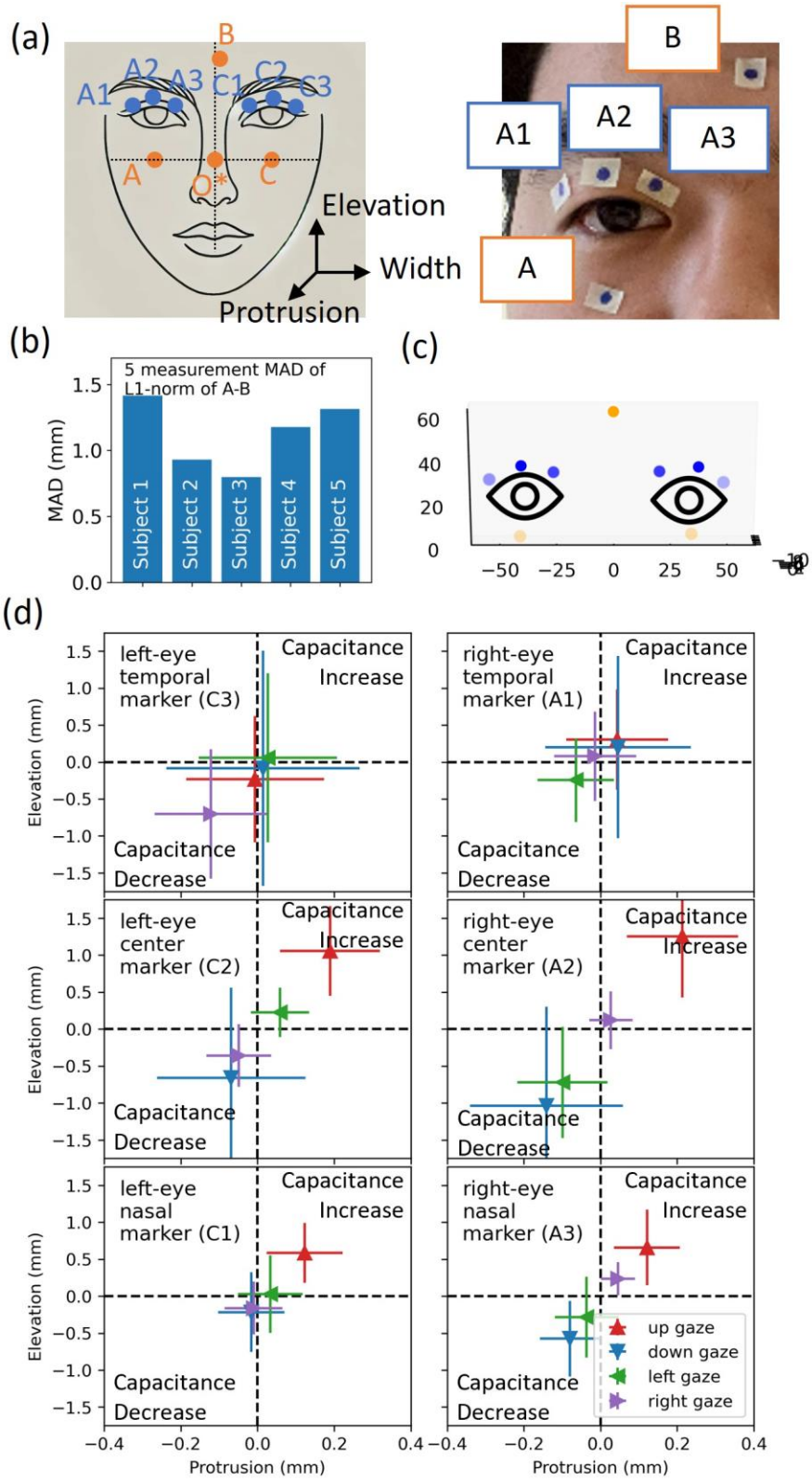
(a)
B
A2
A3
C1
C2
C3
A1
A
C
Elevation
Width
Protrusion
B
A1
A2
A3
A
(b)
5 measurement MAD of L1-norm of A-B
MAD (mm)
Subject 1
Subject 2
Subject 3
Subject 4
Subject 5
(c)
(d)
left-eye temporal marker (C3)
right-eye temporal marker (A1)
left-eye center marker (C2)
right-eye center marker (A2)
left-eye nasal marker (C1)
right-eye nasal marker (A3)
Capacitance Increase
Capacitance Decrease
Elevation (mm)
Protrusion (mm)
up gaze
down gaze
left gaze
right gaze

Figure 25. Face scanning to identify ideal sensor location for eye tracking. (a) The marker groups and location on eye. Group A is around the right eye and Group C is around the left eye. Marker B was near the center of the forehead, and O* was the midpoint between A and C, serving as the origin for scan. Reference markers (orange) were used to align scans to global coordinate while measurement markers (blue) were used to determine protrusion and elevation during gaze movement. (b) MAD of L1-norm between point A and point B. (c) Markers locations in transformed coordinates. (d) The five-subject mean and MAD of marker elevation and protrusion, grouped by maker location. Each panel in this graph represents a measurement marker (C1 - C3 and A1 - A3) and each arrow inside represents a directional gaze's (up, down, left, right) elevation and protrusion change from the center gaze. Increases in protrusion or elevation lead to an increase in capacitance compared to center gaze.

4.4.2 Human Capacitive Gaze Tracker

Following the scanning result from the last section, I designed a CPC eye-tracker with four sensors into two differential pairs. Sensor pair 1 contained two sensors installed at the temporal side of both eyes to sense the horizontal gaze movement. Sensor pair 2 was above the center of both eyes but had slightly different spacing such that the signal did not cancel. While using a single-ended setup for vertical sensing might be good enough from the result in Figure 25d, a differential setup provided common signal rejection, making the CPC eye-tracker less vulnerable to blinks, droops, and eye closures, which had large vertical signal amplitude but were synchronized on both eyes. All four sensors were adjustable by users at a sensor-to-eye distance

between 5 and 10 mm, ensuring user comfort. The picture of the eyeglass can be seen in Figure 26a-b.

All four sensors were connected to an FDC1004 (Texas Instruments, TX, USA) CDC. Compared with the AD7747 CDC used in earlier sensor characterization sessions and Chapter 3, the FDC1004 CDC operated on the same switched-capacitor principles but offered a tenfold increase in sampling rate and supported four sensors. Nevertheless, it had a lower measurement accuracy and signal-to-noise ratio. Despite that, this compromise was acceptable because of the larger capacitance change from gaze due to improved sensor design and the larger adult human eyeball. The nRF52840 microcontroller was still used to interface with the CDC and relayed data to a computer through either Bluetooth Low-Energy protocol or USB protocol. USB communication was used in this section for the transmission bandwidth and latency performance.

CPC eye-trackers could be integrated into off-the-shelf eyeglass frames, allowing easy and non-obtrusive eye monitoring. This compatibility was demonstrated in a prototype created using a modified off-the-shelf safety visor. During the modification, the protective polycarbonate lens of the safety visor was removed, and two strips with equally spaced slots were attached to the top of the eyeglass frame to securely hold the sensors out of the vision field. The sensing circuitry was mounted on the forward-left side of the frame, just outside the left temple area.

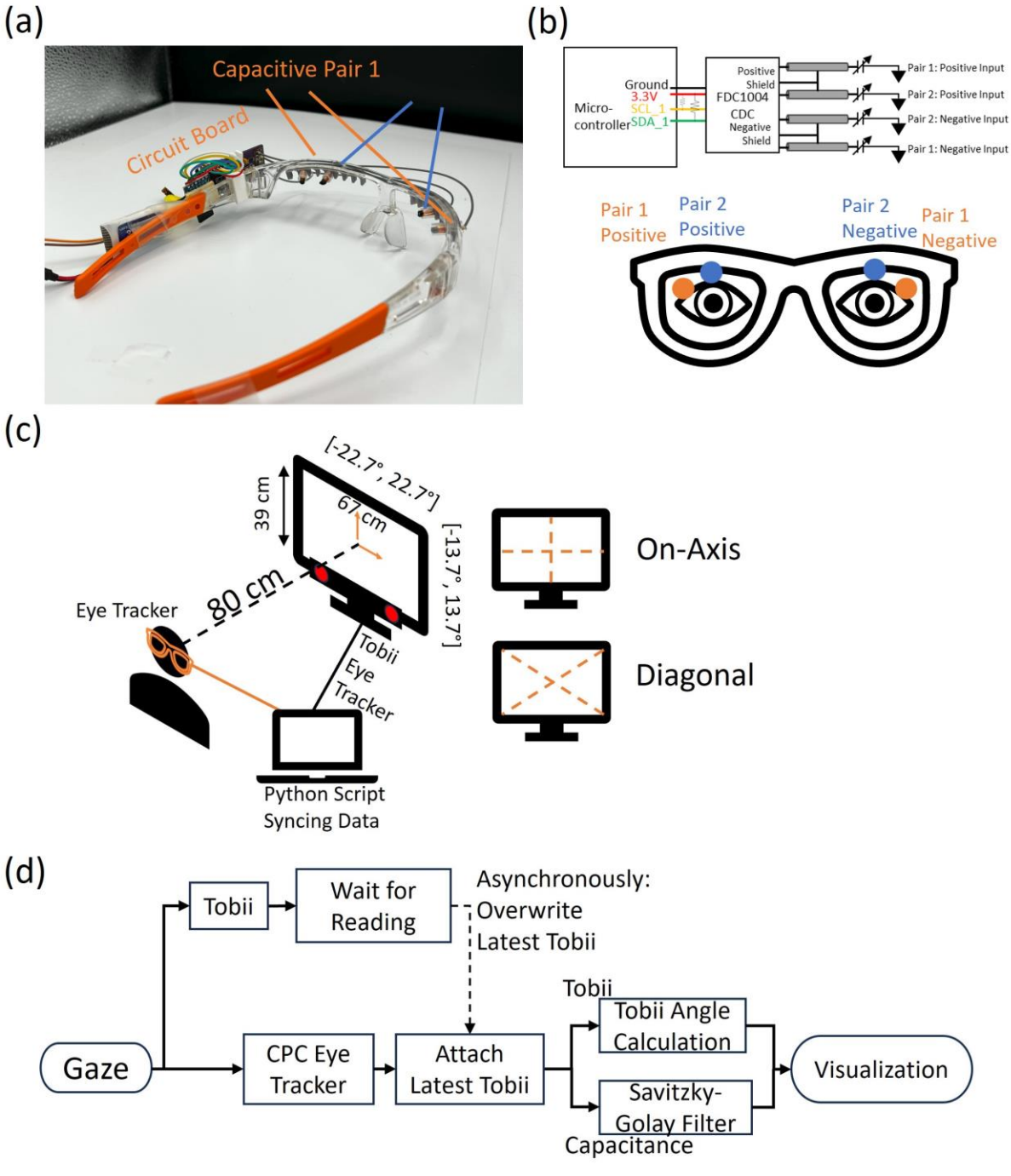

Figure 26. The CPC capacitive human eye trackers and setup for gaze tracking accuracy benchmark. (a) Picture of the capacitive gaze tracker. (b) Electrical schematics and sensor pair assignment. Both positive differential inputs are above the left eye with the pair 1 at temporal side

and pair 2 at center. The pair 2 negative is 2 mm higher than positive in this case. (c) Illustration of test setup. The screen has a size of (67, 39) cm, and participants sit at 80 cm. The full screen size is equivalent to a horizontal gaze angle range of 45.4°, vertical angle gaze of 27.4°. (b) The flowchart of the test. The samplings of the reference Tobii eye-tracker and the CPC eye-tracker are independent, and latest sampled data from the Tobii is appended to every CPC eye-tracker measurement regardless of whether it has been refreshed.

The accuracy of the capacitive CPC eye tracker was benchmarked against the Tobii Pro Nano (Stockholm, Sweden), a commercial pupil and corneal reflection (PCR)-based eye-tracker. Participants sat approximately 80 cm from a 31-inch computer screen with a dimension of 67 cm by 39 cm (see Figure 26c, left). A custom Python script concurrently gathered the CPC eye-tracker's reading via USB and the Tobii eye-tracker's left-eye gaze data using the manufacturer-supplied Tobii Pro Python SDK. For each received CPC eye-tracker data, the latest Tobii reading was appended and written to a CSV file for later analysis. The CPC eye-tracker had a sampling of 189 Hz. The CPC eye-tracker and the Tobii eye-tracker updated asynchronously with the Tobii eye-tracker's data updated approximately every sixth CPC sample, equating to a sampling rate of about 31.5 Hz.

Participants engaged in one-minute simulated saccade tracking tasks categorized into simpler on-axis cases and more complex diagonal cases (see Figure 26c, right). Unlike the non-human primate eye-tracker in Chapter 3, for both cases, there were neither red laser dots nor on-screen visual cues guiding the gaze. Instead, the gaze path was rendered on screen and participants moved to any point on the gaze path at their discretion. For the on-axis tasks, participants were asked to perform the saccade tracking on horizontal and vertical axes intersecting at the center of

the monitor. In contrast, the off-axis tasks required participants to perform a saccade gaze on the diagonal axis across the screen.

The data processing pipelines can be seen in Figure 26d. Capacitance data were processed through the Savitzky-Golay filter to smooth out high-frequency noises. Unlike Chapter 3, wavelet methods were not used due to the human capacitive eye-tracker's better signal-to-noise ratio and higher sampling rate. The Savitzky-Golay filter, with a window length of 64 data points and a polynomial order of 5, required fewer parameters to tune and computed much faster, allowing possible real-time processing. Both capacitive pair 1 and pair 2's readings were plotted with the commercial eye-tracker.

Tobii eye-tracker's data, reporting as a pair of numbers between 0 and 1, represented the on-screen gaze location as percentages of screen width and height. Tobii's gaze location followed the sign convention of computer graphics and originated from the upper-left corner of the display, increasing when gazing rightward or downward. Tobii eye-tracker returned a null value if on-screen gaze location could not be found due to eye closure, gaze out of screen area, or gaze velocity higher than tracking capacity. In this benchmark, I treated the center of the screen, or (50%, 50%) location as reported by Tobii as 0° gaze and upward gaze as positive. Thus, the gaze angles were calculated using the following formulas, with the and vertical gaze angle flipped to adhere to the sign convention. The conversion is in Equation 4.2.

$$Horizontal\ Gaze\ Angle = atan2(w_{screen} * (W_{tobii} - 0.5), d)$$

$$Vertical\ Gaze\ Angle = -atan2(h_{screen} * (H_{tobii} - 0.5), d) \quad (4.2)$$

where the lowercase w and h are screen width and height, uppercase W, H represents the percentages given by Tobii, and d is the spacing between participant and display.

The comparison result is shown in Figure 27a-b. In the Horizontal component of the "on-axis" test, the sensor pair 1 capacitance was linear with the gaze angle up to around ±10° from the center. Performing a least-squares fitting on a cubic function model (Equation 4.3)

$$C = ax^3 + bx^2 + cx + d \tag{4.3}$$

where c is the capacitance, x is the gaze angle from the Tobii data, and a, b, c, d were function coefficients to be calculated from data where the squared loss was minimized. The cubic function fitting had an R2-score of 0.892. Calculating the sensitivity (fF/°) from the fitted line, the sensitivities were 0.53 fF/°, 0.34 fF/°, and 0.42 fF/° for horizontal gaze angles smaller than -10°, between -10° and 10°, and larger than 10°, respectively.

For the vertical component of the on-axis test, the cubic fitting returned an R2-score of 0.814, and the sensitivity is around 0.57 fF/° in sensor pair 2. While capacitive sensor reading still showed good agreement with the Tobii gaze data, it was affected by horizontal gaze. Encoding each gaze point with color based on horizontal gaze, I saw an up-to-4 fF capacitance change caused by horizontal gaze movement. 4 fF was approximately equal to 6.6° of vertical gaze angle, considering a horizontal gaze range of ±22°, the ratio is about 30%.

For the diagonal cases, the time series plot showed that sensor pair 1's horizontal gaze sensitivity varied based on the eye's vertical gaze. For example, as seen in Figure 27b, from seconds 0 to 10, the gaze was upper-right, and sensor pair 1 was highly sensitive to horizontal

gaze. However, in seconds 10 to 15, the gaze was lower-right, and the same magnitude rightward horizontal gaze produced a much less noticeable capacitance change. The only difference was that in the latter time, the vertical gaze was downward. After encoding each gaze point with color based on vertical gaze, I could observe that sensor pair 1 had much higher horizontal gaze sensitivity when also gazing upward. Using the same cubic functions curve fitting, when the vertical gaze was upward, the horizontal sensitivity was higher, with sensitivities of 1.7 fF/°, 0.52 fF/°, and 0.48 fF/° for horizontal gaze angles smaller than -10°, between -10° and 10°, and larger than 10°, respectively. Conversely, when gazing downward, the horizontal sensitivities were at 0.09 fF/°, 0.19 fF/°, and 0.05 fF/°, respectively. The horizontal gaze sensitivity when gazing upward was about 9.4 times higher than gazing downward, and 4.9 times better than gazing center from the on-axis case. This difference was reasonable as all sensors were located on the upper side of the eye, when gazing downward, the distance between the scleral-corneal junction and the sensor increases. As capacitance sensitivity was inversely proportional to distance, the sensitivity became much smaller as distance increased.

Finally, the vertical component of the diagonal model was evaluated. When the horizontal gaze was to the right side (positive), the linearized sensitivity was about 0.48 fF/°, and the other one was 0.52 fF/°. Both values were similar, indicating the vertical sensitivity is not that affected by horizontal gaze, as the displacement to the sensor remained relatively unchanged regardless of horizontal gaze.

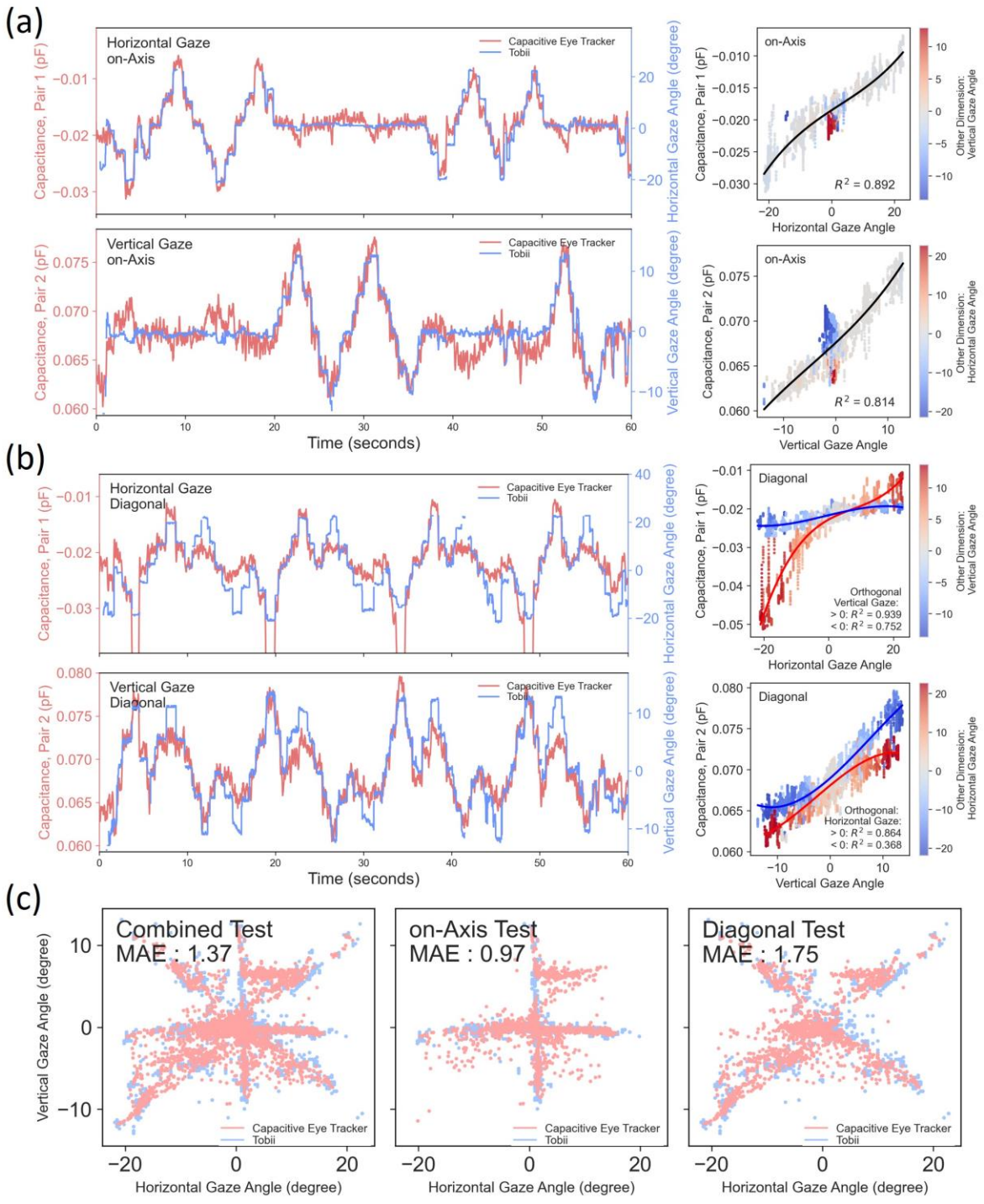

Figure 27. Capacitive response corresponding to different gaze location during on-Axis and Diagonal movements. (a) Capacitance signal and Tobii Eye-tracker recording of on-Axis eye movement. The horizontal and vertical components of the gaze angle and sensor capacitance are

plotted in a time series (left) and comparison (right). Tobii (blue line in time series) lose gaze track at a larger gaze angle or a saccade spanning a large angle. In right-side comparison charts, the gaze points are color encoded by gaze angle in the orthogonal direction. (b) Capacitance signal and Tobii Eye-tracker recording of diagonal eye movement. The horizontal and vertical component of the gaze angle and sensor capacitance, plotted in a time series (left) and comparison (right). (c) Using an 80-20 train-test split, the test case gaze from Tobii (labelled as Actual), and from custom eye tracker device and machine learning (labelled as Predicted).

Using machine learning, it's possible to deal with non-linearity and cross-channel interaction and make an accurate gaze prediction. Based on the machine learning exploration in Chapter 3, tree regression could yield accurate results. For this task, a regression tree ensemble was used, with detailed hyperparameters listed in Table 10. To prevent the model from getting too complex by overfitting edge cases, I limited the maximum tree depth to 15 while requiring a minimum of four gaze points to make a feature split. The dataset combined results from both on-axis and diagonal test cases. Using an 80%-20% train-test split and a random state of 0, the results are shown in Figure 27c. The figure demonstrated that both diagonal and on-axis cases can be predicted well. However, the effect of vertical gaze on horizontal gaze sensitivity led to uncertainties in horizontal gaze predictions, especially when vertical gaze was close to or below zero. Overall, the device predicted gaze with a mean absolute error (MAE) between 0.97° and 1.75°, with combined cases near 1.37°.

Table 10. Regression Tree Ensemble parameters for human gaze prediction

Parameters	**Hyperparameters**
Model Type	Regression Tree Ensemble
Number of Trees	150
Max Depth	15
Minimum Sample per Leaf	4

In conclusion, the wearable CPC capacitive eye-tracker demonstrated high performance in tracking gaze when benchmarking against the commercial Tobii Pro Nano eye-tracker. Due to sensor placements, the CPC eye-tracker's horizontal gaze sensitivity varied with gaze direction, with sensitivity higher for upward gaze. With machine learning, the eye-tracker predicted gaze with a median absolute error (MAE) between 0.97° and 1.75°.

4.5 Fatigue Tracking with the Capacitive Eye Tracker

4.5.1 Eye-tracker Configuration for Fatigue Monitoring

A fatigue monitoring system was developed based on the gaze tracker. In the gaze tracker, I used differential sensing to attenuate blinks and eye closures. For fatigue monitoring, I will use blink and eye closures as biomarkers. As a result, the vertical channel in the eye tracker was switched to a single-ended setup (Figure 28a). Besides, due to the long running time for fatigue monitoring, the wearable fatigue monitor can generate more data than its internal memory can hold. To address this, a micro-SD card was used to buffer data or store it for later analysis. Since

writing data to a micro-SD card can take a long and unpredictable amount of time, a double-buffering technique was implemented. This meant two separate buffers were used to store the data temporarily; while one buffer was being written to the SD card, the other buffer collected new data. This ensured no data loss even when operating at a high sampling rate. A real-time operating system (RTOS) helps manage this process, ensuring no data gets lost.

The capacitive data were sampled at 200 Hz and smoothed with the same Savitzky-Golay filter of 64 window size, 5 polynomial order. Blinks and eye closures can be seen as a sudden dip of the capacitive signal due to the temporary retraction of the eyelid during eye closure (as seen in Figure 28b). To identify the peaks from normal gaze movement, I used *'scipy.signal.find_peaks'* function to automatically detect them. In its default configuration, the find_peaks algorithm detects every peak (Figure 28c, first row). To identify significant signals that stand out against noise, a minimum peak prominence was required. Given the variability in wearing positions, face geometry, and different blinks/ eye closure behaviors, it's impractical to decide an one-size-fits-all prominence threshold. Instead, I used a threshold based on signal standard deviation. A 1-Hz cut-off, second-order high-pass filter was used to attenuate gaze movements, which usually had a longer timeframe. The threshold was subsequently calculated as twice the standard deviation of the filtered signal. The improved signal detection can be seen in row 2 of Figure 28c.

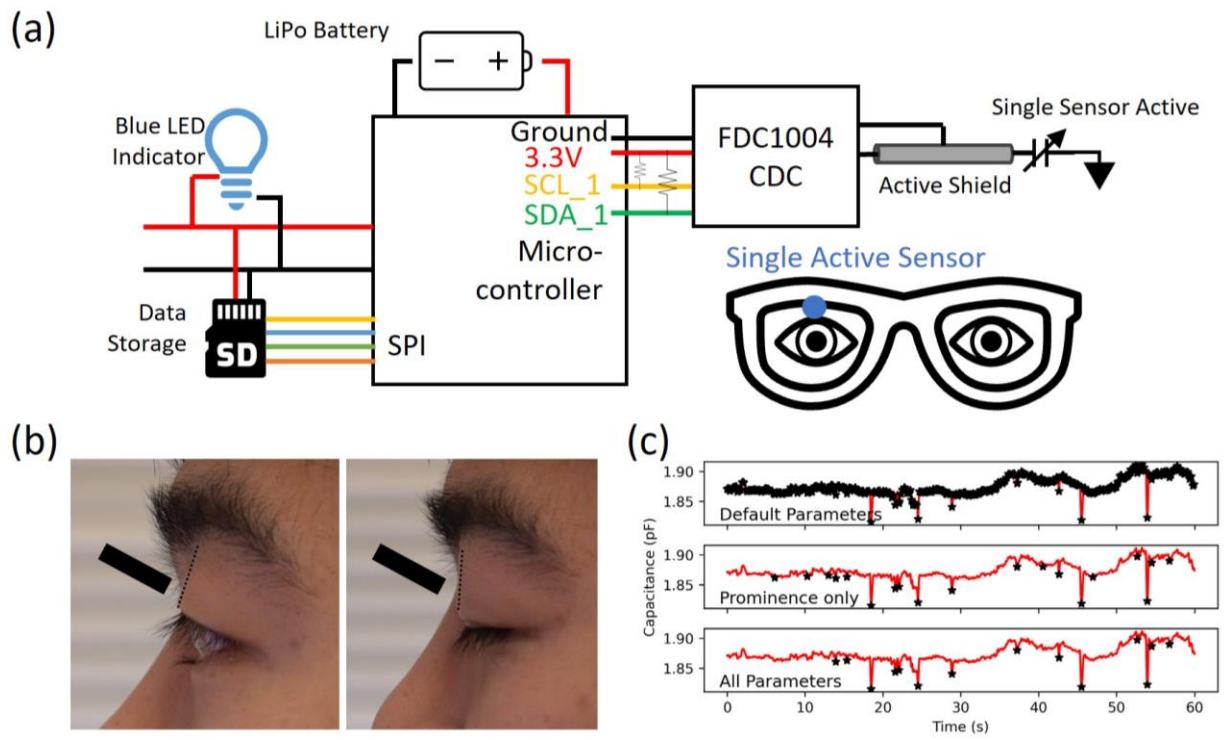

Figure 28. The signal from eye closure. (a) The schematic of the eye-tracker in the fatigue tracking mode. Only one sensor data is collected while others are disabled in the software. Another blue indicator LED, LiPo battery and SD card adapter are installed for storing data during unplugged use. (b) Capacitance decreases from eye closure as the eyelid retracts from the vertical sensor location. The sensor locations are labeled as black rectangles, and the eyelid boundary is in dashed lines. (c) Blinks and eye closures detected by different parameters in the *find_peak* algorithm. The star marker indicated the detected eye closures. Row 1: Using all default parameters. Row 2: Using the Minimum Peak Prominence in Table 11. Row 3: Using all parameters.

Despite improvements, the detection algorithm still had a few false detections where the *find_peak* algorithm incorrectly identified the minima of a downward gaze as blinks. For instance, a false blink was detected around the second 48 as the algorithm treated it as a local minimum for

a long dip between the second 45 and second 53. To better detect blinks rather than gaze movements, the algorithm's parameters were tuned to align with typical blink characteristics. Multiple research across demographics have found the blink duration range between 0.25 to 0.55 seconds [124-128]. As a result, I set the width of the peak to be between 0.1 to 0.7 second when evaluated at 50% of the peak's relative height (RH), and the minimum separation between consecutive blinks was set to 0.3s. The full parameters for the blink detection algorithm are in Table 11.

Table 11. Parameters for blink detection algorithms for capacitive eye-tracker

Peak Detection Parameter	**Peak Detection Parameter Value**
Peak Width	[0.1, 0.7] second
Relative Height for Eye Closure Time Calculation	Width at 50% peak height
Minimum Spacing between Consecutive Blinks	0.3 s
Minimum Peak Prominence	Standard Deviation of high-pass (f_s = 1 Hz, order = 2) filtered signal

The detected blinks and durations using the tuned algorithm can be seen in Figure 28c, row 3. The accuracy of this algorithm was further validated through a test with manual counting.

4.5.2 Fatigue Biomarker Detection and Verification

Blink frequencies and PERCLOS were biomarkers detected using the capacitive eye-tracker for fatigue characterization. The capacitive eye-tracker's biomarker detection was validated against camera footage.

The setup can be visualized in Figure 29a. For the video acquisition, a digital camera was set up on a tripod on the same level as the subject's eyes. The camera was placed at a sufficiently far distance to capture the entire face of the subject and recorded video at 1080p resolution and 60 frames-per-second (fps). Subjects were asked to sit still on a chair and look at the camera lenses for over 3 minutes. When the eye-tracker started up, the installed blue LED light briefly lit up for 2 seconds before starting any sampling. The video segment prior to the LED indication was trimmed.

Subsequently, the video was divided into 6 counts of 30-second segments using the *FFmpeg* software tool. For each video segment, the blink count and PERCLOS were counted manually, as well as automatically with the capacitive eye-tracker and a computer-vision-based eye closure counter for cross-references. As shown in the flowchart Figure 29a, in the manual detection workflow, every 3 frames (50ms) of frames of video were sampled and compiled into a collage for manual inspection. Each frame resembling eye closure was labeled, and the total number of such frames was counted. Each frame labeled was considered as a full 50 ms of closure, a reasonable assumption given that blink and closure durations are much longer than 50 ms. The capacitive sensor blink detection used the algorithm described in the last section.

In the computer-vision-based detection, the participant's face was detected using the *frontal_face_detector* module from the *dlib* software package [129] with the pre-trained

shape_predictor_68_face_landmarks facial landmark model. For each video frame, 6 landmark points (p1 to p6 in Figure 29a) were identified from the eye region, and the eye aspect ratio (EAR) was calculated as Equation 4.4.

$$EAR = \frac{\left||p_2 - p_6|\right| + \left||p_3 - p_5|\right|}{2\left||p_1 - p_4|\right|} \tag{4.4}$$

where a dip in EAR between an eye-closure threshold representing eye closures [130]. Through the experiment, I found EAR changes with head rotation. Specifically, the EAR reduces when subjects rotate their heads vertically, therefore causing false detection. Thus, the same *find_peaks* algorithm used in the capacitive eye-tracker was ported to detect EAR dips, with peak width and minimum separation parameters set identically. The EAR dip threshold was set at 0.22, with a prominence higher than 0.04.

The result is in Figure 29b-d. In Figure 29b, a 30-second capacitance signal from the capacitive eye-tracker is plotted along with the EAR calculated by the computer-vision algorithm. It is evident that blinks detected by the capacitive eye tracker correspond one-to-one with EAR dip events. Unlike the EAR-based algorithm, the capacitive eye tracker can also detect gaze movement, as seen in the lower-magnitude, longer time-frame capacitance changes. Figure 29c shows a zoomed-in view of a specific blink's capacitance change as well as the corresponding video frame. The 50% relative height (RH) line, whose length was treated as blink duration, was marked red.

Results from three subjects are shown in Figure 29d. The capacitive eye-tracker showed good agreement with the manual counting as well as the computer-vision-based algorithm. The capacitive eye-tracker, as well as the computer-vision-based algorithm, is expected to miss less than 1 blink and less than 1% of PERCLOS per 30-second segment. However, the capacitive eye tracker does over-count blink and PERCLOS at times, as seen in outliers. This over-counting outlier indicates a potential impact from the gaze movement, where a blink conjugated with a downward gaze could appear longer.

In this section, I found that the capacitive eye-tracker could measure blink frequency and eye closure durations, which were important digital biomarkers for eye-based fatigue detection. Benchmark results against manual counting and computer-vision-based detection methods showed that the capacitive eye tracker could accurately track these two biomarkers. In the next section, I will test the capacitive eye-tracker with noise-induced fatigue.

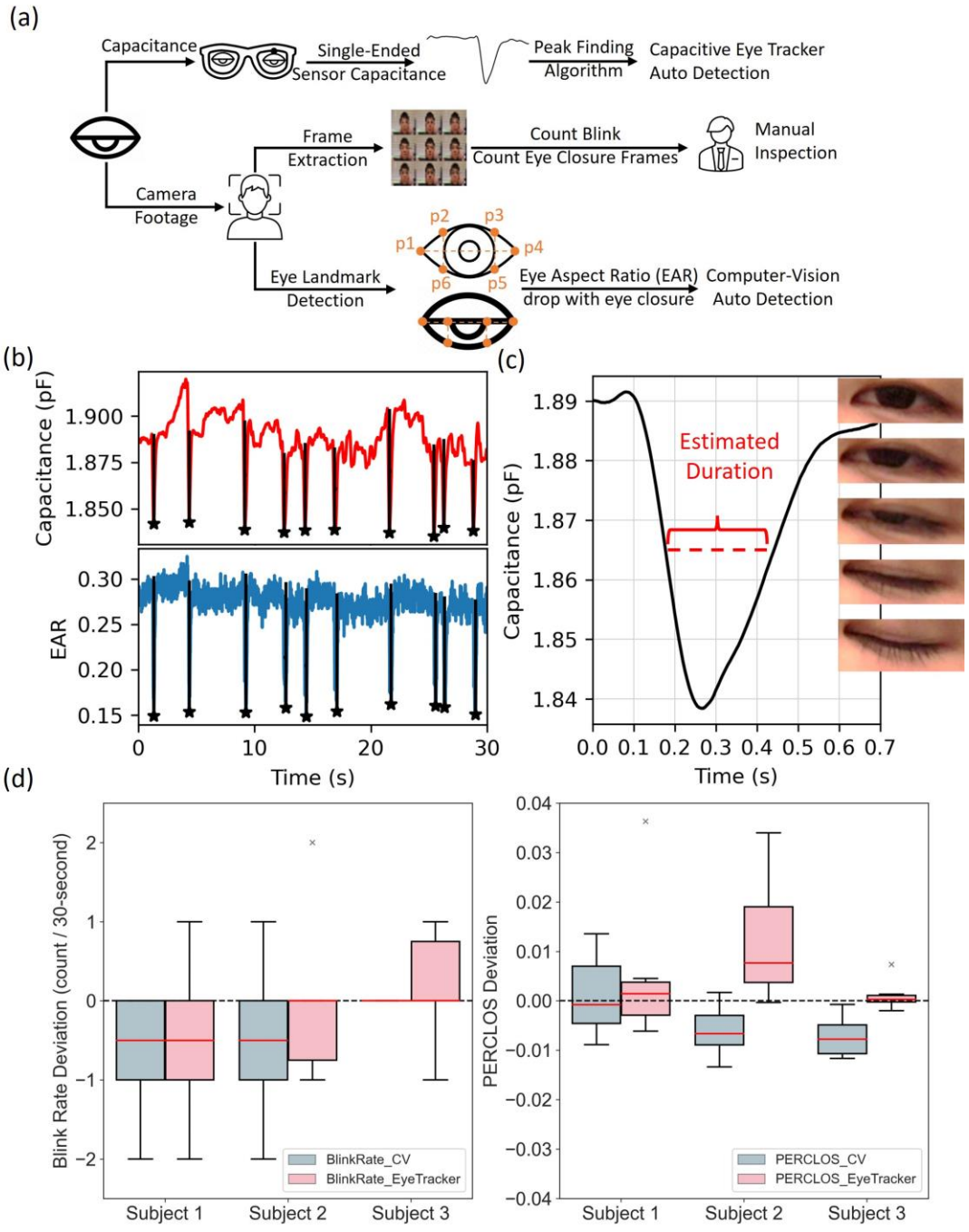

Figure 29. Capacitive eye-tracker based blinks and Percentage of eyelid closure over the pupil over time (PERCLOS) digital biomarker detection, benchmarked against manual counting and computer-vision based algorithms. (a) Flowcharts show how blinks and PERCLOS are counted with all three methods. The 6 landmark points (p1 – p6) for Eye Aspect Ratio (EAR) calculation

are labelled. (b) Comparison between capacitive signal (upper) and EAR from computer-vision based method. The automatically identified blinks and change amplitude are labelled by the star symbol and vertical line. (c) Zoomed view of a closing edge of a blink as well as the corresponding video frames, placed at the capacitance level corresponding in time. This specific blink starts at around 100 ms time mark, took about 150 ms for eye closure, and the reopening took about another 300 ms. Eye closure time is the peak width estimated at half of the peak prominence, represented as the red dashed line. (d) Statistics for the whole 3-minutes test for 3 subjects. The statistics are calculated on 30-second segments. Left: Blink count per 30-second deviation from manual counting from custom eye tracker (dark teal color) and camera (pink). Right: PERCLOS deviation from manual counting from custom eye tracker and camera.

4.5.3 Short-term Induced Fatigue Test

The fatigue tracker was tested on introduced fatigue conditions. The entire test lasted for 15 minutes. In the first minute, the participant didn't get any instructions and could take a rest, and the blink and PERCLOS measurements were considered baseline values. After the first minute, participants began solving mathematical problems involving the multiplication or addition of two numbers less than 100. Participants could choose between multiplication or addition, so the difficulty was neither too high nor too low. The correctness of math solving was not considered as a fatigue indicator. To induce a higher level of fatigue [131], between minutes 5 and 10, a noise clip composed of three 120 beats-per-minute metronome ticks followed by a 0.5-second 1000-Hz alarm noise was played. Participants were asked to continue working on the math questions during and after the noise until the end of tests. Participants were asked to report their fatigue level on the

Karolinska Sleepiness Scale (KSS) at the end of the test. The whole protocol can be seen in Figure 30a.

A preliminary group of 10 participants were included in this test. The data are shown in Figure 30b-d. Figure 30b contrasts the blink rate and PERCLOS between the first minute ("Baseline") and the 2nd minute, where the math solving starts. In the first two minutes, the median blink counts were close to 10 blinks per minute, and PERCLOS was around 0.08. However, the range distribution was much wider during the baseline than in the second minute, indicating that participants with higher blink rates experienced a significant decrease when starting the math-solving task. This decrease in eye closure due to concentration has been observed in studies [132, 133], where blinks have been regarded as breaks in data processing that occurred less frequently during concentration.

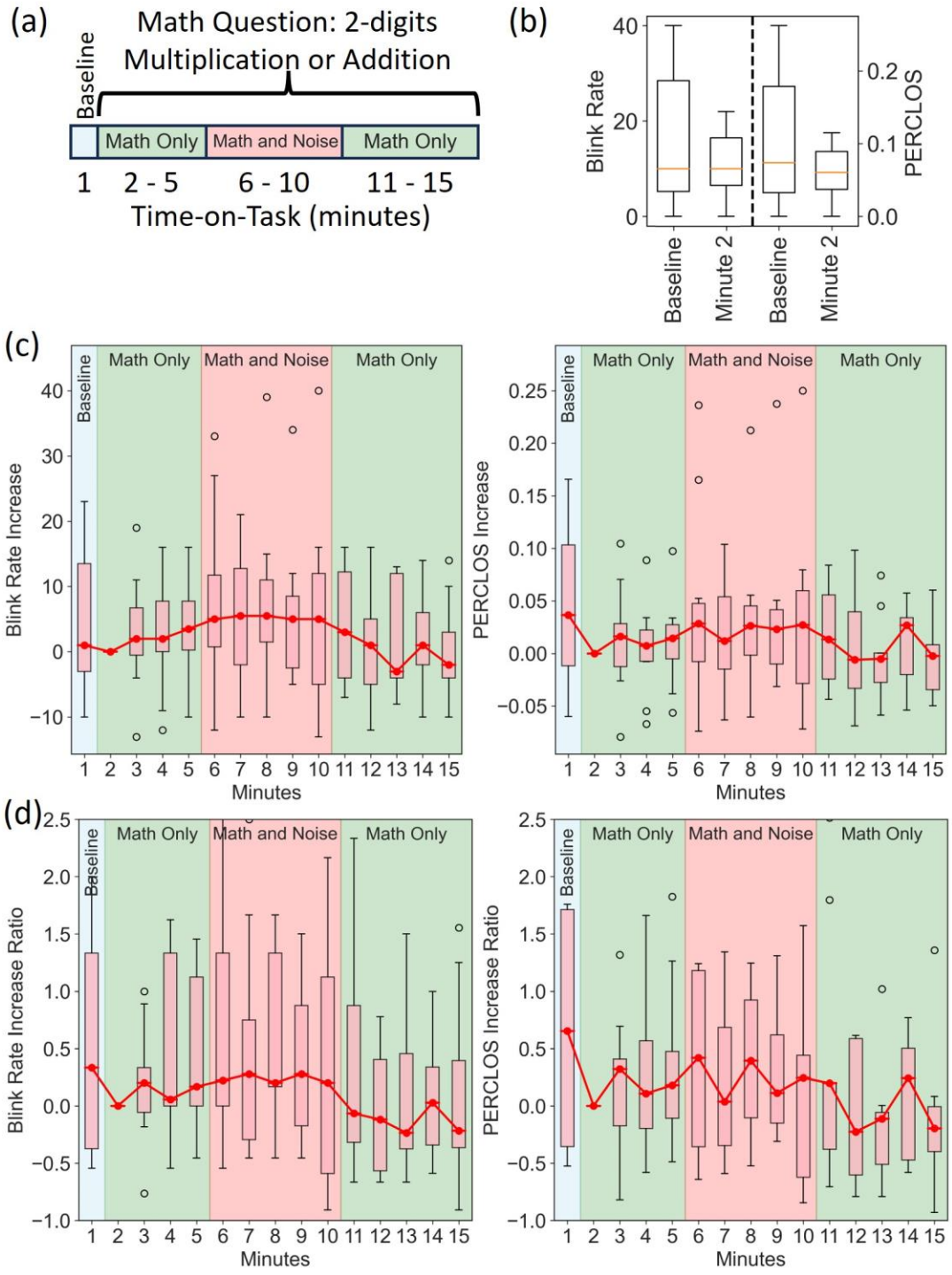

Figure 30. The blink rate and PERCLOS of a 15-minute induced fatigue test. (a) The test protocol. In the first minute, no specific instruction is given and the participant takes a rest. Between minute 2 to minute 15 the participants were asked to solve a double-digits number multiplication or

addition question. Participants can choose between multiplication or addition such that the questions are neither too easy nor overly difficult. Between 5 and 10 minutes, noise is played to induce higher fatigue. (b) Blink Rate and PERCLOS for minute 1 (resting baseline) and minute 2. (c) Boxplots showing blink rate (left) and PERCLOS (right) increases from minute 2. Median of all tests was highlighted by the red line. (d) Boxplots showing blink rate (left) and PERCLOS (right) percentage increases from minute 2. Median was highlighted by the red line.

Figure 30c and Figure 30d show an increase in blink count and PERCLOS after the second minute, with Figure 30c representing differences and Figure 30d representing percentage change. Both figures demonstrate large individual differences, increasing even more during the noise period. Each box in the boxplot represented one minute in the test. The whole test data were divided into three time-segments: Pre-noise (3 to 5 minutes), At-noise (6 to 10 minutes), and Post-noise (11 to 15 minutes). For each time segment, the median of each box's median value and the average of each box's IQR were calculated, as shown in Table 12.

The results showed an increase in fatigue between minutes 2 and 5, suggesting that the time-on-task (ToT) effect of math solving alone could cause fatigue. Between minutes 6 to 10, the combination of noise and math solving led to an even higher blink count and PERCLOS. After the noise ended, both blink rate and PERCLOS decreased. Results indicated that both math-solving and noise could effectively induce fatigue. Notably, the IQR during the noise segments was significantly higher than other math-only segments, indicating the fatigue caused by noise has more individual variance than fatigue from math-solving.

Table 12. The median and inter-quartile range (IQR) of increases from minute 2 at different test segments.

Metric	**Time Ranges**	**Absolute Increase from Minute 2 (Figure 30c)**	**Percentage Increase from Minute 2 (Figure 30d)**
Blink Rate (count)	Minute 3-5 (Pre-noise)	Median: 2.5, IQR: 7.5	Median: 64%, IQR: 95%
	Minute 6-10 (At-noise)	Median: 5.2, IQR 12.7	Median: 109%, IQR: 126%
	Minute 11-15 (Post-noise)	Median: 0, IQR 11.5	Median: 72%, IQR: 89%
PERCLOS	Minute 3-5 (Pre-noise)	Median: 0.013, IQR: 0.034	Median: 20%, IQR: 14%
	Minute 6-10 (At-noise)	Median: 0.023, IQR: 0.062	Median: 24%, IQR: 24%
	Minute 11-15 (Post-noise)	Median: 0.005, IQR: 0.056	Median: -1.8%, IQR: -12%

4.6 CONCLUSION

This chapter introduced a novel cylindrical capacitive sensor made of carbon-nanotube paper composite (CPC) for human eye tracking and fatigue monitoring. The cylindrical CPC sensor addressed the usability issues of flat CPC sensors and, when compared to identically sized copper sensors, demonstrated higher sensitivity and lower noise. The fabricated CPC cylindrical sensors were integrated into an eyeglass frame for non-intrusive human gaze tracking. Benchmark against the commercial Tobii Pro Nano eye-tracker showed that the CPC sensors could accurately track gaze with a median absolute error (MAE) of 0.97° to 1.75°.

Additionally, the capacitive eye-tracker could detect fatigue by measuring blink frequency and PERCLOS (Percentage of Eyelid Closure over the Pupil) biomarkers. Compared with manual

counting and computer vision-based algorithms, the eye-tracker showed less than 1 missed blink count and 1% PERCLOS deviation per 30-second segment. Real-world testing on noise-introduced trials with 10 participants successfully demonstrated the eye-tracker capability in detecting blink and PERCLOS biomarkers associated with time-on-task and noise.

In conclusion, the cylindrical CPC sensor-based capacitive eye-tracker could be a sensitive, non-contact method for both gaze tracking and fatigue monitoring. Its easy integration into wearable devices and existing eyeglasses allows new possibilities for continuous and unobtrusive monitoring of the human gaze and fatigue in numerous applications.

Chapter 5. Conclusions

5.1 Summary of Contribution

In summary, I developed an ultrasensitive capacitive sensor using carbon nanotube-paper composite (CPC) materials and demonstrated applications in human-machine interfaces (HMI) and eye tracking. Finite element analysis results showed that capacitive sensitivity could be increased by decreasing the baseline capacitance by using a smaller electrode or by increasing the with-target capacitance using a fibrous electrode. Using a single fibrous electrode achieved both. The sensor was made from a tensile fracture of CPC, which exposed numerous cellulose fibers. CPC capacitive sensors had higher capacitive sensitivity due to a higher electric field and total surface area from the high aspect ratio cellulose fiber microstructures. Through numerical simulation and experiment, the 10 mm-width single electrode CPC capacitive sensor demonstrated a 31.5% higher capacitive sensitivity than an identical-sized silver sensor, with a hand proximity sensitivity up to 300 mm and pressure sensitivity as low as 64 Pa. The sensor's application on water sensing, hand sensing, and machine-learning enhanced gesture recognition was demonstrated. The CPC capacitive sensor is one of the best in terms of sensitivity-to-size ratio and can have great potential in wearable human-machine interface applications.

I fabricated a novel wearable capacitive eye-tracker for non-human primates, utilizing four sensors in two pairs to measure proximity changes from the scleral-corneal junction during gaze movement. The capacitive eye-tracker was benchmarked against the gold standard scleral search coil method, showing a high linear correlation up to 0.97. Various data processing methods were explored, and alongside machine learning, the gaze tracking accuracy was as high as 0.3°, with a median accuracy of 0.8° for a single gaze pattern, comparable to commercial solutions while being

portable. This non-invasive capacitive eye-tracker served as an alternative to traditional coil and camera-based systems and had a great impact on oculomotor research and vision science.

The eye-tracking applications were further expanded to human eye-tracking. To address the sensor adjustment, displacement specificity, and limiting vision field challenges exposed in the non-human primate eye-tracker, I developed a novel cylindrical sensor by wrapping fractured CPC around a polyurethane core. Benchmark against identical sized copper sensor showed a nearly 100% higher capacitive sensitivity. The eye displacement during different gaze directions was studied with face scanning, and the results were used to optimize sensor placement to maximize sensitivity while mitigating interference. With optimized sensor placement and machine learning, the human eye-tracker demonstrated 1.37° median absolute error (MAE) in various gaze patterns over 45° gaze angles. The application was further extended to detect fatigue by quantifying blink counts and eye closure duration biomarkers. Compared with manual counting and computer-vision-based algorithms, the eye-tracker showed less than 1 missed blink count and 1% PERCLOS deviation per 30-second segment. A preliminary 10-subject test on noise-induced fatigue demonstrated the eye-tracker capability to detect blink and PERCLOS biomarkers in real-world applications among different people. Due to the light weight and low power requirement, this device offers a unique capability for all-day fatigue monitoring in a compact, wearable form, with wide applications in industrial safety, behavioral research, and medical diagnostics.

5.2 FUTURE WORKS

The CPC human eye-tracker is lightweight and low profile and offers high tracking resolution, long running time, and high portability. It can be further developed into applications

for eye-controlled HMI, for example, allowing elders or disabled people to communicate or signal with assistors with only gaze inputs, or controlling robotics with eye gaze for better human-machine collaboration.

The fatigue-tracking capability of the CPC human eye-tracker has significant potential for long-term, unobtrusive fatigue monitoring. Preliminary data indicate high accuracy in biomarker tracking and a strong correlation with fatigue in noise-induced fatigue tests. Nevertheless, while my preliminary data shows the high accuracy of biomarker tracking and good correlation with fatigue in the noise-induced fatigue test, the sample size is still low to draw a statistically significant conclusion. Currently, I'm collaborating with medical doctors to conduct a larger-scale test on patients with potential chronic fatigue symptoms. After that, full day-long tests for fatigue profiling will also be conducted.

List of References

[1] G. R. Kirchhoff, "Zur Theorie des Condensators," ed, 1879.

[2] E. R. Love, "The electrostatic field of two equal circular co-axial conducting disks," *The Quarterly Journal of Mechanics and Applied Mathematics,* vol. 2, no. 4, pp. 428-451, 1949.

[3] B. Reichert and Z. Ristivojevic, "Analytical results for the capacitance of a circular plate capacitor," (in English), *Phys Rev Res,* vol. 2, no. 1, Mar 10 2020, doi: 10.1103/PhysRevResearch.2.013289.

[4] R. M. Bo Luo, Yangqi Chen, Youyuan Zhang, Zhengyou He, "A voltage stress optimization method of capacitive power transfer charging system," presented at the Annual IEEE Conference on Applied Power Electronics Conference and Exposition (APEC), Tampa, FL, USA, 2017.

[5] Z. Z. Xu Chen, Shengbao Yu, Tiberiu-Gabriel Zsurzsan, "Fringing Effect Analysis of Parallel Plate Capacitors for Capacitive Power Transfer Application," presented at the International Future Energy Electronics Conference (IFEEC), Singapore, 2019.

[6] B. D. Hughes, "On the Potential Due to a Circular Parallel Plate Capacitor," (in English), *J Phys a-Math Gen,* vol. 17, no. 6, pp. 1385-1386, 1984, doi: 10.1088/0305-4470/17/6/033.

[7] V. Hutson, "The circular plate condenser at small separations," *Mathematical Proceedings of the Cambridge Philosophical Society,* vol. 59, no. 1, pp. 211-224, 1962, doi: 10.1017/S0305004100002152.

[8] *Ceramic Dielectric Capacitors Classes I, II, III, and IV Part II: Test Methods,* E. C. I. A. (ECIA), 1998.

[9] I. Amerini, P. Bestagini, L. Bondi, R. Caldelli, M. Casini, and S. Tubaro, "Robust smartphone fingerprint by mixing device sensors features for mobile strong authentication," presented at the Electronic Imaging, Media Watermarking, Security, and Forensics San Francisco, CA, 2016.

[10] B. Kumar, G. Rajita, and N. Mandal, "A Review on Capacitive-Type Sensor for Measurement of Height of Liquid Level," (in English), *Meas Control-Uk,* vol. 47, no. 7, pp. 219-224, Sep 2014, doi: 10.1177/0020294014546943.

[11] D. Castaneda, A. Esparza, M. Ghamari, C. Soltanpur, and H. Nazeran, "A review on wearable photoplethysmography sensors and their potential future applications in health care," *Int J Biosens Bioelectron,* vol. 4, no. 4, pp. 195-202, 2018, doi: 10.15406/ijbsbe.2018.04.00125.

[12] B. Vanwanseele, T. Op De Beéck, K. Schütte, and J. Davis, "Accelerometer Based Data Can Provide a Better Estimate of Cumulative Load During Running Compared to GPS Based Parameters," (in English), *Front Sports Act Liv,* vol. 2, Oct 30 2020, doi: 10.3389/fspor.2020.575596.

[13] V. T. van Hees *et al.*, "Estimating sleep parameters using an accelerometer without sleep diary," (in English), *Sci Rep-Uk,* vol. 8, Aug 28 2018, doi: 10.1038/s41598-018-31266-z.

[14] E. S. W. David Da He, Charles G. Sodini, "An Ear-worn Continuous Ballistocardiogram (BCG) Sensor for Cardiovascular Monitoring," in *IEEE Engineering in Medicine and Biology Society*, San Diego, CA, 2012, pp. 5030-5033, doi: 10.1109/EMBC.2012.6347123.

[15] C. S. Kim, A. M. Carek, O. T. Inan, R. Mukkamala, and J. O. Hahn, "Ballistocardiogram-Based Approach to Cuffless Blood Pressure Monitoring: Proof of Concept and Potential Challenges," *IEEE Transactions on Biomedical Engineering,* vol. 65, no. 11, pp. 2384-2391, 2018, doi: 10.1109/TBME.2018.2797239.

[16] S. A. Zawawi, A. A. Hamzah, B. Y. Majlis, and F. Mohd-Yasin, "A Review of MEMS Capacitive Microphones," (in English), *Micromachines-Basel,* vol. 11, no. 5, May 2020, doi: 10.3390/mi11050484.

[17] S. Kim, Y. Kawahara, A. Georgiadis, A. Collado, and M. M. Tentzeris, "Low-Cost Inkjet-Printed Fully Passive RFID Tags for Calibration-Free Capacitive/Haptic Sensor Applications," (in English), *Ieee Sens J,* vol. 15, no. 6, pp. 3135-3145, Jun 2015, doi: 10.1109/Jsen.2014.2366915.

[18] X. H. Guo, Y. Huang, X. Cai, C. X. Liu, and P. Liu, "Capacitive wearable tactile sensor based on smart textile substrate with carbon black/silicone rubber composite dielectric," (in English), *Meas Sci Technol,* vol. 27, no. 4, Apr 2016, doi: 10.1088/0957-0233/27/4/045105.

[19] J. Q. Zhang *et al.*, "Highly Stretchable and Self-Healable MXene/Polyvinyl Alcohol Hydrogel Electrode for Wearable Capacitive Electronic Skin," (in English), *Adv Electron Mater,* vol. 5, no. 7, Jul 2019, doi: 10.1002/aelm.201900285.

[20] S. Kanaparthi, "Pencil-drawn Paper-based Non-invasive and Wearable Capacitive Respiration Sensor," (in English), *Electroanal,* vol. 29, no. 12, pp. 2680-2684, Dec 2017, doi: 10.1002/elan.201700438.

[21] Z. C. Song, Y. Zhou, L. Zhao, C. L. Chang, W. X. An, and S. H. Yu, "A Wearable Capacitive Friction Force Sensor for E-Skin," (in English), *Acs Appl Electron Ma,* vol. 4, no. 8, pp. 3841-3848, Aug 23 2022, doi: 10.1021/acsaelm.2c00463.

[22] Bijender and A. Kumar, "Flexible and wearable capacitive pressure sensor for blood pressure monitoring," (in English), *Sens Bio-Sens Res,* vol. 33, Aug 2021, doi: 10.1016/j.sbsr.2021.100434.

[23] H. Yousef, M. Boukallel, and K. Althoefer, "Tactile sensing for dexterous in-hand manipulation in robotics-A review," (in English), *Sensor Actuat a-Phys,* vol. 167, no. 2, pp. 171-187, Jun 2011, doi: 10.1016/j.sna.2011.02.038.

[24] H. Oh, G. C. Yi, M. Yip, and S. A. Dayeh, "Scalable tactile sensor arrays on flexible substrates with high spatiotemporal resolution enabling slip and grip for closed-loop robotics," (in English), *Sci Adv,* vol. 6, no. 46, Nov 2020, doi: 10.1126/sciadv.abd7795.

[25] S. Patel, H. Park, P. Bonato, L. Chan, and M. Rodgers, "A review of wearable sensors and systems with application in rehabilitation," (in English), *J Neuroeng Rehabil,* vol. 9, Apr 20 2012, doi: 10.1186/1743-0003-9-21.

[26] M. M. Rodgers, V. M. Pai, and R. S. Conroy, "Recent Advances in Wearable Sensors for Health Monitoring," (in English), *Ieee Sens J,* vol. 15, no. 6, pp. 3119-3126, Jun 2015, doi: 10.1109/Jsen.2014.2357257.

[27] M. Mathew, S. Radhakrishnan, A. Vaidyanathan, B. Chakraborty, and C. S. Rout, "Flexible and wearable electrochemical biosensors based on two-dimensional materials: Recent developments," (in English), *Anal Bioanal Chem,* vol. 413, no. 3, pp. 727-762, Jan 2021, doi: 10.1007/s00216-020-03002-y.

[28] N. Zengeler, T. Kopinski, and U. Handmann, "Hand Gesture Recognition in Automotive Human-Machine Interaction Using Depth Cameras," (in English), *Sensors-Basel,* vol. 19, no. 1, Jan 1 2019, doi: 10.3390/s19010059.

[29] M. Arsalan and A. Santra, "Character Recognition in Air-Writing Based on Network of Radars for Human-Machine Interface," (in English), *Ieee Sens J,* vol. 19, no. 19, pp. 8855-8864, Oct 1 2019, doi: 10.1109/Jsen.2019.2922395.
[30] Z. M. Xiao, W. B. Hu, C. H. Liu, H. Yu, and C. Z. Li, "Noncontact Human-Machine Interface With Planar Probing Coils in a Differential Sensing Architecture," (in English), *Ieee T Instrum Meas,* vol. 67, no. 4, pp. 956-964, Apr 2018, doi: 10.1109/Tim.2017.2784079.
[31] S. F. Zhao *et al.*, "Recent Advancements in Flexible and Stretchable Electrodes for Electromechanical Sensors: Strategies, Materials, and Features," (in English), *Acs Appl Mater Inter,* vol. 9, no. 14, pp. 12147-12164, Apr 12 2017, doi: 10.1021/acsami.6b13800.
[32] Y. K. Li *et al.*, "Laser-Patterned Copper Electrodes for Proximity and Tactile Sensors," (in English), *Adv Mater Interfaces,* vol. 7, no. 4, Feb 2020, doi: 10.1002/admi.201901845.
[33] A. Murai, S. Kanazawa, K. Ayusawa, S. Washino, M. Yoshida, and M. Mochimaru, "DATSURYOKU Sensor-A Capacitive-Sensor-Based Belt for Predicting Muscle Tension: Preliminary Results," (in English), *Sensors-Basel,* vol. 21, no. 19, Oct 2021, doi: 10.3390/s21196669.
[34] H. T. Qin, Y. Cai, J. Y. Dong, and Y. S. Lee, "Direct Printing of Capacitive Touch Sensors on Flexible Substrates by Additive E-Jet Printing With Silver Nanoinks," (in English), *J Manuf Sci E-T Asme,* vol. 139, no. 3, Mar 2017, doi: 10.1115/1.4034663.
[35] A. Frutiger *et al.*, "Capacitive Soft Strain Sensors via Multicore-Shell Fiber Printing," (in English), *Adv Mater,* vol. 27, no. 15, pp. 2440-2446, Apr 17 2015, doi: 10.1002/adma.201500072.
[36] S. Tsuji and T. Kohama, "Self-Capacitance Proximity and Tactile Skin Sensor With Shock-Absorbing Structure for a Collaborative Robot," (in English), *Ieee Sens J,* vol. 20, no. 24, pp. 15075-15084, Dec 15 2020, doi: 10.1109/Jsen.2020.3011701.
[37] R. Moheimani, N. Aliahmad, N. Aliheidari, M. Agarwal, and H. Dalir, "Thermoplastic polyurethane flexible capacitive proximity sensor reinforced by CNTs for applications in the creative industries," (in English), *Sci Rep-Uk,* vol. 11, no. 1, Jan 13 2021, doi: 10.1038/s41598-020-80071-0.
[38] J. Y. Zhang, S. M. Goodman, H. G. Wise, A. B. Dichiara, and J. H. Chung, "Electromechanical coupling of isotropic fibrous networks with tailored auxetic behavior induced by water-printing under tension," (in English), *J Mater Chem C,* vol. 9, no. 13, pp. 4544-4553, Apr 7 2021, doi: 10.1039/d0tc05526c.
[39] A. B. Dichiara, A. Song, S. M. Goodman, D. He, and J. Bai, "Smart papers comprising carbon nanotubes and cellulose microfibers for multifunctional sensing applications," (in English), *J Mater Chem A,* vol. 5, no. 38, pp. 20161-20169, Oct 14 2017, doi: 10.1039/c7ta04329e.
[40] J. D. R. Robert J. Ouellette, "Alkanes and Cycloalkanes: Structures and Reactions," in *Organic Chemistry*: Elsevier, 2014, ch. 4, pp. 111-161.
[41] G. B. Graeme J. Ackland, "Interatomic Potential Development," in *Comprehensive Nuclear Materials (Second Edition),* vol. 1, R. E. S. Rudy J.M. Konings Ed.: Elsevier, 2020, pp. 544-572.
[42] N. Fakhri, D. A. Tsyboulski, L. Cognet, R. B. Weisman, and M. Pasquali, "Diameter-dependent bending dynamics of single-walled carbon nanotubes in liquids," (in English),

P Natl Acad Sci USA, vol. 106, no. 34, pp. 14219-14223, Aug 25 2009, doi: 10.1073/pnas.0904148106.
[43] E. F. Antunes, A. O. Lobo, E. J. Corat, and V. J. Trava-Airoldi, "Influence of diameter in the Raman spectra of aligned multi-walled carbon nanotubes," (in English), *Carbon*, vol. 45, no. 5, pp. 913-921, Apr 2007, doi: 10.1016/j.carbon.2007.01.003.
[44] J. K. Streit, S. M. Bachilo, A. V. Naumov, C. Khripin, M. Zheng, and R. B. Weisman, "Measuring Single-Walled Carbon Nanotube Length Distributions from Diffusional Trajectories," *ACS Nano*, vol. 6, no. 9, pp. 8424-8431, 2012/09/25 2012, doi: 10.1021/nn3032744.
[45] Z. W. Wang, C. C. Luan, G. X. Liao, J. P. Liu, X. H. Yao, and J. Z. Fu, "Progress in Auxetic Mechanical Metamaterials: Structures, Characteristics, Manufacturing Methods, and Applications," (in English), *Adv Eng Mater*, vol. 22, no. 10, Oct 2020, doi: 10.1002/adem.202000312.
[46] W. W. Wu, W. X. Hu, G. A. Qian, H. T. Liao, X. Y. Xu, and F. Berto, "Mechanical design and multifunctional applications of chiral mechanical metamaterials: A review," (in English), *Mater Design*, vol. 180, Oct 15 2019, doi: 10.1016/j.matdes.2019.107950.
[47] R. F. Almgren, "An Isotropic 3-Dimensional Structure with Poisson Ratio=-1," (in English), *J Elasticity*, vol. 15, no. 4, pp. 427-430, 1985.
[48] J. N. Grima and K. E. Evans, "Auxetic behavior from rotating squares," (in English), *J Mater Sci Lett*, vol. 19, no. 17, pp. 1563-1565, Sep 2000, doi: Doi 10.1023/A:1006781224002.
[49] N. Stenberg and C. Fellers, "Out-of-plane Poisson's ratios of paper and paperboard," (in English), *Nord Pulp Pap Res J*, vol. 17, no. 4, pp. 387-394, 2002, doi: DOI 10.3183/npprj-2002-17-04-p387-394.
[50] B. E. Thirlwell and L. R. G. Treloar, "Non-Woven Fabrics .6. Dimensional and Mechanical Anisotropy," (in English), *Text Res J*, vol. 35, no. 9, pp. 827-+, 1965, doi: 10.1177/004051756503500907.
[51] R. Peng, Y. D. Ma, Q. Wu, B. B. Huang, and Y. Dai, "Two-dimensional materials with intrinsic auxeticity: progress and perspectives," (in English), *Nanoscale*, vol. 11, no. 24, pp. 11413-11428, Jun 28 2019, doi: 10.1039/c9nr03546j.
[52] S. Domaschke, A. Morel, G. Fortunato, and A. E. Ehret, "Random auxetics from buckling fibre networks," (in English), *Nat Commun*, vol. 10, Oct 25 2019, doi: 10.1038/s41467-019-12757-7.
[53] COMSOL. "Zero Charge." https://doc.comsol.com/5.5/doc/com.comsol.help.semicond/semicond_ug_acdc.7.08.html (accessed Nov-21, 2023).
[54] A. F. Fuchs, C. R. Kaneko, and C. A. Scudder, "Brainstem control of saccadic eye movements," (in eng), *Annual review of neuroscience*, vol. 8, pp. 307-37, 1985, doi: 10.1146/annurev.ne.08.030185.001515.
[55] E. L. Keller, N. J. Gandhi, and J. M. Shieh, "Endpoint accuracy in saccades interrupted by stimulation in the omnipause region in monkey," (in eng), *Visual neuroscience*, vol. 13, no. 6, pp. 1059-67, Nov-Dec 1996.
[56] E. L. Keller, N. J. Gandhi, and S. Vijay Sekaran, "Activity in deep intermediate layer collicular neurons during interrupted saccades," (in eng), *Experimental brain research*, vol. 130, no. 2, pp. 227-37, Jan 2000.

[57] C. A. Scudder, C. S. Kaneko, and A. F. Fuchs, "The brainstem burst generator for saccadic eye movements: a modern synthesis," (in eng), *Experimental brain research,* vol. 142, no. 4, pp. 439-62, Feb 2002, doi: 10.1007/s00221-001-0912-9.
[58] J. J. Hopp and A. F. Fuchs, "The characteristics and neuronal substrate of saccadic eye movement plasticity," (in eng), *Progress in neurobiology,* vol. 72, no. 1, pp. 27-53, Jan 2004, doi: 10.1016/j.pneurobio.2003.12.002.
[59] R. Soetedjo, Y. Kojima, and A. F. Fuchs, "How cerebellar motor learning keeps saccades accurate," (in eng), *Journal of neurophysiology,* vol. 121, no. 6, pp. 2153-2162, Jun 1 2019, doi: 10.1152/jn.00781.2018.
[60] E. C. Lee, J. C. Woo, J. H. Kim, M. Whang, and K. R. Park, "A brain-computer interface method combined with eye tracking for 3D interaction," (in English), *J Neurosci Meth,* vol. 190, no. 2, pp. 289-298, Jul 15 2010, doi: 10.1016/j.jneumeth.2010.05.008.
[61] M. N. Shadlen and W. T. Newsome, "Neural basis of a perceptual decision in the parietal cortex (area LIP) of the rhesus monkey," (in eng), *Journal of neurophysiology,* vol. 86, no. 4, pp. 1916-36, Oct 2001, doi: 10.1152/jn.2001.86.4.1916.
[62] C. R. Camalier *et al.*, "Dynamics of saccade target selection: race model analysis of double step and search step saccade production in human and macaque," (in eng), *Vision research,* vol. 47, no. 16, pp. 2187-211, Jul 2007, doi: 10.1016/j.visres.2007.04.021.
[63] M. P. Grant *et al.*, "Abnormal eye movements in Creutzfeldt-Jakob disease," (in eng), *Annals of neurology,* vol. 34, no. 2, pp. 192-7, Aug 1993, doi: 10.1002/ana.410340215.
[64] U. Rosenhall, E. Johansson, and C. Gillberg, "Oculomotor findings in autistic children," (in eng), *The Journal of laryngology and otology,* vol. 102, no. 5, pp. 435-9, May 1988, doi: 10.1017/s0022215100105286.
[65] G. M. Jones and J. D. DeJong, "Dynamic characteristics of saccadic eye movements in Parkinson's disease," (in eng), *Experimental neurology,* vol. 31, no. 1, pp. 17-31, Apr 1971, doi: 10.1016/0014-4886(71)90173-7.
[66] J. Bek, E. Poliakoff, and K. Lander, "Measuring emotion recognition by people with Parkinson's disease using eye-tracking with dynamic facial expressions," (in English), *J Neurosci Meth,* vol. 331, Feb 1 2020, doi: 10.1016/j.jneumeth.2019.108524.
[67] G. Avanzini, F. Girotti, T. Caraceni, and R. Spreafico, "Oculomotor disorders in Huntington's chorea," (in eng), *Journal of neurology, neurosurgery, and psychiatry,* vol. 42, no. 7, pp. 581-9, Jul 1979, doi: 10.1136/jnnp.42.7.581.
[68] A. T. Duchowski, *Eye Tracking Methodology: Theory and Practice*. London: Springer, 2003.
[69] E. Marg, "Development of Electro-Oculography - Standing Potential of the Eye in Registration of Eye Movement," (in English), *Ama Arch Ophthalmol,* vol. 45, no. 2, pp. 169-185, 1951, doi: DOI 10.1001/archopht.1951.01700010174006.
[70] T. N. Cornsweet and H. D. Crane, "Accurate two-dimensional eye tracker using first and fourth Purkinje images," *J. Opt. Soc. Am.,* vol. 63, no. 8, pp. 921-928, 1973/08/01 1973, doi: 10.1364/JOSA.63.000921.
[71] H. H. L. M. Goossens and A. J. Van Opstal, "Blink-perturbed saccades in monkey. II. Superior colliculus activity," (in English), *Journal of neurophysiology,* vol. 83, no. 6, pp. 3430-3452, Jun 2000, doi: 10.1152/jn.2000.83.6.3430.
[72] M. M. Houben, J. Goumans, and J. van der Steen, "Recording three-dimensional eye movements: scleral search coils versus video oculography," (in eng), *Invest Ophthalmol Vis Sci,* vol. 47, no. 1, pp. 179-87, Jan 2006, doi: 10.1167/iovs.05-0234.

[73] B. L. Zuber, J. L. Semmlow, and L. Stark, "Frequency characteristics of the saccadic eye movement," (in eng), *Biophysical journal,* vol. 8, no. 11, pp. 1288-98, Nov 1968, doi: 10.1016/s0006-3495(68)86556-7.
[74] D. A. Robinson, "A Method of Measuring Eye Movemnent Using a Scieral Search Coil in a Magnetic Field," (in eng), *IEEE transactions on bio-medical engineering,* vol. 10, pp. 137-45, Oct 1963.
[75] A. F. Fuchs and D. A. Robinson, "A method for measuring horizontal and vertical eye movement chronically in the monkey," (in eng), *Journal of applied physiology,* vol. 21, no. 3, pp. 1068-70, May 1966.
[76] S. J. Judge, B. J. Richmond, and F. C. Chu, "Implantation of magnetic search coils for measurement of eye position: an improved method," (in eng), *Vision research,* vol. 20, no. 6, pp. 535-8, 1980.
[77] L. Grosenick, J. H. Marshel, and K. Deisseroth, "Closed-loop and activity-guided optogenetic control," (in eng), *Neuron,* vol. 86, no. 1, pp. 106-39, Apr 08 2015, doi: 10.1016/j.neuron.2015.03.034.
[78] Y. El-Shamayleh, Y. Kojima, R. Soetedjo, and G. D. Horwitz, "Selective Optogenetic Control of Purkinje Cells in Monkey Cerebellum," (in eng), *Neuron,* vol. 95, no. 1, pp. 51-62.e4, Jul 5 2017, doi: 10.1016/j.neuron.2017.06.002.
[79] R. Soetedjo and G. D. Horwitz, "Closed-Loop Optogenetic Perturbation of Macaque Oculomotor Cerebellum: Evidence for an Internal Saccade Model," *The Journal of Neuroscience,* vol. 44, no. 6, p. e1317232023, 2024, doi: 10.1523/JNEUROSCI.1317-23.2023.
[80] A. Braun, R. Wichert, A. Kuijper, and D. W. Fellner, "Capacitive proximity sensing in smart environments," (in English), *J. Ambient Intell. Smart Environ.,* Article vol. 7, no. 4, pp. 483-510, 2015, doi: 10.3233/ais-150324.
[81] K. K. Sadasivuni, A. Kafy, L. Zhai, H. U. Ko, S. Mun, and J. Kim, "Transparent and flexible cellulose nanocrystal/reduced graphene oxide film for proximity sensing," (in eng), *Small,* vol. 11, no. 8, pp. 994-1002, Feb 25 2015, doi: 10.1002/smll.201402109.
[82] A. Nelson, G. Singh, R. Robucci, C. Patel, and N. Banerjee, "Adaptive and Personalized Gesture Recognition Using Textile Capacitive Sensor Arrays," *IEEE Transactions on Multi-Scale Computing Systems,* vol. 1, no. 2, pp. 62-75, 2015, doi: 10.1109/TMSCS.2015.2495100.
[83] A. Consejo, C. Llorens-Quintana, M. M. Bartuzel, D. R. Iskander, and J. J. Rozema, "Rotation asymmetry of the human sclera," (in eng), *Acta ophthalmologica,* vol. 97, no. 2, pp. e266-e270, Mar 2019, doi: 10.1111/aos.13901.
[84] C. R. S. Kaneko, S. Rosenfeld, E. Fontaine, A. Markov, J. O. Phillips, and J. Yarno, "A preformed scleral search coil for measuring mouse eye movements," (in English), *J Neurosci Meth,* vol. 193, no. 1, pp. 126-131, Oct 30 2010, doi: 10.1016/j.jneumeth.2010.08.023.
[85] S. Adade and V. E. Das, "Vertical vergence in nonhuman primates depends on horizontal gaze position," (in English), *Strabismus,* vol. 27, no. 3, pp. 172-181, 2019, doi: 10.1080/09273972.2019.1629465.
[86] P. J. Boutros, N. S. Valentin, K. N. Hageman, C. K. Dai, D. Roberts, and C. C. Della Santina, "Nonhuman primate vestibuloocular reflex responses to prosthetic vestibular stimulation are robust to pulse timing errors caused by temporal discretization," (in

English), *Journal of neurophysiology*, vol. 121, no. 6, pp. 2256-2266, Jun 2019, doi: 10.1152/jn.00887.2018.
[87] J. P. Gottlieb, M. G. Macavoy, and C. J. Bruce, "Neural Responses Related to Smooth-Pursuit Eye-Movements and Their Correspondence with Electrically Elicited Smooth Eye-Movements in the Primate Frontal Eye Field," (in English), *Journal of neurophysiology*, vol. 72, no. 4, pp. 1634-1653, Oct 1994, doi: 10.1152/jn.1994.72.4.1634.
[88] R. Soetedjo, C. R. S. Kaneko, and A. F. Fuchs, "Evidence that the superior colliculus participates in the feedback control of saccadic eye movements," (in English), *Journal of neurophysiology*, vol. 87, no. 2, pp. 679-695, Feb 2002, doi: 10.1152/jn.00886.2000.
[89] P. Foeller and L. Tychsen, "Eye movement training and recording in alert macaque monkeys: 1. Operant visual conditioning; 2. Magnetic search coil and head restraint surgical implantation; 3. Calibration and recording," *Strabismus,* vol. 10, no. 1, pp. 5-22, Mar 2002, doi: 10.1076/stra.10.1.5.8154.
[90] Y. Tang *et al.*, "Eye Position Compensation Improves Estimates of Response Magnitude and Receptive Field Geometry in Alert Monkeys," *J Neurophysiol,* vol. 97, no. 5, pp. 3439-3448, 2007/05/01 2007, doi: 10.1152/jn.00881.2006.
[91] A. Cohen, I. Daubechies, and J. C. Feauveau, "Biorthogonal Bases of Compactly Supported Wavelets," (in English), *Commun Pur Appl Math,* vol. 45, no. 5, pp. 485-560, Jun 1992, doi: 10.1002/cpa.3160450502.
[92] I. Daubechies, "The Wavelet Transform, Time-Frequency Localization and Signal Analysis," (in English), *Ieee T Inform Theory,* vol. 36, no. 5, pp. 961-1005, Sep 1990, doi: Doi 10.1109/18.57199.
[93] T. Y. Li *et al.*, "Ultrasensitive Capacitive Sensor Composed of Nanostructured Electrodes for Human-Machine Interface," (in English), *Adv Mater Technol,* vol. 7, no. 10, Oct 2022, doi: 10.1002/admt.202101704.
[94] V. Sakthivelpathi *et al.*, "Capacitive eye tracker made of fractured carbon nanotube-paper composites for wearable applications," *Sensors and Actuators A: Physical,* vol. 344, p. 113739, 2022/09/01/ 2022, doi: 10.1016/j.sna.2022.113739.
[95] S. Banks and D. F. Dinges, "Behavioral and Physiological Consequences of Sleep Restriction," (in English), *J Clin Sleep Med,* vol. 3, no. 5, pp. 519-528, 2007.
[96] A. Moradi, S. S. H. Nazari, and K. Rahmani, "Sleepiness and the risk of road traffic accidents: A systematic review and meta-analysis of previous studies," (in English), *Transport Res F-Traf,* vol. 65, pp. 620-629, Aug 2019, doi: 10.1016/j.trf.2018.09.013.
[97] K. Uehli *et al.*, "Sleep problems and work injuries: A systematic review and meta-analysis," (in English), *Sleep Med Rev,* vol. 18, no. 1, pp. 61-73, Feb 2014, doi: 10.1016/j.smrv.2013.01.004.
[98] D. A. Lombardi, S. Folkard, J. L. Willetts, and G. S. Smith, "Daily Sleep, Weekly Working Hours, and Risk of Work-Related Injury: Us National Health Interview Survey (2004-2008)," (in English), *Chronobiol Int,* vol. 27, no. 5, pp. 1013-1030, 2010, doi: 10.3109/07420528.2010.489466.
[99] M. P. Walker, "The Role of Sleep in Cognition and Emotion," (in English), *Ann Ny Acad Sci,* vol. 1156, pp. 168-197, 2009, doi: 10.1111/j.1749-6632.2009.04416.x.
[100] P. Alhola and P. Polo-Kantola, "Sleep deprivation: Impact on cognitive performance," *Neuropsychiatr Dis Treat,* vol. 3, no. 5, pp. 553-67, 2007.

[101] R. J. Williamson *et al.*, "The relationship of fatigue to mental and physical health in a community sample," (in English), *Soc Psych Psych Epid,* vol. 40, no. 2, pp. 126-132, Feb 2005, doi: 10.1007/s00127-005-0858-5.
[102] E. M. Kleiman, B. J. Turner, A. L. Chapman, and M. K. Nock, "Fatigue Moderates the Relationship Between Perceived Stress and Suicidal Ideation: Evidence From Two High-Resolution Studies," (in English), *J Clin Child Adolesc,* vol. 47, no. 1, pp. 116-130, 2018, doi: 10.1080/15374416.2017.1342543.
[103] R. Nelesen, Y. Dar, K. Thomas, and J. E. Dimsdale, "The relationship between fatigue and cardiac functioning," (in English), *Arch Intern Med,* vol. 168, no. 9, pp. 943-949, May 12 2008, doi: 10.1001/archinte.168.9.943.
[104] T. Akerstedt and M. Gillberg, "Subjective and Objective Sleepiness in the Active Individual," (in English), *Int J Neurosci,* vol. 52, no. 1-2, pp. 29-37, 1990, doi: Doi 10.3109/00207459008994241.
[105] K. Kaida *et al.*, "Validation of the Karolinska sleepiness scale against performance and EEG variables," (in English), *Clin Neurophysiol,* vol. 117, no. 7, pp. 1574-1581, Jul 2006, doi: 10.1016/j.clinph.2006.03.011.
[106] M. Kumari *et al.*, "Cortisol secretion and fatigue: Associations in a community based cohort," (in English), *Psychoneuroendocrino,* vol. 34, no. 10, pp. 1476-1485, Nov 2009, doi: 10.1016/j.psyneuen.2009.05.001.
[107] D. J. H. Powell, C. Liossi, R. Moss-Morris, and W. Schlotz, "Unstimulated cortisol secretory activity in everyday life and its relationship with fatigue and chronic fatigue syndrome: A systematic review and subset meta-analysis," (in English), *Psychoneuroendocrino,* vol. 38, no. 11, pp. 2405-2422, Nov 2013, doi: 10.1016/j.psyneuen.2013.07.004.
[108] M. Basner, D. Mollicone, and D. F. Dinges, "Validity and sensitivity of a brief psychomotor vigilance test (PVT-B) to total and partial sleep deprivation," (in English), *Acta Astronaut,* vol. 69, no. 11-12, pp. 949-959, Dec 2011, doi: 10.1016/j.actaastro.2011.07.015.
[109] S. K. L. Lal and A. Craig, "A critical review of the psychophysiology of driver fatigue," (in English), *Biol Psychol,* vol. 55, no. 3, pp. 173-194, Feb 2001, doi: Doi 10.1016/S0301-0511(00)00085-5.
[110] A. Craig, Y. Tran, N. Wijesuriya, and H. Nguyen, "Regional brain wave activity changes associated with fatigue," (in English), *Psychophysiology,* vol. 49, no. 4, pp. 574-582, Apr 2012, doi: 10.1111/j.1469-8986.2011.01329.x.
[111] O. G. Okogbaa, R. L. Shell, and D. Filipusic, "On the Investigation of the Neurophysiological Correlates of Knowledge Worker Mental Fatigue Using the Eeg Signal," (in English), *Appl Ergon,* vol. 25, no. 6, pp. 355-365, Dec 1994, doi: Doi 10.1016/0003-6870(94)90054-X.
[112] W. Klimesch, "EEG alpha and theta oscillations reflect cognitive and memory performance: a review and analysis," (in English), *Brain Res Rev,* vol. 29, no. 2-3, pp. 169-195, Apr 1999, doi: Doi 10.1016/S0165-0173(98)00056-3.
[113] W. Klimesch, "Alpha-band oscillations, attention, and controlled access to stored information," (in English), *Trends Cogn Sci,* vol. 16, no. 12, pp. 606-617, Dec 2012, doi: 10.1016/j.tics.2012.10.007.
[114] S. Gannouni, A. Aledaily, K. Belwafi, and H. Aboalsamh, "Emotion detection using electroencephalography signals and a zero-time windowing-based epoch estimation and

relevant electrode identification," (in English), *Sci Rep-Uk*, vol. 11, no. 1, Mar 29 2021, doi: 10.1038/s41598-021-86345-5.
[115] A. J. Cleare, "The HPA axis and the genesis of chronic fatigue syndrome," (in English), *Trends Endocrin Met*, vol. 15, no. 2, pp. 55-59, Mar 2004, doi: 10.1016/j.tem.2003.12.002.
[116] A. D. L. Roberts, S. Wessely, T. Chalder, A. Papadopoulos, and A. J. Cleare, "Salivary cortisol response to awakening in chronic fatigue syndrome," (in English), *Brit J Psychiat*, vol. 184, pp. 136-141, Feb 2004, doi: 10.1192/bjp.184.2.136.
[117] "PERCLOS: A Valid Psychophysiological Measure of Alertness As Assessed by Psychomotor Vigilance," United States. Federal Motor Carrier Safety Administration. Technology Division, 1998.
[118] D. Sommer and M. Golz, "Evaluation of PERCLOS based current fatigue monitoring technologies," in *2010 Annual International Conference of the IEEE Engineering in Medicine and Biology*, 31 Aug.-4 Sept. 2010 2010, pp. 4456-4459, doi: 10.1109/IEMBS.2010.5625960.
[119] J. A. Stern, D. Boyer, and D. Schroeder, "Blink Rate - a Possible Measure of Fatigue," (in English), *Hum Factors*, vol. 36, no. 2, pp. 285-297, Jun 1994, doi: 10.1177/001872089403600209.
[120] R. Z. Marandi, P. Madeleine, O. Omland, N. Vuillerme, and A. Samani, "Eye movement characteristics reflected fatigue development in both young and elderly individuals," (in English), *Sci Rep-Uk*, vol. 8, Sep 3 2018, doi: 10.1038/s41598-018-31577-1.
[121] Y. Laidani, S. Hanini, G. Mortha, and G. Heninia, "Study of a Fibrous Annual Plant, Luffa Cylindrica for Paper Application Part I: Characterization of the Vegetal," *Iranian Journal of Chemistry and Chemical Engineering*, vol. 31, pp. 119-129, 12/01 2012.
[122] M. K. Katz, Philip B., "The human eye as an optical system," in *Duane's Clinical Ophthalmology*, vol. 1. Philadelphia: Lippincott Williams & Wilkins, 2013, ch. 33.
[123] C. S. Foster, D. Azar, and C. H. Dohlman, *Smolin and Thoft's The Cornea: Scientific Foundations and Clinical Practice*, 4 ed. Lippincott Williams & Wilkins, 2004.
[124] K. A. Kwon *et al.*, "High-speed camera characterization of voluntary eye blinking kinematics," (in English), *J R Soc Interface*, vol. 10, no. 85, Aug 6 2013, doi: 10.1098/rsif.2013.0227.
[125] M. Bologna *et al.*, "Voluntary, spontaneous and reflex blinking in patients with clinically probable progressive supranuclear palsy," (in English), *Brain*, vol. 132, pp. 502-510, Feb 2009, doi: 10.1093/brain/awn317.
[126] S. H. Choi, K. S. Park, M. W. Sung, and K. H. Kim, "Dynamic and quantitative evaluation of eyelid motion using image analysis," (in English), *Med Biol Eng Comput*, vol. 41, no. 2, pp. 146-150, Mar 2003, doi: 10.1007/Bf02344882.
[127] M. Korosec, I. Zidar, D. Reits, C. Evinger, and F. VanderWerf, "Eyelid movements during blinking in patients with Parkinson's disease," (in English), *Movement Disord*, vol. 21, no. 8, pp. 1248-1251, Aug 2006, doi: 10.1002/mds.20930.
[128] W. S. Sun *et al.*, "Age-related changes in human blinks - Passive and active changes in eyelid kinematics," (in English), *Invest Ophth Vis Sci*, vol. 38, no. 1, pp. 92-99, Jan 1997.
[129] D. King. "dlib C++ Library." http://dlib.net/ (accessed Mar-2024.
[130] C. Dewi, R. C. Chen, C. W. Chang, S. H. Wu, X. Y. Jiang, and H. Yu, "Eye Aspect Ratio for Real-Time Drowsiness Detection to Improve Driver Safety," (in English), *Electronics-Switz*, vol. 11, no. 19, Oct 2022, doi: 10.3390/electronics11193183.

[131] U. Landstrom, "Noise and Fatigue in Working Environments," (in English), *Environ Int*, vol. 16, no. 4-6, pp. 471-476, 1990, doi: Doi 10.1016/0160-4120(90)90015-X.
[132] Z. W. Wu, C. G. Begley, P. Situ, T. Simpson, and H. X. Liu, "The Effects of Mild Ocular Surface Stimulation and Concentration on Spontaneous Blink Parameters," (in English), *Curr Eye Res*, vol. 39, no. 1, pp. 9-20, Jan 2014, doi: 10.3109/02713683.2013.822896.
[133] A. A. Abusharha, "Changes in blink rate and ocular symptoms during different reading tasks," *Clinical Optometry*, vol. 9, no. null, pp. 133-138, 2017/11/20 2017, doi: 10.2147/OPTO.S142718.